

Simulation Studies of Transition Metal and Actinide Oxides

A thesis submitted to the Department of Chemistry of
University College London in partial fulfilment of the
requirements for the degree of Doctor of Philosophy.

By
Steven Nicoll
October 1995

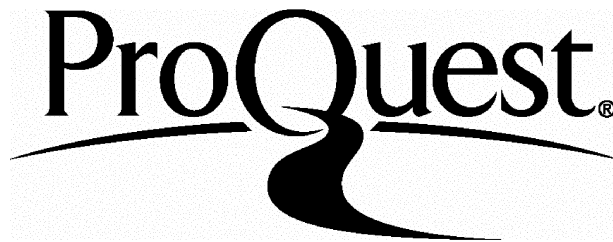
ProQuest Number: 10016729

All rights reserved

INFORMATION TO ALL USERS

The quality of this reproduction is dependent upon the quality of the copy submitted.

In the unlikely event that the author did not send a complete manuscript and there are missing pages, these will be noted. Also, if material had to be removed, a note will indicate the deletion.



ProQuest 10016729

Published by ProQuest LLC(2016). Copyright of the Dissertation is held by the Author.

All rights reserved.

This work is protected against unauthorized copying under Title 17, United States Code.
Microform Edition © ProQuest LLC.

ProQuest LLC
789 East Eisenhower Parkway
P.O. Box 1346
Ann Arbor, MI 48106-1346

ABSTRACT

This thesis reports the results of several studies carried out using the technique of atomistic computer simulation.

First, an investigation of the behaviour of several important fission products in UO_{2+x} is discussed. With the aid of a simple statistical mechanical model of defect equilibria, the favoured location for single Xe atoms in UO_2 is found to display a marked dependence on the Xe concentration. A predicted change in the preferred location of Xe as the Xe concentration is increased, is shown to coincide with a well known reduction in the diffusion coefficient of this fission product. Using similar techniques, the charge state and location of Mo atoms in UO_{2+x} is then investigated. A computed estimate of the solubility of Mo in UO_{2+x} is found to agree with the generally insoluble nature for this important fission product. Mo atoms dispersed in the lattice are calculated to have a charge state of no greater than 3+. Results are also given concerning the behaviour of atoms of the closely related fission products Ru, Rh and Pd. Finally, as a test of our model for fission product solubility, the behaviour of Sr and Ba in UO_2 is investigated and the results compared with experiment.

The clustering of defects in the highly non-stoichiometric transition metal oxides Mn_{1-x}O , Fe_{1-x}O , Co_{1-x}O and Ni_{1-x}O is a well studied phenomenon. In the final part of this thesis the effect of the dopants Mn, Fe, Co and Ni on the stability of several important defect structures in these oxides is investigated. If crystal field effects are included in the analysis, Fe is found to enhance the stability of {4:1} defect clusters in Mn_{1-x}O , Co_{1-x}O and Ni_{1-x}O .

To Gran and Grandad

ACKNOWLEDGEMENTS

The work described in this thesis was carried out as part of a collaboration between the Institute for Transuranium Elements (European Commission Joint Research Centre, Karlsruhe) and the Royal Institution of Great Britain. I have benefited greatly from the help and advice of many of my friends and colleagues at both of these institutions. I particularly thank my supervisors Dr.Hj.Matzke (Karlsruhe) and Prof.C.R.A.Catlow (RI) for their continued help, advice and patience. Dr.R.W.Grimes (now at Imperial College, London) is also thanked, particularly for supervision during the early part of this work and for suggesting the study on Mo in UO₂.

I am grateful for the grant of a PhD fellowship from the Human Capital and Mobility Programme of the European Commission, during the period of which the work on UO₂ was carried out. The financial support of Harwell Laboratory and the Royal Institution, for the transition metal oxide study, is also gratefully acknowledged.

In Karlsruhe, I am indebted to Dr.I.Ray and his family for their hospitality and support when I first arrived in Germany. Dr.E.R.R.Hernandez is thanked for letting me have a copy of his thesis which I have used as a bench mark on all matters concerning style. And finally, Deb is thanked for everything else, including proof reading the final manuscript.

LIST OF CONTENTS

Abstract	3
Acknowledgements	5
List of Figures	10
List of Tables	13
Part 1 — Methods	15
1 Introductory Remarks	17
2 Defect Statistics	21
2.1 Overview	21
2.2 Defect Formation Energies.....	25
2.3 Solubility	27
2.4 Comment	30
3 Simulation Techniques and Potentials	31
3.1 Simulating the Perfect Lattice	31
3.2 Crystal Properties	35

3.3 The Calculation of Defect Formation Energies	36
3.4 Interionic Potentials	40
3.5 Ionic Polarizability	46
3.6 Summary	47
Part 2 — Fission Products in UO₂	49
4 Introduction	51
4.1 Outline of Experimental Knowledge.....	52
4.1.1 <i>Basic Solid State Chemistry</i>	52
4.1.2 <i>Fission Product Behaviour</i>	55
4.2 Outline of Previous Computational Work.....	57
4.3 Overview of Part 2	59
5 Xe	67
5.1 Introduction.....	67
5.2 Experimental Knowledge and Previous Computational Work.....	67
5.3 Computational Procedure	71
5.4 Results and Discussion.....	75
5.5 Summary	80
6 Mo	83
6.1 Introduction.....	83
6.2 Experimental Knowledge.....	85

6.3 Computer Simulation of Mo in Urania.....	87
6.4 Results.....	92
6.5 Further Analysis and Discussion.....	102
6.6 Summary	111
7 Ru, Rh and Pd	113
7.1 Introduction.....	113
7.2 Experimental knowledge.....	113
7.3 The computer simulation of Ru, Rh and Pd	116
7.4 Results.....	121
7.4.1 Ru.....	125
7.4.2 Rh.....	131
7.4.3 Pd.....	136
7.5 Analysis and Discussion	142
7.6 Summary	147
8 Sr and Ba	149
8.1 Introduction.....	149
8.2 The Behaviour of Sr and Ba in UO_{2+x}	151
Part 3 — Dopants in Transition Metal Oxides	161
9 Introduction	163
9.1 The Transition Metal Oxides	163

10 Methods	169
10.1 Interionic Potentials	169
<i>10.1.1 Potentials for $M^{2+}-O^{2-}$ and $O^{2-}-O^{2-}$ interactions.....</i>	<i>170</i>
<i>10.1.2 Potentials for $M^{3+}-O^{2-}$ interactions</i>	<i>174</i>
10.2 Crystal Field Effects.....	175
11 Results and Discussion	179
11.1 The Charge State of Dopant Cations.....	180
11.2 Neutral and Singly Charged Cation Vacancies.....	182
11.3 {4:1} Clusters.....	185
11.4 Conclusions	189
References	191

LIST OF FIGURES

Figure 1. Schematic of the maximum solubility of an impurity	29
Figure 2. The fluorite structure	52
Figure 3. The 2:2:2 cluster	53
Figure 4. The cuboctahedral cluster in UO_{2+x}	54
Figure 5. Fission product sites considered in this thesis	62
Figure 6. The concentrations calculated for some important defects in a model UO_2 system	65
Figure 7. Variation of D_{Xe} with Xe concentration in nominally stoichiometric UO_2 single crystals at $T=1400^\circ\text{C}$	68
Figure 8. Variation of D_{Xe} with stoichiometry in UO_2 powders, as found by Miekeley and Felix	70
Figure 9. Variation of D_{Xe} with stoichiometry in UO_{2+x} powders, as found by Lindner and Matzke	71
Figure 10. Calculated proportion of Xe at divacancy sites in stoichiometric UO_2	77
Figure 11. Calculated proportion of Xe at U, di-, and trivacancy sites in UO_{2+x} as a function of O/U ratio	78
Figure 12. Variation of the oxygen potential of UO_2 with O/U ratio	84
Figure 13. The percentage of isolated Mo atoms occupying trivacancy sites as a function of O/U ratio and Mo concentration	95
Figure 14. Percentage of isolated Mo in di- and trivacancy sites in stoichiometric UO_2 as a function of Mo concentration	96

Figure 15. Proportion of Mo (in all charge states) present in single uranium vacancies .	98
Figure 16. Charge states of Mo in uranium vacancies.....	100
Figure 17. Breakdown of the energy contributions to Mo charge transfer reactions....	106
Figure 18. Plot of the free energy change ΔE occurring when single Mo atoms in the gas phase are added to pure urania.....	109
Figure 19. The relative partial molar Gibbs free energies of oxygen of the oxides of Ru, Rh, and Pd.....	115
Figure 20. Proportion of single atoms of Ru occupying trivacancies in urania	126
Figure 21. Proportion of single atoms of Ru occupying divacancy sites in urania.....	127
Figure 22. Proportion of single Ru atoms occupying uranium vacancy sites in urania .	128
Figure 23. Proportion of single Ru atoms occupying uranium vacancy sites as charged ions	129
Figure 24. Proportion of single Rh atoms occupying trivacancy sites in urania	131
Figure 25. Proportion of single Rh atoms occupying divacancy sites in urania	132
Figure 26. Proportion of single Rh atoms occupying uranium vacancy sites in urania .	133
Figure 27. Proportion of single Rh atoms occupying uranium vacancy sites as charged ions	134
Figure 28. Proportion of single Pd atoms occupying oxygen vacancy sites in urania ...	137
Figure 29. Proportion of single Pd atoms occupying divacancy sites in urania	138
Figure 30. Proportion of single Pd atoms occupying trivacancy sites in urania.....	139
Figure 31. Proportion of single Pd atoms occupying uranium vacancy sites in urania..	140
Figure 32. Proportion of single Pd atoms occupying uranium vacancy sites as Pd^0 and Pd^{1+}	141

Figure 33. “Free energy” change (ΔE) per atom when Ru, Rh and Pd atoms are added to urania	145
Figure 34. Plot of calculated site preference of Sr and Ba.....	154
Figure 35. Plot of energy change in system when a concentration of Sr/Ba is dissolved	156
Figure 36. Plot of $\Delta E/c$ for Sr and Ba vs O/M.....	159
Figure 37. The rock salt structure	164
Figure 38. Schematic of the {4:1} cluster	166

LIST OF TABLES

Table 1. Defect energies for UO ₂ calculated with the CASCADE program	61
Table 2. Parameters for the short range potentials of the Xe-UO ₂ system.....	73
Table 3. Shell model parameters for U, O and Xe	74
Table 4. Basic defect energies of Xe in UO ₂ calculated via computer simulation	75
Table 5. Short range potentials for Mo interactions.....	89
Table 6. Polarizability data for Mo.....	91
Table 7. Ionization potentials (in eV) used in this work.....	92
Table 8. Defect energies for Mo in UO ₂ calculated with CASCADE.....	94
Table 9. Short range potentials for Ru interactions	117
Table 10. Short range potentials for Rh interactions.....	118
Table 11. Short range potentials for Pd interactions.....	118
Table 12. Polarizability data for Ru, Rh and Pd.....	120
Table 13. Defect energies for Ru in UO ₂	122
Table 14. Defect energies for Rh in UO ₂	123
Table 15. Defect energies for Pd in UO ₂	124
Table 16. Short range potentials for Sr and Ba interactions.....	152
Table 17. Calculated defect energies for single atoms of Sr and Ba	153
Table 18. Some energy values of processes required in Chapter 8	155
Table 19. Short range interactions for the transition metal oxides.....	171
Table 20. Shell model parameters for the O ²⁻ ion in the transition metal oxides.....	172

Table 21. Perfect crystal properties for the transition metal oxides	173
Table 22. $M^{3+}-O^{2-}$ short range interactions	175
Table 23. Ionization potentials and octahedral site preference	180
Table 24. ΔE for the formation of dopant cations in the 3+ charge state.....	181
Table 25. ΔE for the formation of singly charged cation vacancies	183
Table 26. ΔE for the formation of neutral cation vacancies.....	185
Table 27. ΔE for the formation of $\{4:1\}^{5-}$ clusters.....	187
Table 28. ΔE for the formation of $\{4:1\}^{1-}$ clusters.....	188

PART 1
— METHODS

1 Introductory Remarks

In principle, a detailed knowledge of the structure of a solid on the atomic scale can be gained by recourse to the electronic theory of solids and a full quantum mechanical calculation. Indeed, where metals and highly covalent solids are concerned a realistic account of the electronic structure is often imperative. However, such calculations are computationally demanding and when defects are present in the solid, the loss of translational symmetry often makes a first principles calculation unfeasible.

For solids with a highly ionic character the situation is eased somewhat. Here it is a reasonable approximation to treat the atoms in the solid as ions of fixed charges whose interactions with each other can be specified, once and for all, by well defined potentials. This atomistic model of a solid was originally applied to the alkali halides [1] but the computational advantages of the model have also led to it being applied to solids of a less pronounced ionic nature. The availability of high speed computers means that atomistic simulation has become a powerful predictive tool applied to the study of a large range of materials (see for example [2,3]).

In this thesis the results of an atomistic simulation study of two distinct types of oxides are given. These are the fluorite structured actinide oxide UO_2 and the iron group, rock salt structured, transition metal oxides MnO , FeO , CoO and NiO . All these oxides may display some, often a large, departure from the ideal stoichiometric composition. As the crystal structure of these materials can often withstand quite large degrees of non-stoichiometry, the change in composition is accommodated by the creation of defects in the lattice. In all the oxides considered here, stoichiometry change is accommodated by point defects, including both vacancies and interstitials. Aggregation of such defects into larger clusters is, however, commonplace in these materials.

In addition to the non-stoichiometric character of the oxides considered, a second theme running throughout the course of this thesis is our interest in the behaviour of foreign atoms. In the case of UO_2 , the reason for our interest is clear. UO_2 has for years been one of the most important fuels in the nuclear reactor industry. The fissioning process in a nuclear fuel continually produces an ever increasing population of fission products. These fission products exhibit a wide range of physical and chemical behaviour in the fuel. They may precipitate as solids or as gas bubbles and some fission products will be soluble. Whatever the final destination of a fission product atom, there will, however, be a period when it exists as a single isolated atom in the fuel lattice. It is this important phase in the history of a fission product that we attempt to examine in this thesis.

In the case of the transition metal oxides, our interest focuses upon much smaller doses of foreign atoms. The defect structure of these materials has long been of interest, with clusters of defects being shown to be of importance [4]. In view of the large degrees of non-stoichiometry often exhibited by these oxides, interaction between the defects accommodating this non-stoichiometry and atoms of impurities or dopants becomes possible. This interaction can have a marked effect on the type of defects and defect clusters favoured. It is therefore of interest to investigate the ways in which a single dopant atom may interact with other defects and defect clusters in these materials.

To investigate the stability of a defect or a foreign atom at a particular site, the quantity we calculate is the defect formation energy. The commonest method used for directly calculating such quantities is quasi-static simulation, which means that, unlike a molecular dynamics approach, thermal motions are not included in the model. However, in this model, as the name implies, the lattice is not rigidly fixed. When a defect is introduced into the crystal the co-ordinates of lattice atoms are allowed to change in response to the new environment. This relaxation in the lattice geometry is a crucial factor in the calculation of reliable defect energies.

Once defect energies have been calculated, equilibrium statistical mechanics can then be used to calculate the concentration of a particular defect in the lattice. In the following chapter, the procedure adopted in calculating the thermodynamic equilibrium state of a system of non-interacting point defects is described. This is followed in Chapter 3 by an outline of the method of quasi-static atomistic simulation and the calculation of defect energies. In Part 2 of the thesis, these methods are applied to a study of the behaviour of some important fission product in UO_2 . In Part 3 we turn to a study of the transition metal oxides where calculated defect energies are used to investigate the effects of dopants on the stability of some important point defect structures.

2 Defect Statistics

2.1 Overview

To place the results of the defect calculations discussed in this thesis into some perspective, it is necessary to formulate a model which maps the detailed atomistic calculations into quantities more easily investigated through experimental work. Such a mapping is provided by statistical mechanics. In this section we discuss, in general terms, an approach to the equilibrium statistical mechanics of point defects. The approach used will follow closely that discussed by Lidiard [5].

We begin by writing the appropriate thermodynamic potential - usually the Gibbs function G - for a closed system containing N_d different types of defect, where the only degrees of freedom present are the defect concentrations themselves. In the case of the Gibbs function, this means that we fix the system pressure p and temperature T together with (in our particular case) the degree of non-stoichiometry x . This does not, however, prevent us from carrying out several separate calculations for the system with different values for these parameters.

Thus, a perfect non-defective crystal at fixed p and T ($x=0$ automatically as the crystal, as yet, contains no defects) has a certain value for the Gibbs function, $G_0(p,T)$ say. As defects (intrinsic and extrinsic) are created in this crystal the value of G will change. As a first approximation, we write this change in G as a linear function of the numbers of defects together with a configurational entropy term corresponding to the number of ways in which these defects can be arranged in the crystal. We thus write the Gibbs function for the defective crystal in the following approximate form.

$$G(p, T, \mathbf{n}) = G_0(p, T) + \sum_{i=1}^{i=N_d} g_i n_i - k_B T \ln \Omega . \quad (1)$$

Here n_i specifies the number of defects of type i (in our notation this will be the i^{th} element of the vector \mathbf{n}) and g_i is the formation energy of each of these defects, for simplicity these energies are assumed to be independent of p , T and the number of defects present¹. Ω is a combinatorial factor over all the defects. It is assumed that we can write this in a form where each of the defect populations i are independent, that is we assume that there are no site blocking effects between defects. Ω can thus be written,

$$\Omega(N, \mathbf{n}) = \prod_{i=1}^{i=N_d} \Omega_i(N, n_i) , \quad (2)$$

where each Ω_i is a function only of n_i and the system size, which is given here in terms of the number of unit cells N . The actual form of Ω_i will depend on the particular type of defect being considered. In the simplest case of a defect consisting of a single lattice vacancy or a single substitutional impurity, Ω_i may be approximately written as,

$$\Omega_i = \frac{(\beta_i N)!}{(\beta_i N - n_i)! n_i!} , \quad (3)$$

where β_i is a factor specifying the proportion of sites per unit cell at which a defect of type i may be placed. Slightly different forms for Ω_i may be required if we are considering defects for which we would need to specify an orientation as well as a position (such as a defect consisting of two bound vacancies) although often these factors may be subsumed into a single number which we shall denote below by z_i . For the simpler defects z_i will be equal to β_i . Modification of expressions (2) and (3) is often an important component in more sophisticated statistical mechanics treatments attempting to describe systems containing large defect populations (the equations given are, at best,

¹ Perhaps the independence of the g_i from the pressure p is the most reasonable part of this assumption. Assuming that g_i is independent of T and defect numbers is less satisfactory. T dependence can however be included through more involved calculation of the g_i terms. Some allowance for the effect of defect concentrations on g_i may also be added but theory here is really lacking if the defect concentrations are high.

only reasonable where defect concentrations are relatively low). However, as there exists as yet no truly satisfactory theory for systems with high defect concentrations, we keep to expressions similar to (2) and (3) for the Ω_i , although strictly speaking, at times the validity of doing this will be questionable.

The object then, is to find those values of n_i which make G as small as possible. Although we are working in the dilute limit where there are no interactions between defects, the maintenance of certain essential system constraints (such as electroneutrality) may mean that not all the n_i are independent. A simple example is given by a model system of UO_2 containing oxygen Frenkel defects as the only defects present. Here the system constraints require that for each O vacancy produced an O interstitial is also created. A common way to deal with constraints in such problems is through the use of Lagrange undetermined multipliers. The procedure is to “augment” the function to minimise with multiples of functions representing the constraints on the parameters of the function. This means that for a system with N_d defect types and N_c constraints we write a modified equation for G as

$$G(\mathbf{p}, T, \mathbf{n}) = G_0(\mathbf{p}, T) + \sum_{i=1}^{i=N_d} g_i n_i - k_B T \ln \left(\prod_{i=1}^{i=N_d} \Omega_i \right) + \sum_{j=1}^{j=N_c} \lambda_j \phi_j, \quad (4)$$

where ϕ_j is the function corresponding to the j^{th} equation of constraint and λ_j is the associated undetermined multiplier. In all the cases that will concern us here, the ϕ_j may be written as linear functions of the constrained parameters (that is the numbers of defects). We thus write,

$$\phi_j = c_{j0} N + \sum_{i=1}^{i=N_d} c_{ji} n_i = 0. \quad (5)$$

Or equivalently, in terms of the defect concentrations $[i]=n_i/N$,

$$\phi_j = c_{j0} + \sum_{i=1}^{i=N_d} c_{ji} [i] = 0, \quad (6)$$

where the c_{ji} and c_{j0} are coefficients to be specified when setting up the problem. There will be one such equation for each system constraint. The augmented Gibbs function (4) is then minimised in the normal way. This means solving the above constraint equations together with equations for the first derivatives of G . As p and T are held constant, the only derivatives left are those with respect to n_i ; i.e. $\frac{\partial G}{\partial n_i}$, the defect chemical potentials, μ_i .

$$\frac{\partial G}{\partial n_i} = \mu_i = g_i + k_B T \ln \left(\frac{[i]}{z_i} \right) + \sum_{j=1}^{j=N_c} \lambda_j c_{ji} = 0, \quad (7)$$

where we have introduced the numbers z_i which contain the information on the internal combinatorics of the defect (that is the β_i of equation (3) and the number of ways of orienting a defect at a particular site).

Solving all the equations of types (6) and (7) simultaneously provides us with the equilibrium values for the defect concentrations $[i]$. For systems containing more than a few defects, these simultaneous equations are best solved using an appropriate numerical algorithm such as the Newton-Raphson method adopted in this work. The solution to these equations is equivalent to the mass-action approach. Analytically the defect concentrations will be seen to have the following form,

$$[i] = z_i \exp \left(\frac{-g_i}{k_B T} \right) \left\{ \prod_{j=1}^{j=N_c} \exp \left(\frac{-\lambda_j c_{ji}}{k_B T} \right) \right\}, \quad (8)$$

from which equilibrium constants may be obtained if required.

The above method is satisfactory in the dilute limit. Increasing the defect concentrations however, leads to several further complicating factors that need to be considered. Of the two main problems encountered, one has already been mentioned and concerns the form for the combinatorial factor Ω . When concentrations are high both equations (2) and (3) will be incorrect; due to the blocking of sites by *all defect types*, not all the $\beta_i N$ sites will

be available for occupancy by the n_i defects. An additional problem relates to the defect formation energies g_i . These correspond to the formation of a single isolated defect in a crystal of infinite extent. Interactions between defects at high concentrations can be expected to significantly alter these energies. One approach in tackling this problem is to assume that the first two terms on the right hand side of equation (4) represent the first terms in a Taylor series expansion for G in powers of n_i (for an example of this approach see [6]). Extending this series to second order gives the necessary cross-terms but parameterization of the additional elements of the required $N_d \times N_d$ matrix presents a problem. A scaling of interactions with the square of the defect concentrations may, in any case, be hard to justify physically. An alternative approach is provided by the introduction of activity coefficients which are parameterized by some suitable physical model such as the Debye-Hückel method for the long range electrostatic interactions between defects. Even here such methods probably fail quite badly at significantly high defect concentrations [7]. Perhaps the most promising method is provided by the rather brute force application of Monte-Carlo techniques to the problem and progress has been made in this area by several authors (for example see [8]).

2.2 Defect Formation Energies

A further remark should be made concerning the defect formation energies g_i . In the next chapter we shall discuss how a particular component of these energies may be calculated through computer simulation. The energies thus obtained however, will not always describe the total energy of defect formation. For instance, when charge transfer terms are important these are incorporated through the use of tabulated ionisation potentials and if defect formation requires the displacement of a formula unit to the crystal surface (the Schottky mechanism) then the lattice energy must also be included². As an example,

² This latter term may, however, be calculated via a computer simulation.

consider the formation of the defect Mo_{U}''' in UO_2 (a Mo^{1+} ion at a U vacancy site). For the formation of this defect we can imagine that we first remove a U lattice ion to an infinite distance away from the crystal (for the moment we shall forget that we describe the crystal itself as being infinite in extent) a neutral Mo atom is then inserted, from infinity, into the vacancy thus created. We next ionise the Mo producing the Mo^{1+} . This requires the first ionisation energy of Mo, IP_{Mo}^1 (we use tabulated free ion ionisation potentials through necessity although strictly speaking, an in-crystal ionisation potential is really required). The second component of the total energy is the difference between the energy of the crystal containing one Mo_{U}''' defect and the crystal containing no defects at all. It is this energy which we calculate through computer simulation and we will denote it for the moment by $g_{\text{Mo}_{\text{U}}'''}^*$. Finally we must bring the displaced U ion back from infinity. In UO_2 it is believed that cation Frenkel defects are energetically unfavourable (see Chapter 4) formation of U vacancies thus proceeds via the Schottky mechanism. This means we should place the displaced U ion on the surface of the crystal creating a new formula unit. This lowers the defect formation energy by the lattice energy E_{lat} . The total defect formation energy is thus given by,

$$g_{\text{Mo}_{\text{U}}'''} = g_{\text{Mo}_{\text{U}}'''}^* + \text{IP}_{\text{Mo}}^1 - E_{\text{lat}} \quad (9)$$

The formation of the defect described would also require the accommodation of an electron in the crystal (as U_{U}' for instance) and also the creation of the two oxygen vacancies that were formed when we created the Schottky defect for the U vacancy. It is the system constraint equations (6) which ensure that these factors are not forgotten.

Although we shall discuss in detail the energies obtained from computer simulation in the next chapter there is one last point that should be made concerning the g_i^* . In the next chapter we shall describe a method that enables us to calculate the change in internal energy upon defect formation at constant volume. Whilst programs exist for the

calculation of the equivalent changes in the vibrational entropy, these were not available for the present work. The term g_i is thus really a misnomer in our case but it was retained in the above equations as, in principle, these free energies are amenable to calculation [9].

2.3 Solubility

Using the treatment described above we can obtain the defect concentrations [i]. In themselves these numbers can be of great use and an example of this is given in Chapter 5 where we discuss the behaviour of Xe in UO_2 . However, in most experiments the influence of the defect populations is measured indirectly. It is therefore important to attempt to derive quantities from our calculations which can be tested in experimental work. Reasonable agreement between the calculated and experimentally derived values for these quantities will then give us confidence in the understanding of processes on the atomistic scale derived from our computer simulations.

When considering the incorporation of foreign atoms into a host crystal, a quantity of importance is the maximum solubility of the impurity. This quantity will normally be quoted in units such as ppm or mol% etc. From the computational perspective it is common to give solution energies for isolated impurity atoms in the host (see for example [10]). Relating these energies to actual solubilities however is not always such a straight forward matter. In this section we give a definition of maximum solubility from the computational perspective which attempts to circumvent this problem.

Consider a pure host crystal at a certain pressure and temperature. At equilibrium this crystal will contain a certain concentration of intrinsic defects (vacancies and interstitials etc.) and have a certain value for the Gibbs function, $G_{([X]=0)}$ say (we shall drop for the moment the stating of the explicit dependence of G on p and T). If we now add an impurity X to the crystal, not only will the foreign atoms need to be accommodated but, through the system constraints, the original intrinsic defect concentrations will also be

altered. Through several paths then, the addition of the impurity will result in a new value for the Gibbs function of the crystal which, for an impurity concentration of C , we shall write $G_{([X]=C)}$. Initially however, before solution in the host, the impurity must exist in some form or other such as a gas or solid etc. (we shall assume for the moment that this form is composed only of the pure element). Each atom of X in its initial state can be said to have associated with it a free energy of g_X .

Thus considering a closed system containing the host and impurity, the difference in the free energy between the final conditions (some impurity dissolved in the host) and the initial conditions (separate host and impurity materials) is given by,

$$\Delta G = G_{([X]=C)} - G_{([X]=0)} - g_X C. \quad (10)$$

If ΔG is negative, then the incorporation of the impurity atoms at concentration C would appear to be favoured; the X atoms would be said to be soluble. Contrariwise, if ΔG is greater than zero we can assume that attempting to put such a concentration of X into the host would not result in a thermodynamically stable product. The value of C at the transition point (if such a point exists) between these two types of behaviour, for which $\Delta G=0$, we call the "maximum solubility" of X in the host. Of course we are guaranteed at least one concentration that yields $\Delta G=0$ by the trivial case of $C=0$; we are however searching for the case where $C>0$. The procedure is given schematically in Figure 1³.

Strictly speaking, the value of ΔG only tells us whether or not solution of X in the host proceeds spontaneously. Even if ΔG is always positive when $C>0$, a small amount of X will still be thermodynamically stable in the host⁴. For our purposes, however, we ignore this fraction and use the value of ΔG as our main indicator of solubility. If ΔG is always

³ This figure schematically plots the variation of the energy change of the whole crystal with impurity concentration. Normally, however, we shall plot the energy change *per impurity atom*. Examples of the type of plots produced in this case will be found in Chapter 8.

⁴ This amount will approximately be related to $\exp(-\Delta G/kT)$.

positive we say that X is insoluble in the host and similarly if ΔG is always negative we say X is soluble.

Although we have given above the case where X is in some well defined pure form before entering the host, the procedure can be extended to cases where this is not so. If X begins as some compound however, we must be sure to include terms that account for the behaviour of all parts of that compound, not just X. For example, if X begins as an oxide we must be sure to accommodate any released oxygen either in the host, or as a new X oxide, or as free oxygen; we must ensure that nothing escapes from our closed model system. The difficulty in devising a closed system which resembles an experimental one will be found in Chapter 8 to be a major obstacle in the application of this procedure.

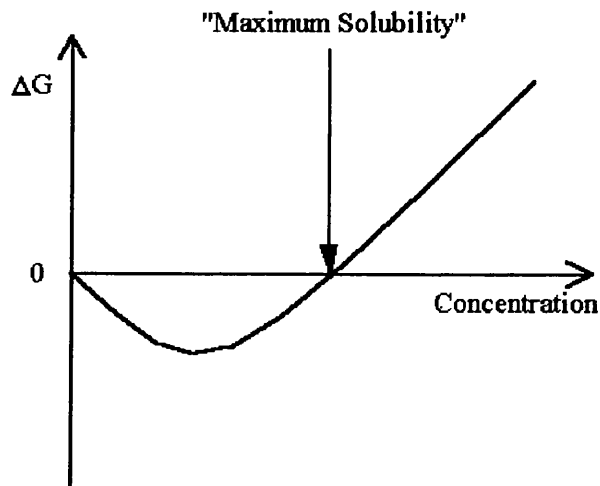


Figure 1. Schematic of the maximum solubility of an impurity. When the impurity concentration is greater than zero, the concentration which gives $\Delta G=0$ is defined here as our approximation to the maximum solubility of the impurity.

2.4 Comment

Before ending this chapter it is perhaps appropriate to make a few remarks concerning the value of carrying out the procedures discussed in this chapter. The objective of this thesis is to explore certain highly defective oxides using computer simulation. The advantage of simulation techniques is the detailed picture that can be acquired of physical processes on the atomistic scale. In seeking the detailed picture however, we cannot ignore larger scale phenomena; a defect may appear to be energetically favourable when considered in isolation but if its creation results in an increase in free energy of the total system then it may be no more than a transitory state. The treatment discussed in this chapter is an attempt to include some of the more basic factors which should be considered when trying to discover which defects are important but it is in no way exhaustive.

3 Simulation Techniques and Potentials

In the previous chapter we discussed ways in which knowledge of defect formation energies may be used to work out the defect concentrations in a system containing several different defect species. Knowing these concentrations enables us to produce a path through which the defect controlled properties of the system can be understood. In this chapter the principles behind the calculation of defect formation energies will be outlined. As such calculations have been described in detail by Catlow and Mackrodt [11], we limit ourselves here to an overview of the approach. We begin with a discussion of the simulation of a defect free, or perfect lattice and then describe the approximations used to model the same lattice when a single point defect is created. The difference in energy between the defective and perfect crystal is defined as the defect formation energy.

3.1 Simulating the Perfect Lattice

Assuming that we have a description of the interactions between the various atoms present in the crystal (the derivation of interaction potentials will be discussed later in this chapter) the simulation of the perfect crystal can begin by placing all atoms at their experimentally determined equilibrium positions. Generally, we can expect that this initial starting configuration will not correspond to the configuration of lowest energy within the simulation. When adjusting the initial configuration to one of lower energy, the change in the atomic configuration can be completely specified by giving two distinct types of quantity. The first of these will describe the change in the positions of atoms within a unit cell. These changes are specified by the displacement vectors $\delta \mathbf{r}^\alpha = \mathbf{r}^\alpha - \mathbf{r}_{\text{init}}^\alpha$ where $1 \leq \alpha \leq n$ is an index specifying the α^{th} atom in the n atom basis for the unit cell. The second quantity to consider describes how the lattice vectors

themselves are distorted between moving from the initial configuration to the new one. This is achieved by specifying the symmetrical strain matrix $\Delta\epsilon$, where

$$\Delta\epsilon = \begin{bmatrix} \delta\epsilon_1 & \frac{1}{2}\delta\epsilon_6 & \frac{1}{2}\delta\epsilon_5 \\ \frac{1}{2}\delta\epsilon_6 & \delta\epsilon_2 & \frac{1}{2}\delta\epsilon_4 \\ \frac{1}{2}\delta\epsilon_5 & \frac{1}{2}\delta\epsilon_4 & \delta\epsilon_3 \end{bmatrix}. \quad (11)$$

The new configuration may then be given by the transformation,

$$\mathbf{r}^\alpha = (\mathbf{1} + \Delta\epsilon) \cdot (\mathbf{r}_{\text{init}}^\alpha + \delta\mathbf{r}^\alpha). \quad (12)$$

Combining the $3n$ components of the displacement vectors and the 6 independent elements of the strain matrix given by equation 11 into a single $(3n+6)$ vector δ , we can write the lattice energy, U , of the crystal for a configuration \mathbf{x} (specified as internal and bulk components \mathbf{r} and ϵ) as a power series expansion in $\delta = \mathbf{x} - \mathbf{x}_{\text{init}}$ about an initial configuration \mathbf{x}_{init} ,

$$U(\mathbf{x}) = U(\mathbf{x}_{\text{init}}) + \mathbf{b} \cdot \delta + \frac{1}{2}\delta \cdot \mathbf{A} \cdot \delta + \dots \quad (13)$$

Here \mathbf{b} is a vector of first derivatives with elements given by,

$$b_i = \frac{\partial U(\mathbf{x}_{\text{init}})}{\partial x_i}, \quad (14)$$

and \mathbf{A} is a matrix of second derivatives where

$$A_{ij} = \frac{\partial^2 U(\mathbf{x}_{\text{init}})}{\partial x_i \partial x_j}. \quad (15)$$

If U were a harmonic function of δ then truncating equation 13 after second order and differentiating would give,

$$\delta = -\mathbf{A}^{-1} \cdot \mathbf{b}, \quad (16)$$

defining a vector δ which, through equation 12, would yield the exact energy minimum configuration. Generally, there will be some contribution to U from terms higher than the second order. However if \mathbf{A} is positive definite, equation 16 will still give a vector δ which will at least follow the direction towards a configuration of lower energy. We can see this by considering the sign of the gradient vector \mathbf{b} in the direction of δ , that is $\delta \cdot \mathbf{b}$. From equation 16 this is given by,

$$\delta \cdot \mathbf{b} = -\delta \cdot \mathbf{A} \cdot \delta . \quad (17)$$

Thus $\delta \cdot \mathbf{b} < 0$ providing \mathbf{A} is positive definite. When the current configuration is not close enough for the quadratic approximation to be valid we may actually over-shoot the energy minimum. However in this case, it is always possible to “backtrack” along the direction of δ to an acceptable configuration of lower energy and the procedure can be repeated until the energy minimum is found. Moreover, as soon as the system is within the harmonic region, the minimum will be located within a single iteration.

The inversion of the matrix \mathbf{A} in equation 16 requires $O(N^3)$ operations. If the inversion is carried out during each iteration, it is clear that this is a major cost in the search for the minimum energy configuration. By choosing an appropriate method for approximating \mathbf{A}^{-1} we can reduce this computational burden and at the same time ensure that the approximation to \mathbf{A} remains both positive definite and symmetrical. The method adopted in the CASCADE code [11,12], is to replace an initially accurately calculated \mathbf{A}^{-1} with an approximation \mathbf{H} on subsequent iterations. The next \mathbf{H} is related to the previous one through the addition of a correction term. There are several possibilities for this correction term in the updating of \mathbf{H} , the one used in the present work is the Davidon-Fletcher-Powell algorithm [13]. This gives the matrix for the $k+1^{\text{th}}$ iteration as,

$$\mathbf{H}_{k+1} = \mathbf{H}_k + \frac{\delta \otimes \delta}{\delta \cdot \beta} - \frac{(\mathbf{H}_k \cdot \beta) \otimes (\mathbf{H}_k \cdot \beta)}{\beta \cdot \mathbf{H}_k \cdot \beta}, \quad (18)^5$$

where $\delta = \mathbf{x}_{k+1} - \mathbf{x}_k$ and $\beta = \mathbf{b}_{k+1} - \mathbf{b}_k$. Hence, using equation 16 and replacing \mathbf{A}^{-1} with the current approximation \mathbf{H}_k , the next, $k+1^{\text{th}}$, configuration is obtained from,

$$\delta_k = -\lambda_k \mathbf{H}_k \cdot \mathbf{b}_k, \quad (19)$$

where the scalar parameter λ has been introduced to enable the use of the backtracking method mentioned earlier. \mathbf{H}_{k+1} is then derived from equation 18 and used to generate the $k+2^{\text{th}}$ configuration and the process is then repeated.

The exact details of the representation of the terms occurring in \mathbf{b} and \mathbf{A} are not discussed here. Details for the representation based on pair potentials may be found in [11] together with further specifics and amendments to the above approach appropriate in crystal simulations. Additionally, for further references on the numerical method given here, the reader is referred to Chapter 10 of [13].

Finally we note that the division of the strain vector δ into internal and bulk components allows the possibility of relaxing just the internal co-ordinates whilst keeping the lattice vectors fixed. As the lattice cell volume does not change for this process this corresponds to an energy minimisation at constant volume. It is more common, however, to allow the change of both internal and bulk components and hence carry out a minimisation at constant pressure.

⁵ Here, $\mathbf{u} \otimes \mathbf{v}$ is the direct product of the vectors \mathbf{u} and \mathbf{v} . The ij^{th} component of the resulting matrix is given by $u_i v_j$.

3.2 Crystal Properties

Once the equilibrium configuration for the perfect lattice has been found, the information contained in \mathbf{A} can be used to calculate dielectric, piezoelectric and elastic constants. When there is no permanent moment and no applied field, the lattice equilibrium condition necessitates that $\mathbf{b}=0$. Retaining this condition, when an external electric field, \mathbf{E} , is applied, equation 13 is rewritten as,

$$U(\mathbf{x}) = U(\mathbf{x}_{\text{init}}) + \frac{1}{2} \delta \cdot \mathbf{A} \cdot \delta - \mathbf{q} \cdot \delta \mathbf{r}^\alpha \mathbf{E}^\alpha, \quad (20)$$

which relates the lattice energy in the applied field to that of the field free equilibrium configuration. Here \mathbf{q} is a vector composed of the charges on the n basis atoms and $\delta \mathbf{r}^\alpha$ is a n -vector of the α components of the internal displacement vectors. The last term in equation 20 follows the convention for the double appearance of indices by implying a summation over all $\alpha=1,2,3$ components of the displacements. In equation 20, \mathbf{A} may be decomposed into separate matrices of the second derivatives with respect to the internal components \mathbf{A}_{rr} and the bulk components $\mathbf{A}_{\varepsilon\varepsilon}$ and a matrix of the mixed second derivatives $\mathbf{A}_{r\varepsilon}$.

$$U(\mathbf{x}) = U(\mathbf{x}_{\text{eq}}) + \frac{1}{2} \delta \mathbf{r} \cdot \mathbf{A}_{rr} \cdot \delta \mathbf{r} + \delta \mathbf{r} \cdot \mathbf{A}_{r\varepsilon} \cdot \delta \boldsymbol{\varepsilon} + \frac{1}{2} \delta \boldsymbol{\varepsilon} \cdot \mathbf{A}_{\varepsilon\varepsilon} \cdot \delta \boldsymbol{\varepsilon} - \mathbf{q} \cdot \delta \mathbf{r}^\alpha \mathbf{E}^\alpha. \quad (21)$$

At equilibrium we require that,

$$\frac{\partial U(\mathbf{x}_{\text{eq}})}{\partial \delta \mathbf{r}} = 0, \quad (22)$$

whence the 3 components of the atomic displacements are found from,

$$\delta \mathbf{r}^\alpha = \left[\mathbf{A}_{rr}^{-1} \cdot \mathbf{A}_{r\varepsilon} \cdot \delta \boldsymbol{\varepsilon} \right]^\alpha + \left[\mathbf{A}_{rr}^{-1} \right]^{\alpha\beta} \cdot \mathbf{q} \mathbf{E}^\beta. \quad (23)$$

Substituting equation 23 into the following expression (written here in gaussian units) for the α component of the electric displacement vector,

$$D^\alpha = E^\alpha + 4\pi P^\alpha = E^\alpha + \frac{4\pi \mathbf{q} \cdot \delta \mathbf{r}^\alpha}{V}, \quad (24)$$

produces a displacement vector with the form,

$$D^\alpha = \sum_i \lambda_i^\alpha \varepsilon_i + \sum \kappa^{\alpha\beta} E^\beta, \quad (25)$$

where we can identify the piezoelectric tensor λ and dielectric tensor κ as,

$$\lambda_i^\alpha = \frac{-4\pi \mathbf{q} \cdot [\mathbf{A}_\pi^{-1} \cdot \mathbf{A}_{r\varepsilon}]_i^\alpha}{V}, \quad (26)$$

and

$$\kappa^{\alpha\beta} = \delta^{\alpha\beta} + \frac{4\pi \mathbf{q} \cdot [\mathbf{A}_\pi^{-1}]^{\alpha\beta} \cdot \mathbf{q}}{V}. \quad (27)$$

In this last equation $\delta^{\alpha\beta}$ is the Kronecker delta. Defining the elastic constants as the second derivatives of U with respect to total strains with no applied field gives, from equations 23 and 14,

$$U(\mathbf{x}) = U(\mathbf{x}_{\text{eq}}) + \frac{1}{2} \delta \varepsilon \cdot [\mathbf{A}_{\varepsilon\varepsilon} - \mathbf{A}_{\varepsilon r} \cdot \mathbf{A}_\pi^{-1} \cdot \mathbf{A}_{r\varepsilon}] \cdot \delta \varepsilon, \quad (28)$$

whence the elastic tensor is given by

$$\mathbf{C} = \frac{[\mathbf{A}_{\varepsilon\varepsilon} - \mathbf{A}_{\varepsilon r} \cdot \mathbf{A}_\pi^{-1} \cdot \mathbf{A}_{r\varepsilon}]}{V}. \quad (29)$$

3.3 The Calculation of Defect Formation Energies

We now consider the introduction of a single isolated defect (a vacancy or an impurity atom for example) into a perfect crystal of the type dealt with above. We can expect the largest part of the disturbance caused by this process to be localised to an area fairly close to the defect. Further away, the influence of the defect will be dominated by its

effective charge and the Coulomb interaction. In this far region then, we can employ some approximation which accounts for the displacement of the ions due to the defect charge without the need for the detailed analysis required when considering the atomic displacements closer to the defect. Effectively the crystal can be partitioned into two regions; an inner region (region 1) where a very detailed account is taken of all atomic displacements and an outer region (region 2) where displacements are dealt with more approximately. This can be made explicit by partitioning the total energy E into three parts,

$$E = E_1(\mathbf{x}) + E_2(\mathbf{x}, \zeta) + E_3(\zeta) . \quad (30)$$

E_1 is the energy of region 1 and is a function of the atomic co-ordinates in the inner region specified by the vector \mathbf{x} . E_3 is the energy of region 2 and is a function of the displacements in the outer region given in ζ which in turn, as we have already implied, are themselves functions of \mathbf{x} . E_2 completes the total energy, and is the energy of interaction between inner and outer regions. It is hence a function of both \mathbf{x} and ζ .

E_3 is defined to be a quadratic function of the displacements ζ ;

$$E_3 = \frac{1}{2} \zeta \cdot \mathbf{M} \cdot \zeta . \quad (31)$$

Substituting equation 31 into 30 and invoking the equilibrium condition in ζ , we have,

$$\left. \frac{\partial E}{\partial \zeta} = \frac{\partial E_2(\mathbf{x}, \zeta)}{\partial \zeta} \right|_{\zeta=\zeta_0} + \mathbf{M} \cdot \zeta_0 = 0, \quad (32)$$

from which a modified form of equation 30 can be derived where the explicit dependence upon E_3 has been removed. That is, an expression involving only interactions occurring wholly within region 1 and those occurring between region 1 and region 2.

$$E = E_1(\mathbf{x}) + E_2(\mathbf{x}, \zeta) - \frac{1}{2} \left. \frac{\partial E_2(\mathbf{x}, \zeta)}{\partial \zeta} \right|_{\zeta_0} \cdot \zeta_0 . \quad (33)$$

The energy of the defective crystal can then be found from the condition,

$$\frac{dE}{d\mathbf{x}} = \frac{\partial E}{\partial \mathbf{x}} + \frac{\partial E}{\partial \zeta} \cdot \frac{\partial \zeta}{\partial \mathbf{x}} = 0. \quad (34)$$

In this scheme, the minimum energy configuration is assumed to have been found once the forces on all atoms in the inner region are zero ($\partial E / \partial \mathbf{x} = 0$). From equation 34 we see that this is equivalent to a total energy minimisation providing that region 2 is in equilibrium (that is providing $\partial E / \partial \zeta = 0$). The equilibrium condition then becomes,

$$\left. \frac{\partial E_1}{\partial \mathbf{x}} + \frac{\partial E_2(\mathbf{x}, \zeta)}{\partial \mathbf{x}} \right|_{\zeta=\zeta_0} - \frac{1}{2} \left. \frac{\partial^2 E_2(\mathbf{x}, \zeta)}{\partial \mathbf{x} \partial \zeta} \right|_{\zeta=\zeta_0} \cdot \zeta_0 = 0. \quad (35)$$

The next step is to introduce explicit forms for the energy terms occurring in equation 35. The full development in the case of pair potentials will again be found in [11]. However, we shall just mention here the convention employed when summing all energy contributions. The defect formation energy is defined as the energy difference between the total energy of the defective crystal and the total energy of the perfect crystal. Both of these terms may be expressed as summations over all crystal ions with the addition that the summation over the defective crystal also includes the introduced interstitials and vacancies not found in the perfect crystal summation. By using the convention that both the initial position of an interstitial (prior to its introduction into the crystal) and the final position of an atom removed to produce a vacancy are at infinity, and by treating a substituting atom as a combined vacancy and interstitial, the defect energy is written as a single summation over all ions (both those in region 1 and region 2);

$$E = \sum_{l>m} \left\{ \Phi_{lm}(\mathbf{r}_l - \mathbf{r}_m) - \Phi_{lm}(\mathbf{R}_l - \mathbf{R}_m) \right\}, \quad (36)$$

where \mathbf{R}_l is a vector for the position of an atom in the perfect crystal and \mathbf{r}_l is the

corresponding displaced position in the defective crystal. Φ_{lm} is the energy of interaction between atoms l and m.

Whilst taking care to keep to the quadratic form for E_3 in the atomic displacements $\mathbf{r}_k - \mathbf{R}_k$, it is shown in [11] that equation 30 can be written

$$\begin{aligned}
 E = & \sum_{i>j} \left\{ \Phi_{ij}(|\mathbf{r}_i - \mathbf{r}_j|) - \Phi_{ij}(|\mathbf{R}_i - \mathbf{R}_j|) \right\} \\
 & + \sum \left\{ \Phi_{ik}(|\mathbf{r}_i - \mathbf{r}_k|) - \Phi_{ik}(|\mathbf{R}_i - \mathbf{R}_k|) \right\} \\
 & - \frac{1}{2} \sum \left\{ \frac{\partial \Phi_{ik}(|\mathbf{r}_i - \mathbf{r}_k|)}{\partial \mathbf{r}_k} - \frac{\partial \Phi_{ik}(|\mathbf{R}_i - \mathbf{R}_k|)}{\partial \mathbf{r}_k} \right\} \cdot (\mathbf{r}_k - \mathbf{R}_k)
 \end{aligned} \tag{37}$$

where i and j are indices for atoms in region 1 and k indexes an atom in region 2. The full expression consists of the summation over atoms in the inner region and summations for interactions between inner and outer regions. The former is evaluated through explicit summation. The latter, however, is further broken down into two parts. The short range interactions (such as those originating from the Pauli repulsion) are most important for those region 2 atoms lying close to the inner region. Further away, the interactions between atoms in the inner and outer regions will be mostly Coulombic in nature. To take advantage of this, an interfacial sub-region between regions 1 and 2 is introduced acting as a buffer beyond which the short range interactions are not included. In this interfacial region, although displacements are approximated, interactions with region 1 are summed explicitly as in the case of region 1 atoms.

Unlike the short range interactions, Coulombic interactions between regions 1 and 2 must be calculated even for the non-interfacial part of region 2. The displacements ζ_0 are found using an approach based on the method of Mott and Littleton [1] where the region is modelled as a dielectric continuum and the ζ_0 are those induced by the effective charge of the defect centre. The method leads to a summation for the Coulomb interaction that can be performed analytically.

The approach outlined above for the calculation of defect formation energies has been implemented by Leslie [12] in the CASCADE code which follows the tradition begun by the original HADES program developed at Harwell during the early 1970's. CASCADE has been used for all the defect calculations reported in this thesis. It will be apparent from the above description that critical to the success of a simulation will be those parameters describing the interactions between atoms (the Φ in equation 37) and it is to the subject of interionic potentials that we turn to next.

3.4 Interionic Potentials

The crystal energy may be written as a summation expressed in terms of all the n-body interactions where n takes all values from 2 up to N, the total number of atoms in the crystal.

$$\Phi(\mathbf{R}_N) = \Phi_0 + \sum \Phi_{ij}(\mathbf{r}_i, \mathbf{r}_j) + \sum \Phi_{ijk}(\mathbf{r}_i, \mathbf{r}_j, \mathbf{r}_k) + \dots \quad (38)$$

Thus the energy of the configuration \mathbf{R}_N is composed of a base offset Φ_0 and a sum of all the two-body, three-body and higher order interactions. The assumption we make is that it is possible to reduce equation 38 to a form involving only two-body interactions and still obtain a reasonable approximation to $\Phi(\mathbf{R}_N)$. These interactions can then be included in the type of computer simulations already described above. It is not essential to confine the treatment to the pair potential approximation, and indeed the inclusion of three-body terms (see for instance [14]) is now routine. Such refinements have not, however, been necessary in this work. We need then, to specify a form for the pair interactions Φ_{ij} for which there are many possibilities. Assuming that we shall be dealing with predominantly ionic crystals, in addition to the important Coulombic interaction between ions we need to consider the short range repulsive forces experienced between ions as their electron clouds overlap and also the attractive force resulting from the relatively longer range effects of electron correlation; the Van der Waals force. One possible way to express

these last two non-Coulombic terms is the Buckingham form for the interaction between two ions situated at positions \mathbf{r}_i and \mathbf{r}_j

$$\Phi_{ij} = \Phi_{ij}(|\mathbf{r}_i - \mathbf{r}_j|) = A \exp\left(\frac{-|\mathbf{r}_i - \mathbf{r}_j|}{\rho}\right) - C|\mathbf{r}_i - \mathbf{r}_j|^{-6} . \quad (39)$$

The first term on the right hand side of equation 39 represents the short range electron repulsion and the second the Van der Waal interaction. Given the use of such functions, the problem becomes that of specifying the unknown parameters A , ρ and C for all the possible types of pair interactions that can occur in the system under consideration. One way in which this problem may be addressed is to make an initial estimate for these parameters and then iteratively improve this estimate based on a comparison between experimentally measured perfect lattice properties and those calculated using the current pair potential model. This is the empirical approach. Potentials developed in this way have the advantage that they already implicitly include components, such as those originating from covalency and crystal field effects, that are not fully expressible in terms of the ionic model and pair interactions. A problem may arise when we wish to employ such potentials in the calculation of defect formation energies as in this case the interionic spacings between ions close to the defect may be quite different from those present in the perfect crystal used to develop the potentials. Nevertheless, the assumption that we can use empirically derived potentials in defect calculations has worked well and by using a range of experimental data the crystal interactions can be explored for a range of interionic separations. However, the approach remains limited [15].

An alternative and sometimes complementary approach in determining potentials is to attempt to calculate the interactions between two ions. Here, however, we must be sure that for the sake of rigour we do not lose too much of the non-ideal component

mentioned earlier. A limit to the amount of time and resources that we would want to invest in determining potentials is also a factor that will determine which method we use in their calculation. An advantage of a computational approach however, is that interionic separations can be explored that would be totally inaccessible using a purely empirical technique. An approach that has found much use in previous work is the electron gas method developed by several workers but usually associated with the names of Gordon and Kim [16] (GK). As this method has been employed at several stages during the course of the work described here, we will give a brief overview of it. More detailed surveys will be found in [17,18] and the references quoted therein.

The basic philosophy behind the GK approach is that knowledge of the electron density is all that is needed to determine the energy of interaction between two ions. Although some of the functionals relating certain components of the energy to the density may be written exactly, this is not in general true and some approximations are required. The basic procedure is to begin with electron densities for each of the isolated species whose interaction we wish to investigate. These densities are usually taken as those obtained through detailed quantum mechanical calculations. The distance between the ions is fixed and the Coulomb interaction is obtained directly. The remaining part of the energy is determined from the local application of density functionals appropriate to a uniform electron gas. The fact that functionals appropriate to a uniform and not an inhomogeneous gas are used is particularly problematic for areas close to the nucleus where the wave function is rapidly oscillating. However, as electron density overlap of the two ions is relatively small for the near nuclear region, the homogenous approximation is really mostly an issue in the case of the valence shells, where its use is more valid. When electron densities of the two atoms overlap the densities are assumed to be additive; this point is discussed further in [17], but essentially this assumption is reasonable for interactions between closed shell species. For open shell species, where significant rearrangement of electron distributions may take place, the GK method enjoys

less success. However, where the overlap is largely restricted to the closed shells the approach can still be a useful one.

The use of the GK approach has found some success in calculating highly ionic interactions between closed shell ions. The extrapolation of the method to the study of oxides however, is not without its difficulties, and many authors have been forced to introduce some form of adjustment to their basic GK potentials in order to obtain results in reasonable agreement with experiment. Unfortunately, it is not always clear what value lies in the use of such adjusted potentials. Although attempts were made to apply the GK method directly to the studies reported in this thesis, neither in the study of fission products in UO_2 nor in the study of dopants in transition metal oxides was the method found to be satisfactory. The solution adopted in both cases was to use an amalgam of the GK and empirical methods. This is discussed at the end of this chapter.

Before ending our discussion of the GK method, one further point should be made concerning the origins of the electron densities used in the approach. There are essentially two ways in which these densities are usually derived. The first method involves expansion of tabulated analytic basis functions obtained from an accurate Hartree-Fock calculation for the isolated atom. In the second approach the wave functions and hence the densities are calculated numerically, the wave functions and atomic potentials being solved self-consistently (in the present work the HERSKILL program of Harding and Harker [18] was used in implementing this second method). In this latter method relativistic effects, important for larger atoms, may be added using a suitable approximation [19]. It is also important that during the calculation the atom may be embedded in an external potential modelling the Madelung field for the appropriate crystal site. The importance of making some allowance for the crystal field has long been recognised and is of particular relevance when considering the more diffuse anions. A similar scheme can also be applied with the analytical method, where the coefficients of the tabulated basis functions are recalculated for the particular external potential.

Computer programs implementing the GK method described above have been written at Harwell Laboratory and are discussed in the report by Harding and Harker [18].

The GK method includes functionals for the electron correlation energy which are only valid at short ranges. At longer range, where a density functional approach is inappropriate, these functionals cannot be used. The long range, or dispersive interaction, is best described by a multipole expansion, the first term of which, for instantaneous dipole-dipole interactions, is included as the last term in the Buckingham form given in equation 39. When using the empirical approach, this interaction is included automatically, although in this case the resulting numerical value for the parameter C may not give much insight into the true relevance of the dispersive interaction; the sum effect of all the various components of the total interaction will be spread across all three parameters A, ρ and C. In the case of the GK method it is probably best that the resulting interaction is fitted only to the exponential part of equation 39 and that the C parameter is then set using some other means.

One way in which the C parameter may be found has been described by Fowler and co-workers [20] and is based on the early theoretical work on the dispersive interaction by Slater and Kirkwood [21]. The C parameter for the interaction between two atoms i and j, is expressed as a function of the atomic polarizabilities α , and the number of electrons, P, that make a significant contribution to that polarizability.

$$C_{ij} = \frac{3\alpha_i\alpha_j}{2 \left[\left(\frac{\alpha_i}{P_i} \right)^{1/2} + \left(\frac{\alpha_j}{P_j} \right)^{1/2} \right]} \quad (40)$$

Both experimental and computed values for the polarizabilities of several of the ions of interest in this work exist. For the most part, however, this is not the case. In cases where no value for α can be found in the published data tables we used an interpolation scheme between ions of known polarizabilities using the assumption that the polarizability scales

with ionic volume. The electron numbers P are also not so easy to find and here Fowler and co-workers have suggested that the value appropriate to the isoelectronic rare gas be used. Clearly this is not always possible with the materials under consideration in this thesis and hence the nearest approximate rare gas is used as a guideline. In equation 40 however, the error in P is of less importance than that in α .

As we have already stated, the GK method used on its own has often been found to be unsuitable in the study of certain materials. It is also often the case that it is not possible to develop empirical potentials due to the lack of any appropriate experimental data or system (which is unfortunately the case for many of the UO_2 fission products considered in this work). Where both these problems occur, it is still possible to use a combination of the GK and empirical approaches to produce reasonable potentials and, significantly, produce them in a consistent manner. The approach was first used in studies by Butler and co-workers [22] and assumes the existence of good empirical potentials for the host lattice that are used as a reference base. The remaining interactions (i.e. those between host and impurity ions) are determined as potentials which differ from the host reference potentials by a defined amount. This difference is taken to be the same as the difference between the equivalent set of calculated GK potentials. Hence, the energy of interaction between ions i and j , where i and k are host ions and j an impurity is given by

$$\Phi_{ij} = \Phi_{ik}^{\text{empirical}} + \Phi_{ij}^{\text{GK}} - \Phi_{ik}^{\text{GK}}. \quad (41)$$

As this thesis considers only binary oxides, i and k are always taken to be the different host species. In the following chapters, we shall refer to the above approach as “empiricizing”.

We have thus far discussed two methods used for producing interionic potentials suitable for computer simulation work, namely the empirical and GK approaches. These methods were concentrated upon as they were the methods used in the current work. However they are not the only possibilities available. Much recent progress has been made on the

determination of potentials from detailed quantum mechanical studies (see for example [23] and [24]). Although many of the problems mentioned in the above paragraphs have direct parallels in these more numerically intensive approaches, these methods do promise a future improvement in the quality of interionic potentials.

3.5 Ionic Polarizability

Although some allowance for the effect of ionic polarizability can be included in the short range interaction potentials, for accurate defect energy calculations this approach alone is unsatisfactory [25]. An early attempt to model the effect of ionic polarizability was the Point Polarizable Ion model where the dipole moment of an ion is given by,

$$\mu = \alpha E, \quad (42)$$

where α is the ionic polarizability and E the electric field. A problem may arise however, when the mutual polarization fields of a pair of interacting ions causes their respective dipole moments to increase without bound. This problem arises due to the failure of the model to include the polarization limiting effect of electron cloud overlap. An advance can thus be made by including into a model of ionic polarizability the interdependence of the short range interactions and ionic polarizabilities.

The most common method used for introducing ionic polarizability into simulation work is the shell model due to Dick and Overhauser [26]. The essential idea behind this is that each ion is modelled as a central core containing all the mass of the ion which is harmonically coupled to a massless charged shell. The sum of the charges on core and shell is fixed to the total charge of the ion. The short range interaction between two ions acts between the massless shells thus coupling this interaction to the ionic polarizabilities and avoiding some of the problems associated with the Point Polarizable Ion model. The model is summed up by the following equation for the polarizability of an ion.

$$\alpha = \frac{cY^2}{k}, \quad (43)$$

where Y is the charge on the shell and k is the coupling force constant for the restoring force between core and shell. The constant c depends on the units used for the previous quantities. Commonly Y and k will be fitted empirically to give reasonable perfect crystal dielectric constants; the high frequency dielectric constant is particularly relevant here. An alternative approach is to use the α and P parameters of equation 40 as the values for α and Y . This latter approach is favoured in cases where the empirical method is not easily applied.

3.6 Summary

We end this chapter with a brief note on how the methods described above have been employed in the defect energy calculations reported in this thesis. Essentially the problem presented by our two studies (fission products in UO_2 and dopants in transition metal oxides) is the same. In each case we have empirical potentials of proven worth for the interactions between host ions, and need to derive potentials for the interactions of other ions which often are not easy to obtain empirically. The chosen solution in both cases is to derive the foreign ion interactions using the empiricizing approach mentioned above whilst retaining the full empirically derived potentials for the host ion interactions.

For the shell model of ionic polarizability and the Slater-Kirkwood approach to long range dispersive interactions, we use tabulated values for the ionic polarizabilities where these data are available. Unknown values are inferred through interpolation between known data. Whilst in most cases our model for foreign ions cannot be checked against experimental data, where a comparison with previous simulation work is possible, the results reported in this thesis are found to be in good agreement with the older work.

PART 2
— FISSION PRODUCTS IN UO₂

4 Introduction

UO₂ has been much studied from both experimental and computational perspectives. Focus has particularly centred upon its major role as a fuel in nuclear reactors (either alone or with PuO₂ in mixed fuels) and it is this aspect of its practical use that provides an impetus for much of the continued interest. Additionally, the material itself displays many intriguing features which are of interest in their own right. In this part of the thesis, details of the results and interpretation of computer simulation studies into the behaviour of several important fission products in urania are given. The procedures used are those outlined in Part 1; that is, calculation of defect energies through energy minimisation techniques (Chapter 3) followed by estimation of defect concentrations using a simple equilibrium statistical mechanical model (Chapter 2).

When considering the results given in the following chapters it is well to remember the complexity of the problem. The operational reactor fuel may contain high concentrations of many different fission products, each exhibiting its own distinct physical and chemical behaviour. Large scale damage due to the fissioning process, dislocations, bubbles and precipitates all need to be accommodated within the fuel. Extreme conditions of local melting may occur near the paths of fission products allowing processes which would not normally be predicted for a fuel at its operating temperature. Simplifications can, however, be made, both in experimental and computational work, and it is remarkable how successful these often prove in providing results of direct relevance to the real fuel. Before discussing the simplifications introduced into the present study, a brief discussion of the current knowledge on urania is given. The literature is extensive, so we shall restrict ourselves to outlining the main points of general relevance to the work in this thesis. More detailed discussion of particular points will be found in the relevant chapters that follow.

4.1 Outline of Experimental Knowledge

4.1.1 Basic Solid State Chemistry

At room temperature and normal reactor operating temperatures, UO_2 is a semiconductor exhibiting the fluorite structure (see Figure 2). This structure is maintained over a wide range of non-stoichiometry, both oxygen deficiency and excess, and is also robustly retained in the presence of quite large concentrations of impurities. This robustness of structure is one of the attractive features of UO_2 as a nuclear fuel.

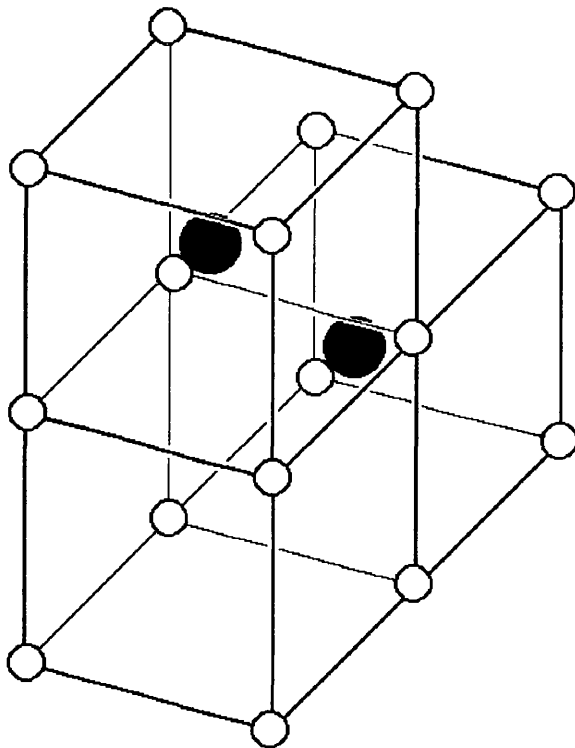


Figure 2. The fluorite structure. The anion sublattice is shown with anions indicated by white circles. The face sharing cubes formed by the anion sublattice alternate as being either occupied by a cation (black circles) or empty (the interstitial site).

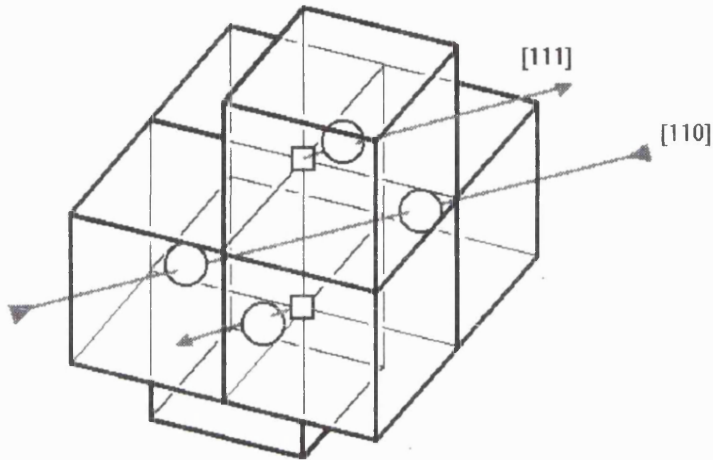


Figure 3. The 2:2:2 cluster. This has been proposed as a means of accommodating excess oxygen in UO_{2+x} . The white circles indicate the four oxygen interstitial, two of which are displaced away from oxygen vacancies in [111] directions, the other two are displaced inwards in [110] directions. White squares indicate the two vacancies on the oxygen sublattice. Anions and cations at normal crystal sites are omitted.

Although oxygen excess is undoubtedly accommodated in the vacant interstitial sites shown in Figure 2, neutron diffraction studies of $\text{UO}_{2.12}$ [27] have suggested that at high degrees of oxygen excess two types of position, displaced from the centre of the interstitial site, are occupied in equal proportions. In addition to these, the presence of oxygen vacancies was also found, again in equal proportion to the oxygen situated at each of the interstitial sites. To account for these observations, the 2:2:2 cluster (Figure 3) of oxygen interstitials and vacancies has been proposed with more complex clusters becoming possible as the $\text{UO}_2/\text{U}_4\text{O}_9$ phase boundary is approached (see [27] for

further details). From work on the β phase of U_4O_9 [28] it has been proposed that a cuboctahedral cluster (Figure 4) may have a role to play in the defect structure of UO_{2+x} , although a simple model based on this structure is incompatible with the observed site occupation numbers in $UO_{2.12}$ [27]. For small degrees of oxygen excess it is less likely that clustering is of importance.

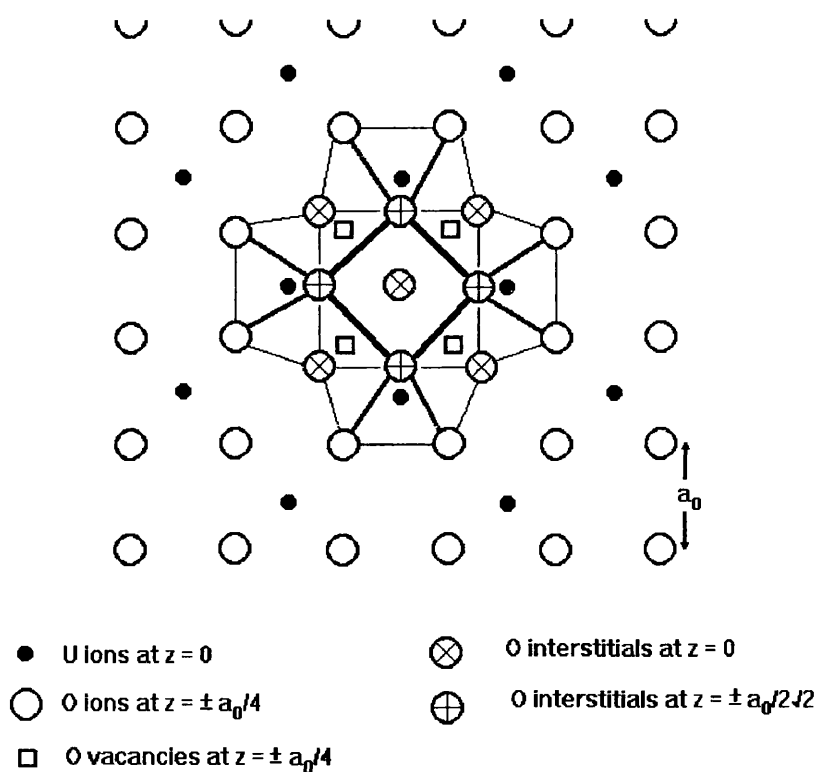


Figure 4. The cuboctahedral cluster in UO_{2+x} . For a fuller explanation of its structure and relationship to the fluorite crystal, refer to [27].

As oxygen excess is accommodated at interstitial sites, whilst the uranium sub-lattice is not disrupted [27], it can be deduced that the oxygen Frenkel is the main form of intrinsic atomic disorder. Oxygen diffusion data on UO_2 and UO_{2+x} have provided an estimate of the oxygen Frenkel defect energy of about 3-4eV, although the basis for the derivation of these values is not without some dispute (see Catlow [29] and below). The Schottky

defect energy is estimated to be somewhat higher at 6-7eV, whilst the U Frenkel energy is placed prohibitively high at 9.5eV [30].

In common with the other fluorite structured crystals, urania exhibits a pre-melting transition that appears to be intimately connected to oxygen interstitials and disorder on the oxygen sub-lattice [31]. The transition is signatred by an anomaly in the high temperature ($\sim 0.85T_m$) specific heat capacity which continues to be the subject of detailed studies [32]. This anomaly is, however, small compared to the electronic contribution to the specific heat which probably takes the form of the thermally induced electronic disorder, $2U^{4+} \rightarrow U^{5+} + U^{3+}$ [29,33]. An enhancement of the creep rate of UO_2 at high temperatures is possibly associated with the 'Bredig' transition and was probably responsible for the erroneously low melting point that was initially quoted in the literature on UO_2 [34].

The importance of electronic disorder in UO_2 has been highlighted by Hyland and Ralph [33]. A hole is usually taken to mean a 5f small polaron localised on a U^{5+} site and, although it has been suggested [35] that an excited electron may be itinerant in bands formed from 6d orbitals, Hyland and Ralph have cited strong reasons to suppose that *thermally* excited electrons will be present as 5f small polarons on U^{3+} sites.

4.1.2 Fission Product Behaviour

Due to the technological importance, it is not surprising that much work has been carried out on the behaviour of fission products in urania. In addition to fission products soluble in the fuel (these include particularly the rare earths), three main types of precipitate are observed [36]; rare gas bubbles, mainly of Xe and Kr; ceramic phases, often described as a perovskite type oxide of Ba, Sr, Zr, Mo and U [37]; and metallic phases, primarily alloys of the metals Mo, Tc, Ru, Rh and Pd. The chemical behaviour of the main fission products has been reviewed by Kleykamp [36], who has also recently reviewed the literature on fission product solubilities [38]. Before joining any precipitates however

(and during any phase of fission induced resolution), a fission product atom will spend at least some time isolated in the fuel matrix. It is this important stage in fission product behaviour which is investigated in this thesis.

Although much is known of the behaviour of many of the fission products, there remain uncertainties. For example, the diffusion of Xe in urania has been extensively studied for many years but there are still substantial disagreements between the various values proposed for its diffusion constant (see the review of Matzke [39]). The cause for much of the uncertainty undoubtedly lies in the necessity to control carefully the many factors which influence fission product behaviour. Primary among these are the stoichiometry, fission product concentration and radiation damage. Although these last two factors are inextricably linked we show in Chapter 5 that the Xe concentration does indeed play an important role in its own right.

Although much effort has been expended in the post-irradiation examination of real fuels, the difficulties in handling highly active samples has, in part, led experimentalists to the use of additional complementary methods. These include ion implantation of selected fission products (and possibly additional oxygen to investigate the effects of stoichiometry changes) and the use of simulated fuels (SIMFUEL) prepared from unirradiated UO_2 and selected fission product additives [37]. Both of these approaches represent a simplification of the real problem that enables major processes important for individual fission products to be isolated and examined.

Although information on the nature of the sites occupied by single fission product atoms have been provided by channeling experiments (see, for example Matzke and Davies [40]) detailed knowledge of fission product behaviour on the atomic scale has primarily relied upon computational work.

4.2 Outline of Previous Computational Work

In addition to experimental investigations, theoretical and computational work provide a complementary approach to the investigation of UO_2 and fission product behaviour. In this section we outline some of the important work of the latter type carried out in investigating, at the atomic scale, the properties of various point defect structures in the material.

With the development of efficient computer codes and reliable models of interionic potentials, it became possible to make realistic attempts to calculate the energies of some important point defects in UO_2 . It was realised at an early stage [29] that a simple point polarizable ion model would not be sufficient for reliable defect energies to be calculated. The first comprehensive studies of defect energies in UO_2 using the shell model were carried out by Catlow and Lidiard [41] and Catlow [29] using the HADES computer code (which is based on the Mott-Littleton method for defect simulation outlined in Chapter 3). In these calculations the oxygen Frenkel (consisting of doubly charged vacancies and interstitials) was confirmed as the major form of intrinsic atomic defect. Although the formation energy calculated ($\sim 5\text{eV}$) was somewhat high compared to that suggested by experimentalists, it was claimed that the experimental value was derived on the mistaken assumption that the mechanisms of oxygen diffusion in UO_2 and UO_{2+x} were identical. Activation energy calculations were presented which suggested this assumption was incorrect. The possibility of oxygen Frenkels formed from singly charged defects was investigated but this was less favoured than the doubly charged case by about 4eV . Although the calculated formation energy of a Schottky trio ($\sim 10.3\text{eV}$) was again calculated to be significantly higher than that suggested from experiment, the value was in line with that calculated for the oxygen Frenkel (see discussion at the end of [41]).

Although the oxygen Frenkel was calculated as the main form of atomic disorder, the electronic transfer process,



was found to be even more energetically favoured and thus in stoichiometric UO_2 this type of electronic disorder was suggested to be more pervasive than oxygen Frenkel formation [29]. As mentioned above, the consequences of this for the thermodynamic data has been investigated by Hyland and Ralph [33].

Catlow and Lidiard also investigated the more complex aggregates of point defects thought to be possible in UO_{2+x} . These included the 2:2:2 cluster mentioned above and some other related clusters. The 2:2:2 cluster was found to be stable.

A more recent investigation of defect energies in UO_2 was carried out by Jackson and co-workers [42]. This was essentially a re-examination of many of the problems studied by Catlow and Lidiard, using an enhanced model for the interionic potentials which gave a much improved agreement with thermal expansivity data. Their work also included a calculation of enthalpy and vibrational entropy terms which was not attempted in the previous studies. The potentials derived by these authors probably represents the most reliable model for defect calculations that is at present available in the literature and have been adopted in this thesis as the basis for all calculations concerning UO_2 . The calculated value for the formation of an oxygen Frenkel defect ($\sim 4.7\text{eV}$) was a little lower than that of Catlow and Lidiard whilst the Schottky energy was somewhat higher ($\sim 11.3\text{eV}$). Curiously, whilst the Schottky energies calculated by both Jackson and co-workers and Catlow and Lidiard were substantially higher than the value suggested by experimentalists, the energy for the bound Schottky trio (or trivacancy, see below) of $\sim 7.3\text{eV}$ calculated by Jackson and co-workers appeared to be in quite good agreement with the experimental value.

Comparing their calculated values for the binding energies of the 2:2:2 and cuboctahedral cluster, Jackson and co-workers found they could not distinguish a favoured cluster and it was suggested that both may be present in oxygen excess UO_2 .

The values derived in such defect energy calculations have been employed in theoretical studies of the Bredig transition in UO_2 [34]. To investigate this problem properly a simple statistical mechanical model of the type outlined in Chapter 2 is no longer appropriate. Extra energy terms due to defect interactions and a modification of the configurational entropy to allow for site blocking effects are required. A direct attempt to study the Bredig transition has been made using molecular dynamics with interionic potentials based on those of Jackson and co-workers [43].

Due to their importance, the first fission products to be investigated using energy minimisation techniques were the rare gases Xe and Kr [44]. This work was subsequently followed up by several authors including Grimes and Catlow [10] who carried out a general survey of fission product behaviour covering many of the important fission products.

4.3 Overview of Part 2

Although there is undoubtedly an appreciable covalent character to the bonding of UO_2 and some have questioned the legitimacy of assigning formal charges (U^{4+} and O^{2-}) to the ions [45] the work of Catlow, and Jackson and co-workers has shown that computations based on an ionic model of UO_2 give results in substantial agreement with experiment, providing care is taken in the derivation of the interionic potentials. In this part of the thesis, defect energy calculations are based on the interionic potentials of Jackson and co-workers for the UO_2 lattice [42]. Interactions with fission products are obtained using the “empiricizing” method outlined in Chapter 3.

The energy of incorporating a fission product atom in UO_2 is calculated for the atom at various sites. To restrict the calculations needed to a feasible number, it is necessary to restrict attention to a few basic sites that are important at relatively low defect concentrations. Interactions of fission products with large defect clusters are not considered in this thesis as the simple statistical mechanical model outlined in Chapter 2

will be too crude for such cases. In the following chapters we shall often present graphs showing the variation of some property with O/U ratio or fission product concentration where, to illustrate the behaviour found in the model system, the graphs may extend quite far into the high O/U or concentration region. It should always be remembered when inspecting these graphs that, at high O/U ratios and fission product concentrations, a more sophisticated treatment would show that the system behaviour will depart from our simpler model, due to the effects of defect-defect interactions, site blocking and cluster formation. Nevertheless, our results provide a useful basis for analysis of the behaviour of such systems.

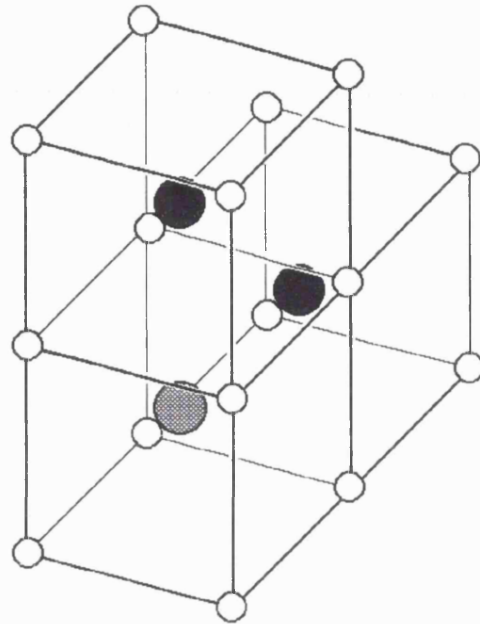
As the fission products investigated in this thesis generally exhibit little solubility in UO_2 , the limitations just outlined are not a major problem; much of the interesting behaviour occurs at or near stoichiometric composition. In line with this focus on low O/U ratios, fission product atoms located at sites built up of only a few lattice vacancies are considered. These are the oxygen vacancy, the uranium vacancy, the divacancy (a bound oxygen and uranium vacancy pair) the trivacancy (a bound Schottky trio) and the tetravacancy (a cluster consisting of two oxygen and two uranium vacancies). Additionally, calculations are performed for fission product atoms located in the large interstitial site. All of the above sites are shown schematically in Figure 5.

The question of which particular site it is most energetically favourable for a fission product to occupy depends, in part, on the ease with which the site may be formed. The computed concentrations of these sites as a function of O/U ratio in UO_2 containing no fission products is given in Figure 6. The data for this figure was obtained using the statistical mechanical model of Chapter 2 together with defect energies calculated with the CASCADE program. These energies are reported in Table 1. It will be seen that site concentrations are heavily dependent upon the O/U ratio, the effect being particularly marked near stoichiometric composition. The importance of the O/U ratio is a recurring theme in this part of the thesis.

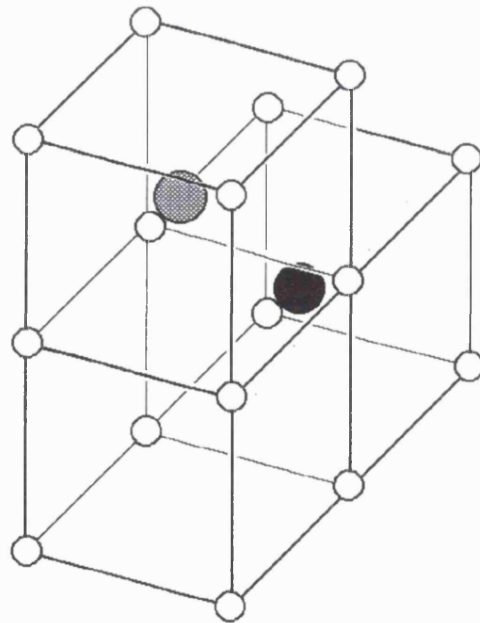
We begin, then, in Chapter 5 with a re-examination of the problem of Xe in UO_2 where we find an important Xe behaviour dependency upon Xe concentration. In Chapter 6 we present first calculations of Mo defect energies. The behaviour, on the atomic scale, of this enormously important fission product has, until now, received little attention in computational work. In Chapter 7 the related fission products Ru, Rh and Pd are investigated. Finally, as a check to our calculations, in Chapter 8 the calculated solubility behaviour of Sr and Ba is compared to known experimental data.

Defect	Energy (eV)	Defect	Energy (eV)
O interstitial	-12.26	tetravacancy	187.69
O vacancy	17.08	U^{3+} at U site	35.25
U vacancy	80.22	U^{5+} at U site	-46.04
divacancy	94.88	U^{6+} at U site	-105.23
trivacancy	110.50		

Table 1. Defect energies for UO_2 calculated with the CASCADE program. Not included in the table but needed in the analysis used in this report is the UO_2 lattice energy. This was calculated as 103.14eV.

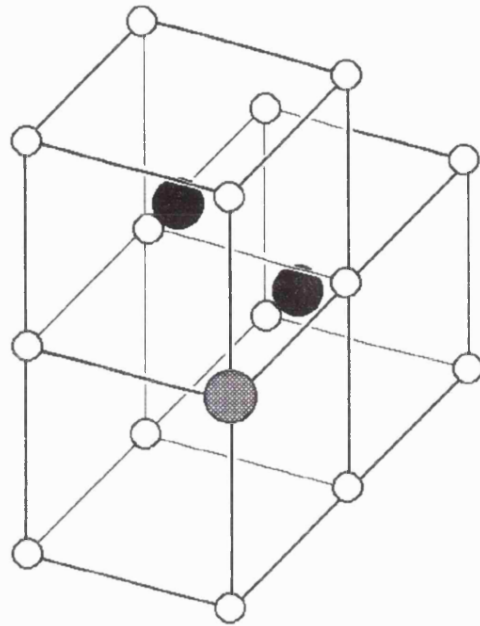


a)

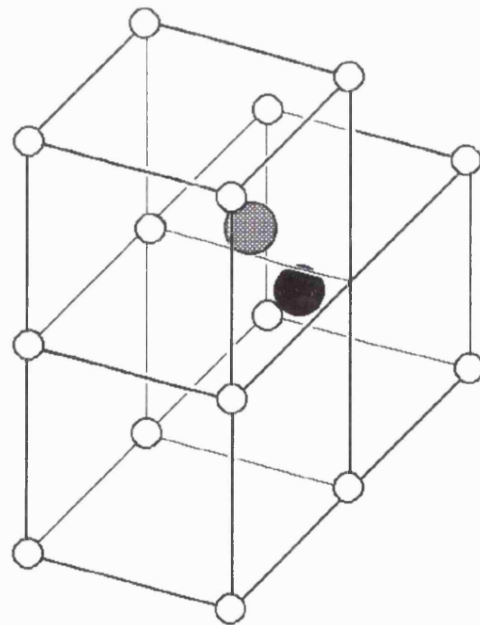


b)

Figure 5. Fission product sites considered in this thesis. a) Interstitial site, b) U vacancy site. Grey circle indicates fission product atom, black U atoms and white O atoms. Continued overleaf.

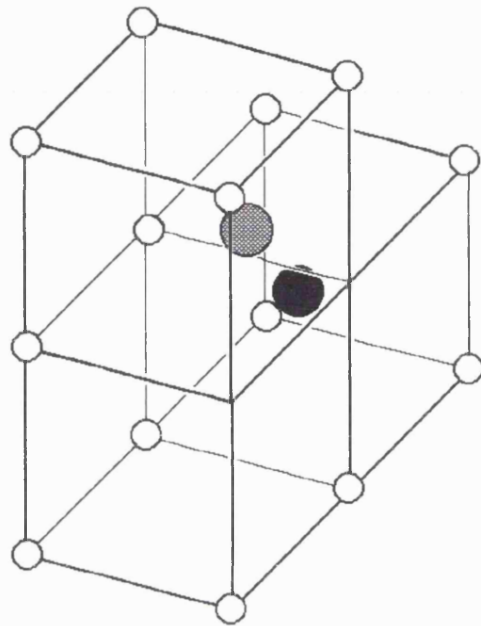


c)

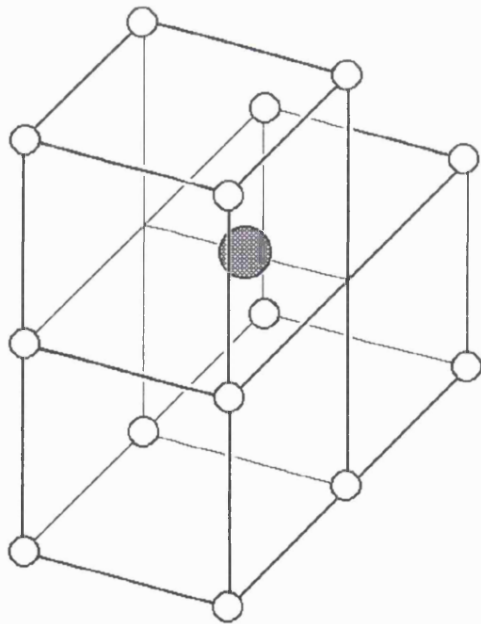


d)

Figure 5 continued. c) O vacancy site, d) divacancy site.



e)



f)

Figure 5 continued. e) trivacancy site, f) tetravacancy site.

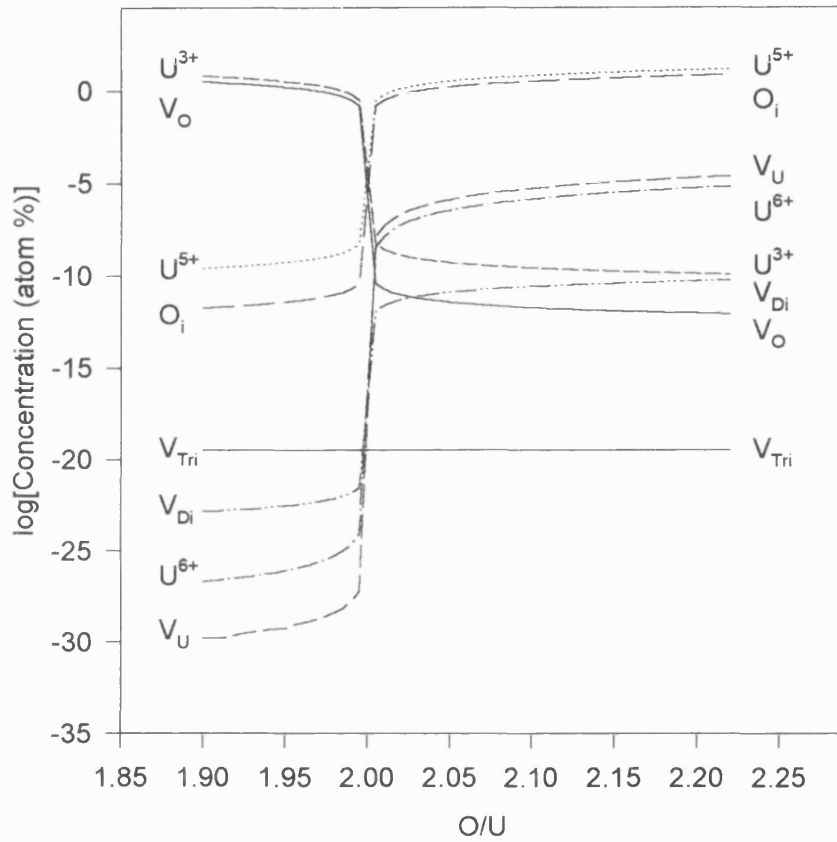


Figure 6. The concentrations calculated for some important defects in a model UO_2 system. An adapted Kröger-Vink notation is used where V_Di and V_Tri are the di and trivacancy respectively.

5 Xe

5.1 Introduction

As one of the major fission products, the behaviour of Xe in uranium dioxide has been a focus of considerable experimental and theoretical attention since the early days of the nuclear industry. Concern has particularly centred on its important role in fuel swelling and this has accordingly led to a desire to obtain a greater understanding of the basic processes governing its migration and trapping within the fuel.

There are many factors which determine the behaviour of Xe in nuclear fuels and it is not our intention to discuss all of these (a review of the most important points will be found in [39]). Here rather we shall confine ourselves, in the main, to an investigation of the effect of Xe concentration on the behaviour of single isolated atoms of Xe in stoichiometric UO_2 . In this study the focus is on the low dose region and hence an investigation of bubble formation and trapping in large radiation induced defects is not included.

5.2 Experimental Knowledge and Previous Computational Work

A point that comes to attention when viewing the existing experimental data on Xe diffusion, is the wide range present in the quoted diffusion coefficients D_{Xe} . This large spread in the often contradictory experimental data was drawn attention to by MacEwan and Stevens [46]. These authors investigated several factors which they believed to have an important effect on D_{Xe} and which should therefore be subject to control in any experimental work. In particular, and of special relevance to this chapter, they investigated the important influence of the fission dose and hence also the Xe

concentration. In their experiments on single crystals and sinters of nominally stoichiometric UO_2 , they found a dramatic decrease in D_{Xe} once the fission dose exceeded 10^{15} fissions/ cm^3 or equivalently a Xe concentration in the region of 10^{-6} atom % (all concentrations will be given as a percent of U+O atoms). Their data for D_{Xe} in single crystals of UO_2 has been reproduced in Figure 7.

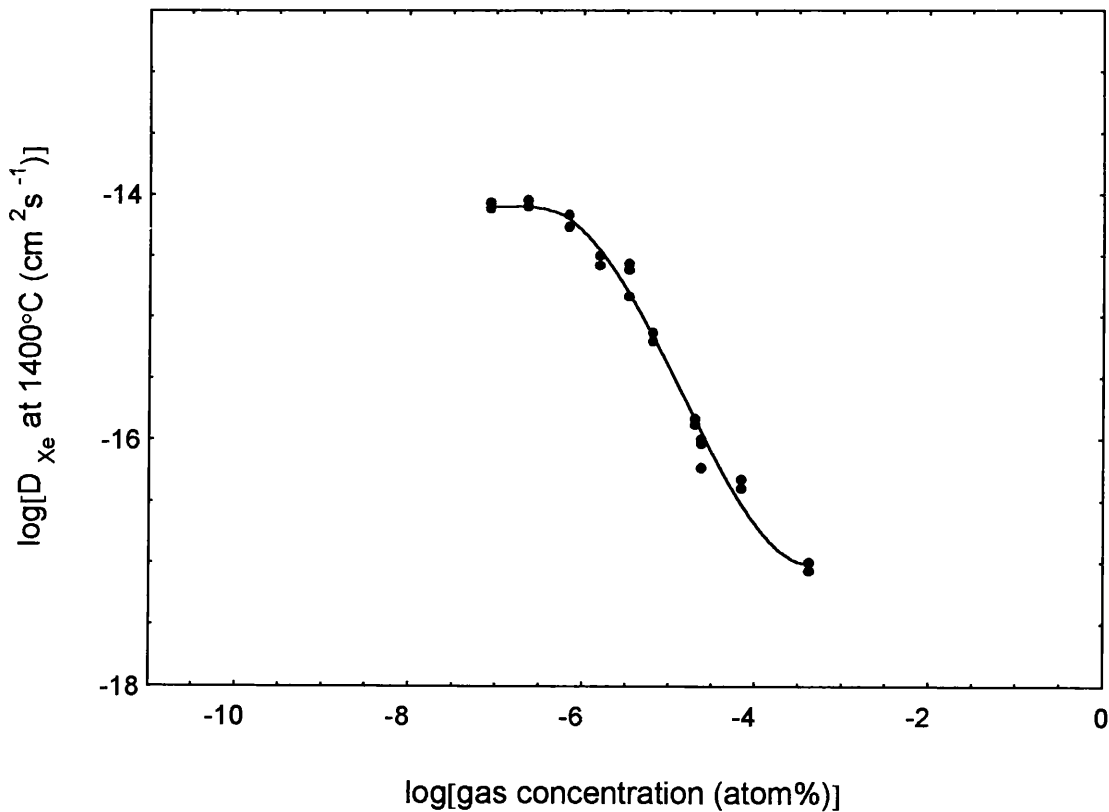


Figure 7. Variation of D_{Xe} with Xe concentration in nominally stoichiometric UO_2 single crystals at $T=1400^\circ\text{C}$. Redrawn from MacEwan and Stevens [46].

The data of MacEwan and Stevens signify the onset of Xe atom interaction with fission induced radiation damage. Such an interaction is an inevitable consequence of the insolubility of Xe in uranium dioxide and clearly, during the course of an experiment, we would expect the importance of this interaction to be heavily dependent upon the damage induced defect concentration. In addition to the effect of radiation damage, at large fission doses, we would expect that a single Xe atom would be increasingly likely to encounter other gas atoms and hence form a nucleus for a fission gas bubble. At the fission dose range focused upon in this chapter however, this second effect is probably less important than the trapping of gas by radiation damage induced defects but its importance will grow with increasing gas concentration. The main intention of this chapter is to show that in addition to the two factors just mentioned, the trend shown in the data of MacEwan and Stevens conceals a parallel change, as a function of Xe concentration, in the location of single atoms of Xe not trapped by radiation damage.

On a theme somewhat different to that of the work of MacEwan and Stevens, in a paper reporting extensive data on both stoichiometric and non-stoichiometric uranium dioxide, Miekeley and Felix [47] found that they could divide their Xe diffusion data into three groups corresponding to UO_{2-x} , UO_2 and UO_{2+x} . Each of these three groups had its own particular value for D_{Xe} but within either of the two non-stoichiometry groups, the actual value of x was found to be unimportant. This last result contrasted with the work of Lindner and Matzke [48], which had demonstrated some years previously a clear dependence of D_{Xe} on the magnitude of x in UO_{2+x} . The results of both these studies are given in Figures 8 and 9. Again [39] should be consulted for a discussion of some of the experimental difficulties which may have contributed towards these apparently contradictory data.

Experimental work on Xe release from doped UO_2 and channelling experiments with Rn implanted UO_2 [49,40] had led to the suggestion that Xe diffuses in trivacancies (that is, bound Schottky trios consisting of a uranium vacancy and two oxygen vacancies, see

Chapter 4). The nature of lattice sites for Xe in UO_{2+x} was later explored from a computational point of view by Catlow [44] who concluded that in UO_{2-x} and UO_2 isolated atoms of Xe would be located in trivacancies. In UO_{2+x} however, he suggested that Xe would be most likely to occupy single uranium vacancy sites. This work was later supported by Ball and Grimes [50] and Grimes and Catlow [10] who found that the divacancy (one uranium and one oxygen vacancy bound together) may also be an important Xe site in stoichiometric UO_2 .

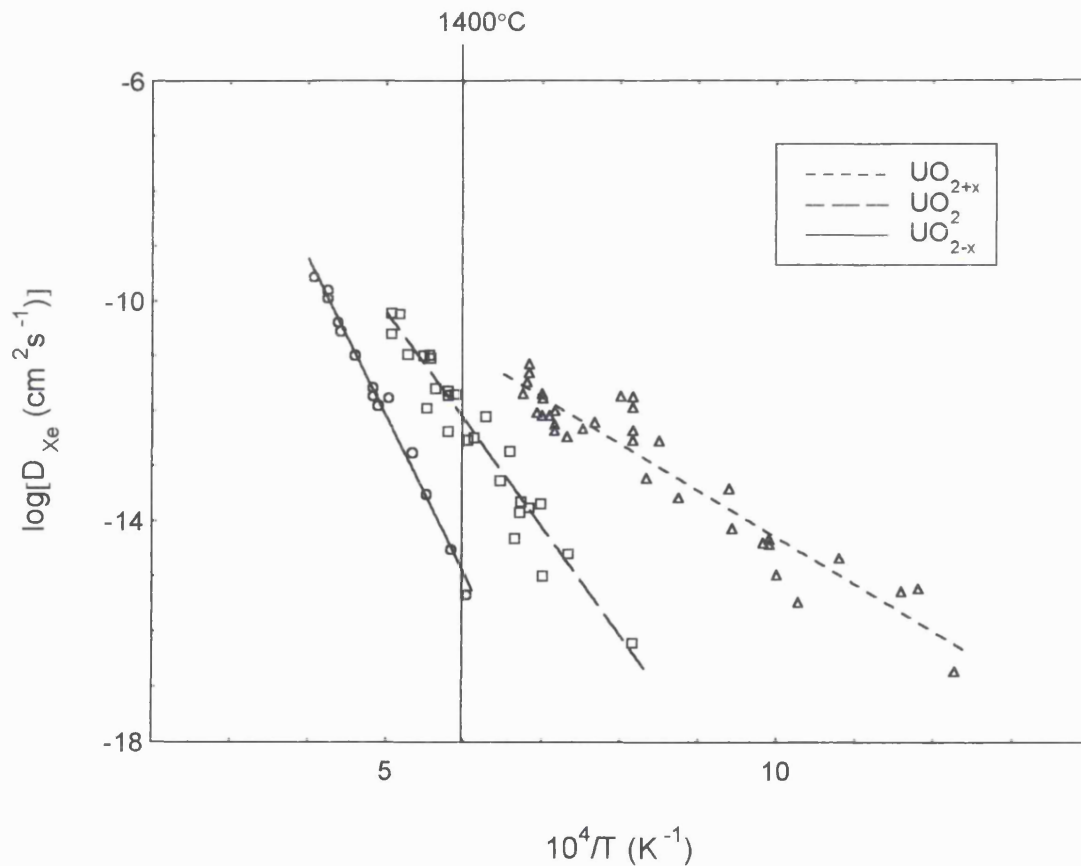


Figure 8. Variation of D_{Xe} with stoichiometry in UO_2 powders, as found by Miekeley and Felix [47]. Note the grouping of the data into the three stoichiometry regions.

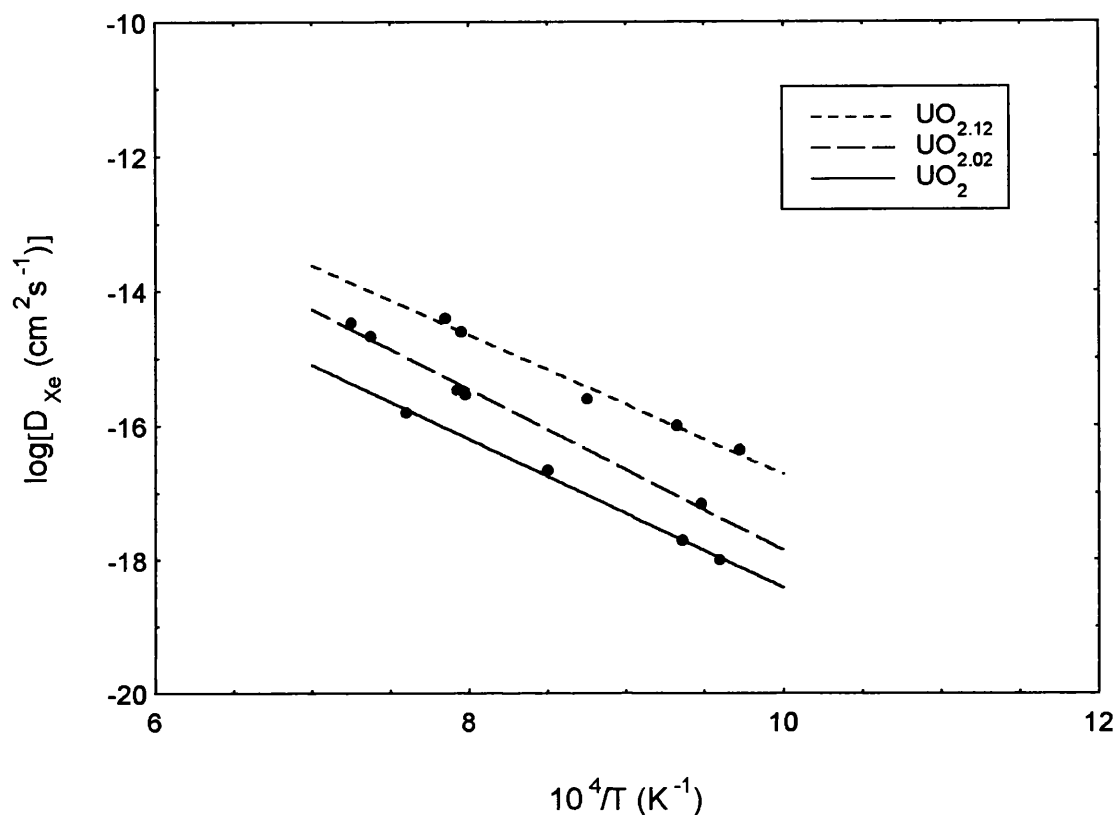


Figure 9. Variation of D_{Xe} with stoichiometry in UO_{2+x} powders, as found by Lindner and Matzke [48]. In contrast to Figure 8 the results suggest that D_{Xe} is dependent on the magnitude of x in UO_{2+x} .

5.3 Computational Procedure

Our starting point in this chapter is the calculation of the formation energies of defects in uranium dioxide. The calculation of such quantities is based on the computational methods discussed in Chapter 3. An integral factor in applying this approach is the need to derive a reliable description of the interactions between ions of the Xe- UO_2 system. In the past, workers have employed several different models for the interionic potentials used in describing these interactions. In his original calculations Catlow [44] employed a

mixture of empirical fitting and Hartree-Fock calculation to derive the interactions between host ions. The interactions between a host and Xe atom, on the other hand, were described using the electron gas method of Gordon and Kim [16,17]. Later, Jackson and Catlow [51] carried out further calculations. In these, they retained the host ion potentials of Catlow's earlier work but used a new set of Xe-host potentials. These were again derived from the method of Gordon and Kim but this time used electron densities which had been refined through the inclusion of relativistic effects. Despite the successes enjoyed by these authors it was recognised that an alternative approach, which avoided the mixing of computed and empirical potentials in the same simulation, was desirable [52]. More recently, Grimes and Catlow [10] achieved this by deriving a set of potentials for both the host and Xe atom interactions solely through use of the Gordon and Kim method. These potentials did, however, result in a poorer calculation of known crystal properties and a rather high value for the formation energy of an oxygen Frenkel defect, the importance of which will be discussed further below. In view of these points, it was decided, in the present work, to attempt to derive a compromise set of interionic potentials.

To ensure that a calculation of intrinsic defect energies would give reasonable results, for the host ion interactions it was decided to employ the set of empirical potentials developed for the UO_2 system by Jackson and co-workers [42]. A set of potentials for the Xe interactions was then derived in a way aiming at some compatibility with these. The approach used was the "empiricizing" method outlined in Chapter 3. Van der Waals type forces were calculated separately using the formula of Slater and Kirkwood (see equation 40) as described by Fowler and co-workers [20]. The short range part of the interaction potentials are given in Table 2. For the long range Coulombic interactions full formal ion charges are assumed.

Interaction	A (eV)	r (Å)	C_6 (eVÅ ⁶)	range (Å)
O-O	11272.6	0.1363	-	$r < 1.2$
O-O	-	-	134.0	$r > 2.6$
U-O	1518.92	0.38208	65.41	$r > 0$
Xe-O	210.8	0.4985	100.02	$r > 0$
Xe-U	4398.0	0.3805	77.73	$r > 0$

Table 2. Parameters for the short range potentials of the Xe-UO₂ system. The potentials are of the Buckingham form $A\exp(-r/\rho) - C_6/r^6$. For the O-O interactions in the ranges $1.2 < r < 2.1$ Å and $2.1 < r < 2.6$ Å, 5th and 3rd order polynomials respectively were used to interpolated between the two ranges quoted in the table. O-O and U-O interaction were those derived by Jackson and co-workers [42], although in their original work 5th and 7th order polynomials were used for the interpolation within the O-O interaction. In the simulations reported here, all short range potentials were cut off for $r > 8.475$ Å.

Ionic polarizabilities were handled via the shell model of Dick and Overhauser discussed in Chapter 3. The shell model parameters used in the present work are given in Table 3.

Defect formation energies, calculated using the above approach, can be used in conjunction with the simple statistical mechanical approach outlined in Chapter 2 to gain information on defect concentrations (in our case, the concentration of Xe at a particular site in UO_{2+x}). The assumptions used in the approach are rather idealised (particularly when considering high concentrations of defects), but we would like to show that the method can still be applied successfully in the case of Xe atoms in UO₂.

Ion	Y (e)	k (eVÅ ⁻²)
O	-4.4	296.2
U	6.54	94.24
Xe	-7.901	222.06

Table 3. Shell model parameters for U, O and Xe. Here Y is the shell charge and k is the coupling force constant. Values are taken from refs. [42] and [20].

It is important to note that equation 4 contains no terms corresponding to the formation of gas bubbles. Whilst there is certainly no reason why such terms could not be included, this omission is, in our case, intentional. In a calculation of the thermodynamic equilibrium of our model closed system, Xe bubble formation is inevitable. The kinetics of this process are, however, not accessible using the simple equilibrium approach outlined in Chapter 2. As we wish to investigate the realm where, in the experimental open system, bubble formation does not have the time to occur, we must ensure that bubble formation is not a possible path in the equilibrium calculation. Our calculations thus refer to that proportion of the total Xe concentration which is dispersed through the lattice and not trapped in bubbles. Under experimental conditions at low gas concentrations this proportion will be large. As already mentioned, it is believed that this realm of low levels of bubble formation persists through the transition shown in the experimental data of Figure 7.

Defect	Energy (eV)
Xe interstitial	18.67
Xe at O vacancy	32.23
Xe at U vacancy	86.05
Xe at divacancy	99.26
Xe at trivacancy	113.77
Xe at tetravacancy	191.12

Table 4. Basic defect energies of Xe in UO_2 calculated via computer simulation.

5.4 Results and Discussion

The basic defect energies derived from our computer simulations are presented in Table 4. The results are consistent with those previously reported by Catlow [44] and Ball and Grimes [50]. If the same analysis that was used by these authors is applied, then isolated Xe atoms are found to be positioned at trivacancies in UO_{2-x} and at uranium vacancies in UO_{2+x} . In UO_2 , the trivacancy site is found to be slightly more favourable than the divacancy. The interesting point arises however, when we consider the predicted concentrations of Xe at each particular site. By introducing stoichiometry and Xe concentration via the constraint equations 6, we can investigate the effect of continually varying these parameters upon the behaviour of Xe in our model Xe- UO_2 system.

In Figure 10 we plot the proportion of Xe occupying divacancy sites against the Xe concentration at 1400°C in stoichiometric UO₂ (under these conditions almost all the remaining Xe is calculated to be in trivacancies). It will be noticed that above a certain Xe concentration there is a sharp decrease in the amount of Xe in divacancies; virtually all the Xe atoms are then found at trivacancy sites. Thus, if we consider the case of increasing Xe concentration, we can think of this transition as being associated with the equilibrium,



written in Kröger-Vink notation. This equilibrium will, however, be influenced by the oxygen Frenkel equilibrium through the occurrence of the oxygen vacancy, $\text{V}_{\text{O}}^{\bullet\bullet}$, in the equation. The behaviour demonstrated in Figure 10 is thus governed by the values of two equilibrium constants. Clearly then, computer simulations which do not provide a realistic value for the oxygen Frenkel formation energy will be unlikely to position this transition in the correct region of Xe concentration. It is for this reason that we have based our calculations on the reliable empirical potentials of Jackson and co-workers [42].

When Figure 10 is compared to Figure 7 it will be seen that the drop in D_{Xe} observed in the data of MacEwan and Stevens upon increasing the Xe concentration, would appear to coincide with the *calculated* drop in the proportion of Xe occupying divacancy sites. It should be remarked that in Figure 10 we have given the case for an idealised absolute stoichiometric composition. For small oxygen excesses, less than those that can be resolved by experiment, divacancies may actually form the majority Xe site in the low concentration region of Figure 10. This can be seen from Figure 11 where the calculated sites for single atoms of Xe are plotted as a function of O/U ratio.

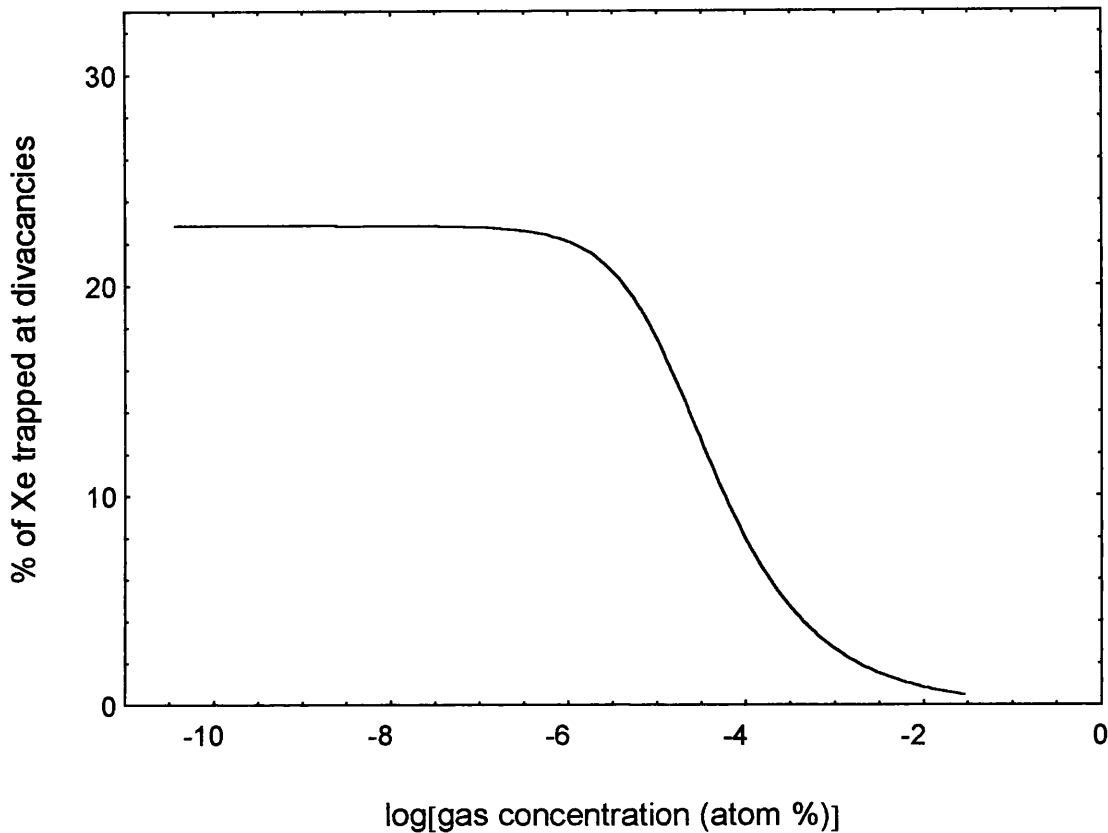


Figure 10. Calculated proportion of Xe at divacancy sites in stoichiometric UO_2 as a function of Xe concentration at 1400°C . The remaining proportion of the Xe is calculated to be at trivacancy sites.

If then, in stoichiometric UO_2 , there is a change in site of single Xe atoms upon increasing the Xe concentration, the question arises as to what effect this will have on the diffusion coefficient D_{Xe} . Strangely enough, some indirect help can be obtained from the work of Miekeley and Felix, where it was the stoichiometry that was the main variable. In common with previous workers (see for example Catlow's paper [44]) our calculations show that the location of Xe atoms at the low gas concentrations used in the Miekeley and Felix experiments, is extremely sensitive to any departures from stoichiometric composition (see Figure 11). In particular, almost any degree of hypo-stoichiometry (oxygen deficiency) will result in virtually all the Xe atoms

occupying trivacancy sites. Thus, the calculated change in the Xe site upon going from UO_2 to UO_{2-x} at low gas concentrations is identical with the change predicted in stoichiometric UO_2 when the gas concentration is increased; that is, in both cases a transition from conditions where both di- and trivacancies are important Xe sites, to those where Xe atoms are located in trivacancies only (cf. Figures 11 and 10).

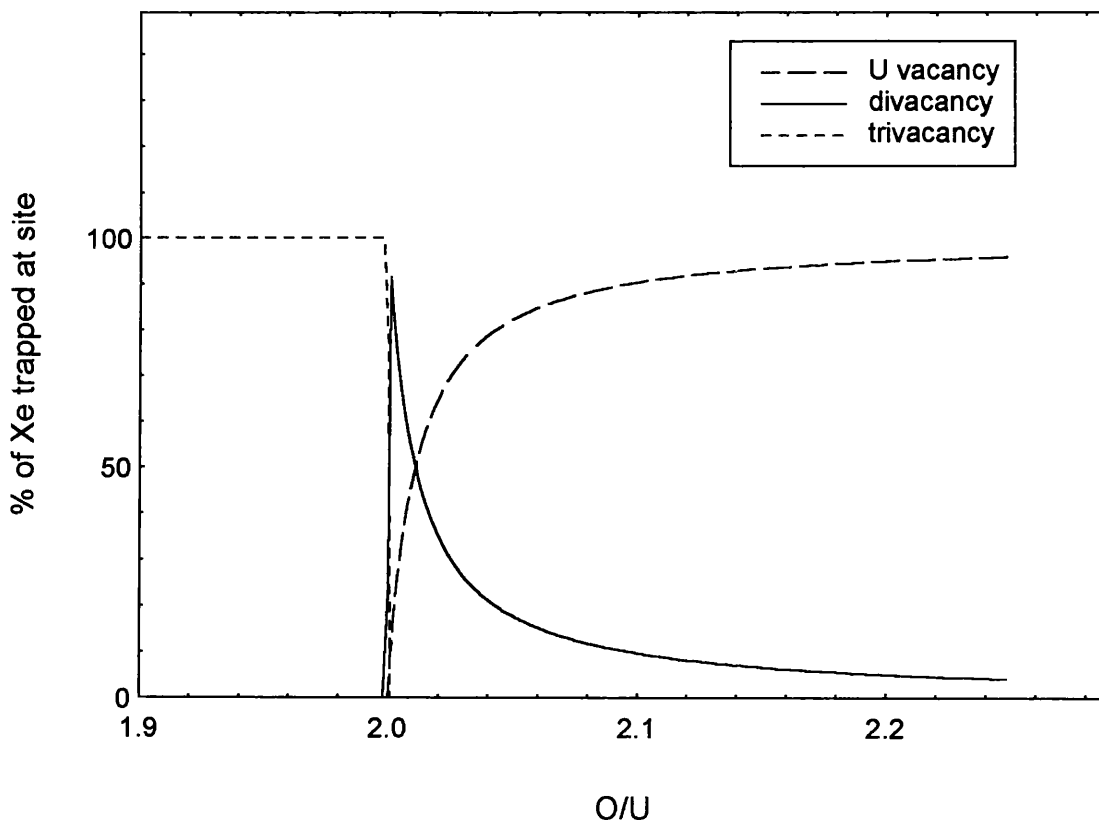


Figure 11. Calculated proportion of Xe at U, di-, and trivacancy sites in $\text{UO}_{2\pm x}$ as a function of O/U ratio. Xe concentration = 10^{-7} atom% and $T=1400^\circ\text{C}$.

Atomic diffusion however, is not only a function of atom location but also of the migration mechanism. It has been suggested that in UO_{2+x} , a uranium vacancy assisted migration mechanism might be at work [44,50] and this may be evidenced in the results of Lindner and Matzke shown in Figure 9 (because through the system constraints, increasing x has the effect of increasing the U vacancy concentration). Nevertheless, whilst it cannot be ruled out that an enhancement in the efficiency of an existing migration mechanism is responsible for the difference between D_{Xe} in UO_2 and UO_{2-x} , the data of Miekeley and Felix might well be indicating the effect of a change in Xe location between these stoichiometries. Support for this point of view comes from the work of Matzke [49] who suggested that, on the basis of diffusion experiments on UO_2 doped with aliovalent impurities, vacancy assisted mechanisms may be unimportant in UO_2 . Hence we might assume that on going from UO_2 to UO_{2-x} , any change in the atomic diffusion will mainly originate from a change in the site of single atoms of Xe. From Figure 8, it can be seen that a transition from a region of stoichiometric composition to one of hypo-stoichiometry results in a smaller value for D_{Xe} . Thus whilst the reasoning is by no means totally compelling, the implication is that the transition in the Xe location seen in Figure 10 will be reflected in a change of D_{Xe} in a manner similar to that seen in Figure 7, that is, a reduction in D_{Xe} with increasing gas concentration.

The above comparison of our calculations on Xe sites with experimental diffusion data (that is data concerning both site and mobility) is intended to add an, as yet, neglected aspect to the discussion of Xe diffusion in UO_2 . The predicted importance of di- and trivacancies as sites for Xe in UO_2 is not in disagreement with the previous experimental results of Matzke and Davies [40], whose channelling investigations of the behaviour of the heavier rare gas Rn in stoichiometric UO_2 suggest that Xe will not occupy single U vacancies. This work did not, however, rule out the occupation of di- or trivacancy sites.

There are some final comments which are necessary concerning the results of this chapter. Implicit in the treatment above is the view that, whatever the actual migration

mechanism, Xe atoms in divacancies are more mobile than those in trivacancies. It should be borne in mind that migration mechanisms of Xe in uranium dioxide are still not well understood, and this assumption, although we have given a reason in its support, is not investigated further here. We have also divorced our model system from a more realistic case where gas atoms may become immobilised through interactions with pre-existing porosity and radiation damage. Such factors are discussed in the work of MacEwan and co-workers and were suggested there as a cause for the transition seen in Figure 7 [46,53]. It is suggested that the effect of the change in site of single Xe atoms calculated in this chapter acts in addition to the factors discussed by these authors.

5.5 Summary

In this chapter we have discussed the effect of increasing Xe concentration upon the site of single atoms of Xe in a model Xe-UO₂ system. At low Xe concentrations, calculations demonstrate the importance of divacancy sites. Although these may not necessarily constitute the majority site (more Xe is perhaps to be found in trivacancies) it is suggested that divacancies are an important factor in the diffusion of Xe atoms in stoichiometric UO₂. As Xe concentration is increased the importance of divacancy sites is diminished until most of the single atoms of Xe are found at trivacancies; the transition is fairly sharp and is calculated to occur at a Xe concentration of about 10⁻⁶ atom %. Although the actual migration mechanisms of Xe atom diffusion are beyond the intended scope of this study, experimental data gathered at different stoichiometries are found to suggest that a reduction in the proportion of Xe at divacancies, would result in a corresponding reduction of D_{Xe}. As the transition mentioned above is calculated to coincide with the observed decrease in D_{Xe} seen in the data of MacEwan and Stevens, it is suggested that in addition to being induced by radiation damage as these authors have suggested, the decrease in D_{Xe} may also contain a contribution originating from a change in the site of single Xe atoms. Although the results presented in this chapter in no way

deny the importance of bubble formation and radiation damage on the behaviour of fission gases in nuclear fuels, they add an important aspect to the atomistic picture of Xe in UO_2 which should not be overlooked.

Many codes in use today for the modelling of reactor fuel materials take as part of their basic input a simple Arrhenius relation for D_{Xe} based on the available experimental data. Clearly there are many factors which can influence Xe diffusion and there have accordingly been attempts to include these in more sophisticated relations for D_{Xe} . In this chapter we have discussed one of these factors in detail in an attempt to rationalise the reason for its influence.

6 Mo

6.1 Introduction.

Of all the fission products Mo occupies a very special place as regards the chemistry of the reactor fuel. Its elemental yield is almost on a par with that of Xe [36] and so its abundance alone would warrant a detailed study of its behaviour. However, much more important than this is the major influence it has on the fuel oxygen potential.

There are two principal reasons for the importance of the fuel oxygen potential. Firstly, it controls the chemical nature of many of the fission products and thus has a knock-on effect regarding their physical behaviour and their role in such important factors as fuel swelling and release rates. Secondly, an uncontrolled increase in the oxygen potential may lead to corrosion of the fuel cladding with serious implications for reactor safety and operation. As the oxygen potential is clearly such a major parameter, any factor which exerts some control over it will be seen to be of great importance.

In Figure 12 we have reproduced from Cordfunke and Konings [54] a graph showing the relationship between the oxygen potential and the oxygen/uranium ratio in UO_{2+x} . We see that close to the stoichiometric composition, the oxygen potential is extremely sensitive to the O/U ratio. If we consider the Mo/MoO₂ couple,



we can draw on Figure 12 a line representing $\Delta G_F(MoO_2)$, the free energy of formation of MoO₂. From the law of mass action, we can think of the transition between Mo dominance and MoO₂ dominance of this equilibrium as being marked by a partial pressure of O₂ of

$$P_{O_2} = \exp(\Delta G_F(MoO_2) / RT), \quad (47)$$

or equivalently an oxygen potential of,

$$\Delta\bar{G}_{\text{O}_2} = RT \ln P_{\text{O}_2} = \Delta G_{\text{F}}(\text{MoO}_2). \quad (48)$$

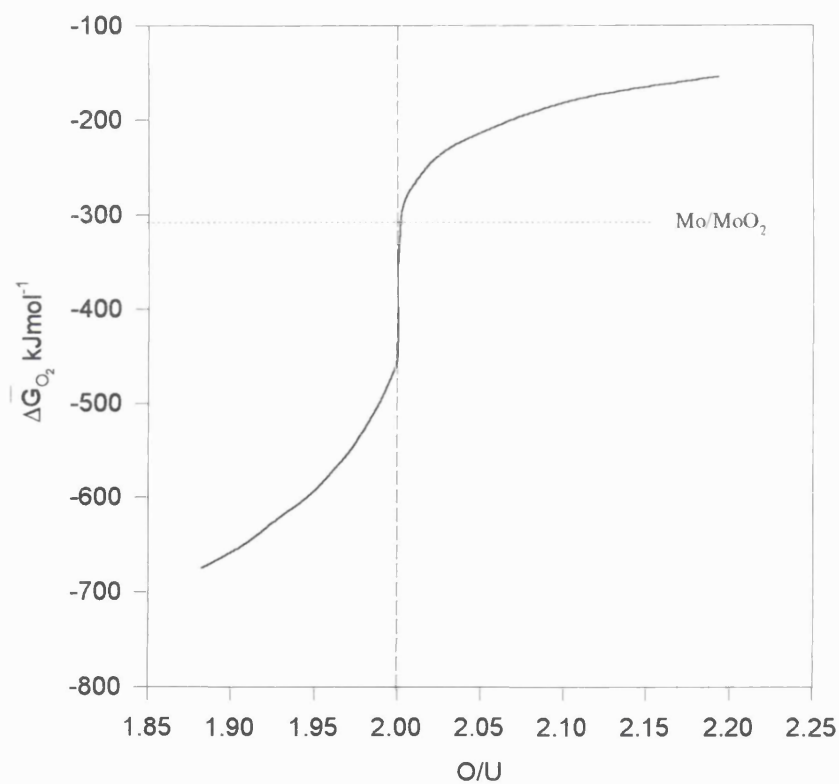


Figure 12. Variation of the oxygen potential of UO_2 with O/U ratio (after Cordfunke and Konings [54]). The horizontal line marks the oxygen potential of the Mo/MoO₂ couple, which is seen to lie very close to that of stoichiometric UO_2 . T=1673 K.

At higher oxygen potentials the equilibrium of the Mo/MoO₂ couple will be displaced towards MoO₂; at lower values Mo metal will predominate. From Figure 12 we can see that the line we have drawn for $\Delta G_F(\text{MoO}_2)$ cuts the graph at an oxygen potential quite close to that occurring in stoichiometric UO₂. The chemical nature of Mo should therefore be a sensitive indicator of fuel stoichiometry and certainly a partitioning of Mo between metallic and oxide phases is observed in reactor fuels⁶ [55]. Given its high yield, it is thus clear that Mo may act as a buffer to the fuel oxygen potential and recent measurements of the oxygen potential in high burn-up fuel suggests this is indeed the case [56].

In this chapter we give results of computer simulations of single Mo atoms in UO_{2+x} but before doing this we shall first discuss what is known, from the experimental perspective, of the behaviour of Mo in urania.

6.2 Experimental Knowledge.

Examination of irradiated reactor fuels using electron and optical microscopy and electron microprobe analysis reveals the presence of two major classes of solid fission product precipitates. These are the ‘grey phase’ precipitates, typified by the perovskite structured (Ba,Sr,Cs)(U,Pu,RE,Zr,Mo)O₃ and the ‘white inclusions’ consisting of alloys of noble metals [55]. These latter, which we shall concentrate on here, are composed almost exclusively of the metals Mo, Tc, Ru, Rh and Pd and are hence often given the name “five metal particles”. The metallic precipitates occur both intra-granularly and on grain boundaries and are often seen to be intimately associated with bubbles of fission gases (Xe and Kr) to the extent that the precipitates are frequently found to be located

⁶ Measurement of this partitioning by electron microprobe analysis has been suggested as a means by which the local O/M ratio in (U,Pu)O₂ may be determined (see Olander for discussion [58]). However, Giacchetti and Sari [59] argue that the method is unsound due to the low solubility of Mo and the possibility of mistaking small metallic precipitates as Mo in solution.

within the gas bubbles themselves [57]. This close association of metallic precipitate and fission gas bubble is suggestive of a co-precipitation phenomena.

The grain boundary precipitates are in general much larger than those found within the grains and they thus provide the bulk of the information from optical and X-ray diffraction data. Under normal reactor operating conditions the size of the intra-granular precipitates rarely exceeds more than some 10 nm possibly due to re-resolution into the lattice with fission spikes [57]. If the fuel undergoes an increased power transient in the reactor however, sizes of the order of 100-1000 nm may be obtained. Such particles provide most of the detailed knowledge on the in-grain precipitates.

The five metal particles commonly exhibit the hexagonal ϵ -Ru(Mo, Tc, Rh, Pd) phase, although less commonly a two phase nature may be observed [54]. A quasi-ternary phase diagram of the Mo-(Tc,Ru)-(Ru,Pd) system and its relationship to reactor fuels may be found in Kleykamp [36]. In a particular precipitate, the actual proportion occurring of each of the 5 elements appears to be fairly random [57], although Kleykamp has suggested that the compositions can be related to the local oxygen potential (burn-up and stoichiometry) and temperature [36]. An interesting observation from EDAX (Energy Dispersive X-ray Analysis) work is that the rim of these precipitates are often found to be depleted in Mo and enriched in Pd [57]. Whilst the Mo depletion may find an explanation in terms of the increasing oxygen potential with burn-up (and hence time) the Pd enrichment is more puzzling (see Chapter 7 for a further comment regarding this). Results such as these do not however seem to have appeared in the open literature and hence we shall discuss them no further in this chapter.

In the past, it has often be thought that at high enough oxygen potentials MoO_2 may exist in solid solution with the UO_2 lattice (see for example [58]). The experimental investigations of Giacchetti and Sari however, indicated a very low solubility for Mo in UO_2 [59]. In investigations on trace irradiated UO_2 samples, Prussin and co-workers [60] found release rates for Mo to be much lower than those of Xe suggesting that a

simple model of Mo migration as an insoluble neutral atom may not be appropriate. Mo release rates were, however, found to be higher than those for the soluble fission products, such as Nd and La, for which no release was observed. The case for Mo should be contrasted to those of Ru and Tc which were found to have similar release rate to Xe [60] (we shall be discussing the behaviour of Ru, Rh and Pd in greater depth in the next chapter). Mo thus appears to demonstrate behaviour lying between that of the soluble and insoluble fission products.

At low oxygen potentials, the general behaviour of Mo seems to be fairly clear; at high enough concentrations it precipitates out together with the other metals of the five metal particles. The ratio of Mo in these particles to that of Mo dispersed in the lattice is not known, although the work of Giacchetti and Sari [59] would tend to suggest that the majority of the Mo precipitates out. However, the low release observed by Prussin and co-workers may suggest a measurable but low atomic mobility and hence the presence of a significant population of isolated atoms or ions of Mo in the lattice at any one time (the experiments of Prussin and co-workers were carried out on trace irradiated samples and precipitation was not thought to be a major factor). As the oxygen potential is increased, the picture is further complicated due to the partitioning of Mo between oxide and metallic precipitates as well as the continued uncertainty of the role and nature of any Mo that may be dispersed throughout the lattice.

6.3 Computer Simulation of Mo in Urania

As was the case with Xe there are three parameters of principle importance employed in analysing results from our simulations; fission product concentration, fuel stoichiometry and temperature. As explained earlier the energy terms calculated in our simulations do not include any temperature dependence excepting that they are based on potentials for the UO_2 lattice designed to give a good value for the lattice parameter over a broad range of temperatures (see [42]). As already mentioned, both the temperature variation

of defect energies, as well as the change in vibrational entropy of the lattice brought about by the creation of a defect, can in principle be calculated but we have not done this in the present work. In view of this we do not explicitly investigate the effect of temperature variation on Mo behaviour although there are undoubtedly some interesting temperature dependency effects to be found for some of the fission products⁷. In these calculations we thus fix the temperature used in solving equations 6 and 7 at a value of relevance to much of the experimental literature and investigate changes in Mo behaviour brought about by stoichiometry and concentration variation alone.

Again we employ the potentials of Jackson and co-workers [42] for the UO_2 lattice and derive “empiricised” potentials for the interactions between Mo and host ions (U^{4+} and O^{2-}). Interactions for Mo with the charge states 0 through to 6+ were calculated. The derived potentials, which were all fitted to the Buckingham form, will be found in Table 5.

Examination of Table 5 reveals a pattern of decreasing ρ and increasing A with increasing Mo charge. This pattern breaks down, however, in the case of interactions involving neutral Mo atoms. The origin of this deviation lies in the method used to calculate the Mo electron densities. As discussed in Chapter 3, there were two methods available to calculate these densities; to expand tabulated wave functions or to calculate densities numerically (in our case using the HERSKILL code of Harding and Harker [18]). As tabulated wave functions were unavailable for most of the Mo ions considered, the latter method was employed in deriving the electron densities for the ions Mo^{1+} through to Mo^{6+} . In the case of neutral Mo however, all attempts to calculate densities using HERSKILL failed to converge. We were thus forced, in this one case, to employ the expansion of tabulated wave functions scheme. Clearly, electron densities calculated

⁷ Although some temperature dependence is included through the approximation used for the configurational entropy this clearly does not account for all the temperature effects.

Interaction	A (eV)	ρ (Å)	C_6 (eV Å ⁶)
Mo-O ²⁻	370.3	0.4417	172.09
Mo ¹⁺ -O ²⁻	345.3	0.4463	65.24
Mo ²⁺ -O ²⁻	508.3	0.4367	43.08
Mo ³⁺ -O ²⁻	718.3	0.4102	28.53
Mo ⁴⁺ -O ²⁻	914.9	0.3901	19.53
Mo ⁵⁺ -O ²⁻	1075.0	0.3764	14.82
Mo ⁶⁺ -O ²⁻	1191.0	0.3675	10.13
Mo-U ⁴⁺	4055.0	0.3614	127.78
Mo ¹⁺ -U ⁴⁺	3814.0	0.3672	51.76
Mo ²⁺ -U ⁴⁺	5324.0	0.3264	35.12
Mo ³⁺ -U ⁴⁺	6503.0	0.3038	23.86
Mo ⁴⁺ -U ⁴⁺	7472.0	0.2889	16.68
Mo ⁵⁺ -U ⁴⁺	8366.0	0.2776	12.84
Mo ⁶⁺ -U ⁴⁺	9279.0	0.2682	8.93

Table 5. Short range potentials for Mo interactions. The Buckingham form $A\exp(-r/\rho)-C_6/r^6$ has been used.

using the two different approaches are not totally equivalent (though we would naturally hope that they would not disagree too drastically) and this has been reflected in the derived potentials. We have thus lost some consistency between the Mo interactions. However, the final calculations indicate that this is of no critical importance as far as the qualitative results of the simulations are concerned.

The electron gas scheme cannot give information concerning the long range dispersive interactions (incorporated as the C_6 term in the Buckingham potential) and in this case we have again made use of the Slater-Kirkwood formula discussed in Chapter 3. To achieve this, estimates of the ionic polarizabilities were required. Polarizabilities (although unfortunately not in-crystal polarizabilities) have been published for Mo and Mo^{6+} [61,62]. Values for the remaining charge states could not be found in the literature. For the ions Mo^{1+} to Mo^{5+} we thus interpolated between the two known extremes on the basis of the assumption that the polarizabilities scaled with the ionic volume. The resulting polarizabilities are given in Table 6. These estimated polarizabilities were used in deriving both the C_6 values shown in Table 5 and shell model parameters which are included in Table 6.

In deriving the C_6 parameter using the Slater-Kirkwood formula (equation 40) in addition to the polarizability itself, we require an estimate of the number of electrons significantly contributing to the polarizability. Fowler and co-workers [20] suggest the use of the value derived for the isoelectronic noble gas atom. For Mo^{6+} this would be about 7.3, as derived in [20] for Kr. For the remaining charge states there is no simple prescription to derive them. We thus fix the electron numbers for all Mo ions at 7. In the Slater-Kirkwood formula however, it is the effect of the polarizability which is most important and the crudity of this estimate for the electron numbers should not have a great effect on the final potentials. We also use this value for the electron number in the shell model, with spring constants being obtained from equation 43 together with the polarizabilities derived above.

Ionization potentials, used in the model for charge transfer effects, have been taken from the literature and are tabulated in Table 7. Ionization potentials for Ru, Rh and Pd have also been included in this table and will be used in the following chapter.

	α (\AA^3)	Y	K ($\text{eV}\text{\AA}^{-2}$)
Mo	9.0	7.0	78.40
Mo ¹⁺	2.4	7.0	294.0
Mo ²⁺	1.42	7.0	496.89
Mo ³⁺	0.86	7.0	820.45
Mo ⁴⁺	0.55	7.0	1282.89
Mo ⁵⁺	0.40	7.0	1763.98
Mo ⁶⁺	0.26	7.0	2713.81

Table 6. Polarizability data for Mo. The polarizabilities α for Mo and Mo⁶⁺ were obtained from [61] and [62]. The remaining α values were interpolated between these two extremes on the basis of the assumption that α scales with ionic volume (spherical ions were assumed and ionic radii were taken from [62]). The electron numbers Y, which are used for both the shell model and Slater-Kirkwood calculation of C_6 parameters, are unknown and have been fixed at 7.0. See text for a further discussion.

	U	Mo	Ru	Rh	Pd
1	6.03	7.10	7.37	7.46	8.34
2	11.84	16.15	16.76	18.07	19.43
3	19.24	27.16	28.47	31.06	32.93
4	31.86	46.40	-	-	-
5	46.57	61.25	-	-	-
6	61.70	68.00	-	-	-

Table 7. Ionization potentials (in eV) used in this work. Sources are [62] and [63].

6.4 Results

The basic defect energies calculated using the CASCADE code are reported in Table 8. These are equivalent to the energies denoted by g^* in equation 9. For two of the results⁸, convergence difficulties were initially experienced but these were removed if the calculation was repeated with no shell on the relevant Mo ion (the shell model still being employed for the host ions). By calculating and comparing defect energies of several Mo defects with and without shells on the Mo, it was confirmed that the act of removing the shell from the Mo ions would have only a small effect on calculated defect energies (probably of the order of a few tenths of an eV for the problem configurations) and thus removing the Mo shells in the two problem cases should have little influence on the final

⁸ These were the calculations concerning neutral Mo in a trivacancy site and Mo^{1+} in an oxygen vacancy.

results. Difficulties also occurred in six other calculations for which a solution could not be obtained. We were fortunate however, in that these six calculations related to quite unimportant defect configurations⁹.

By fixing the system temperature at 1673 K, using the results of Table 8 the defect equilibrium, under variations in fuel stoichiometry and the concentration of single atoms of Mo, has been calculated. This corresponds to investigating the nature of the Mo dispersed through the UO_2 lattice as isolated single atoms.

In sub-stoichiometric UO_{2-x} the picture is fairly clear. Neutral Mo atoms at trivacancy sites are by far the most energetically preferred defect configurations for single Mo atoms at all degrees of sub-stoichiometry and Mo concentrations. We thus plot in Figure 13 the variation in the proportion of all the Mo^{10} (present as single isolated atoms) located in trivacancies, over the whole range in stoichiometry and concentration being considered. We find that in addition to its dominance as a Mo site in UO_{2-x} (where it accommodates almost 100% of the Mo) the trivacancy would also appear to play a role in UO_{2+x} when the Mo concentration is particularly high (we shall return to a discussion of this point later).

What is clear from the calculations, is that in stoichiometric UO_2 the importance of the trivacancy is dependent upon the Mo concentration (compare with the results of Chapter 5 on the behaviour of Xe). At low concentrations relatively little Mo should be found in trivacancies (of the order of 5% of the total Mo concentration). At high concentrations however, the proportion of Mo in trivacancies should approach that

⁹ The defect configurations concerned were Mo^{3+} to Mo^{6+} at the oxygen vacancy, and Mo^{5+} at the divacancy and the tetravacancy sites. The unimportance of these configurations will become apparent through examination of the trends observed in our results and the subsequent discussion.

¹⁰ We shall use the term "Mo" to signify the population of single isolated atoms of Mo in all charge states. When considering Mo ions of a specific charge (including neutral Mo atoms) the charge state shall be given explicitly.

calculated for the case of UO_{2-x} . Whenever Mo is present in a trivacancy site it is calculated to be in the neutral charge state.

Defect	Energy (eV)	Defect	Energy (eV)
Mo^0 at V_U	82.66	Mo^0 at divacancy	97.01
Mo^{1+} at V_U	74.80	Mo^{1+} at divacancy	89.82
Mo^{2+} at V_U	58.49	Mo^{2+} at divacancy	74.31
Mo^{3+} at V_U	31.51	Mo^{3+} at divacancy	47.89
Mo^{4+} at V_U	-6.75	Mo^{4+} at divacancy	9.46
Mo^{5+} at V_U	-57.98	Mo^{5+} at divacancy	-
Mo^{6+} at V_U	-122.69	Mo^{6+} at divacancy	-
Mo^0 at V_O	26.61	Mo^0 at trivacancy	112.14
Mo^{1+} at V_O	24.90	Mo^{1+} at trivacancy	105.74
Mo^{2+} at V_O	11.85	Mo^{2+} at trivacancy	91.29
Mo^{3+} at V_O	-	Mo^{3+} at trivacancy	65.53
Mo^{4+} at V_O	-	Mo^{4+} at trivacancy	27.23
Mo^{5+} at V_O	-	Mo^{5+} at trivacancy	-26.64
Mo^{6+} at V_O	-	Mo^{6+} at trivacancy	-98.88
Mo^0 interstitial	11.76	Mo^0 at tetravacancy	188.71
Mo^{1+} interstitial	8.81	Mo^{1+} at tetravacancy	183.06
Mo^{2+} interstitial	-5.70	Mo^{2+} at tetravacancy	169.53
Mo^{3+} interstitial	-31.78	Mo^{3+} at tetravacancy	146.60
Mo^{4+} interstitial	-70.55	Mo^{4+} at tetravacancy	111.47
Mo^{5+} interstitial	-122.66	Mo^{5+} at tetravacancy	-
Mo^{6+} interstitial	-188.52	Mo^{6+} at tetravacancy	-

Table 8. Defect energies for Mo in UO_2 calculated with CASCADE.

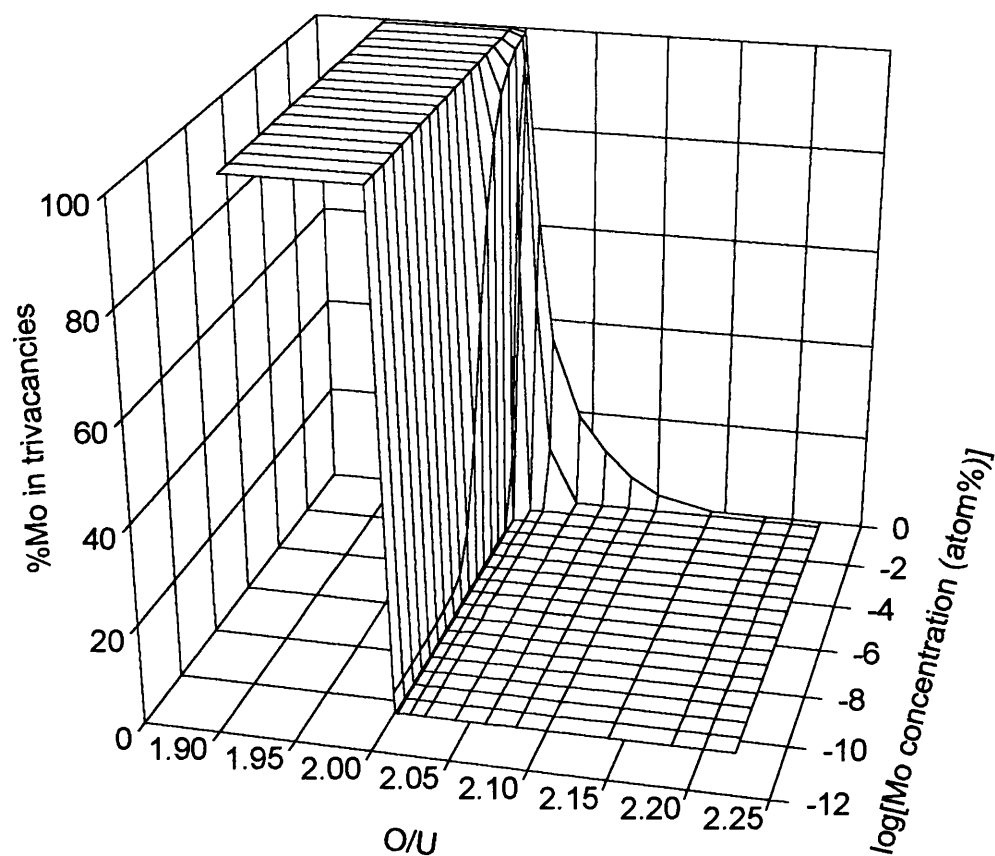


Figure 13. The percentage of isolated Mo atoms occupying trivacancy sites as a function of O/U ratio and Mo concentration. At low and medium concentrations all the Mo is present in trivacancies when urania is hypostoichiometric. Note however, that only in the case of high Mo concentrations is the occupancy of trivacancies a significant factor in hyperstoichiometric urania. Only neutral Mo atoms are calculated to be present in trivacancies.

In Figure 14, we examine in detail the case for stoichiometric UO_2 with changing Mo concentration. We use here the working definition of stoichiometric composition as O/U equal to 2 *exactly*. In practical applications the stoichiometry will only be determinable to within certain bounds and it is important to remember that it may be most appropriate to

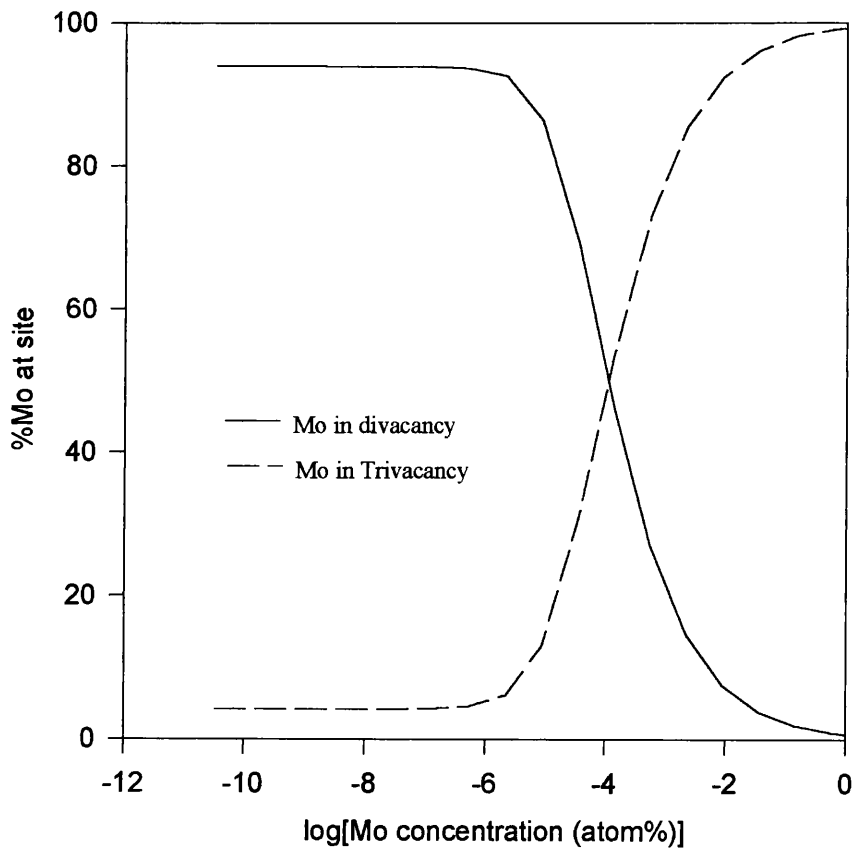


Figure 14. Percentage of isolated Mo in di- and trivacancy sites in stoichiometric UO_2 as a function of Mo concentration.

compare experimental data referring to nominally stoichiometric urania with calculations on a system with O/U only approximately equal to 2. We shall find that at low Mo concentrations this distinction is significant.

Figure 14 plots two lines, one showing the proportion of Mo in trivacancies, the other the proportion in divacancies. It is these two sites which account for almost all the single Mo atoms at exactly stoichiometric composition¹¹. Again Mo at both of these sites is calculated to be in the neutral charge state. It will be seen that for concentrations less than about 10^{-6} atom% over 90% of the Mo is located at divacancy sites. Above this concentration, the trivacancy site gradually regains its importance as the Mo concentration increases up to and into the region where the model of isolated and non-interacting defects very likely breaks down.

When the system moves into the region of hyperstoichiometry it is found that ionization of Mo becomes an important process. The location of the Mo also undergoes a radical change in that the single uranium vacancy becomes the dominant site. We show this in Figure 15 where we have plotted the proportion of Mo in uranium vacancies as a function of the stoichiometry and Mo concentration.

From Figure 15 we can see why it is important to distinguish the idealised exact stoichiometric composition O/U=2 discussed above, from the nominal stoichiometric composition of experimental work. Although at high Mo concentrations a gradual change in the behaviour of Mo is calculated, at low concentrations the change in behaviour on passing from UO_{2-x} through UO_2 to UO_{2+x} is abrupt. We can illustrate this by considering the behaviour of Mo in $\text{UO}_{2.001}$, slightly hyperstoichiometric urania. In this case we find that at low concentrations all the Mo is located in single uranium vacancies¹². Not until the concentration exceeds 10^{-3} atom% does the behaviour begin to

¹¹ Where the divacancy site dominates there is also a small concentration of neutral Mo to be found at uranium vacancies but this population never amounts to more than 1-2% of the total Mo concentration.

¹² With charge states 0 (5%), 1+ (76%), and 2+ (19%).

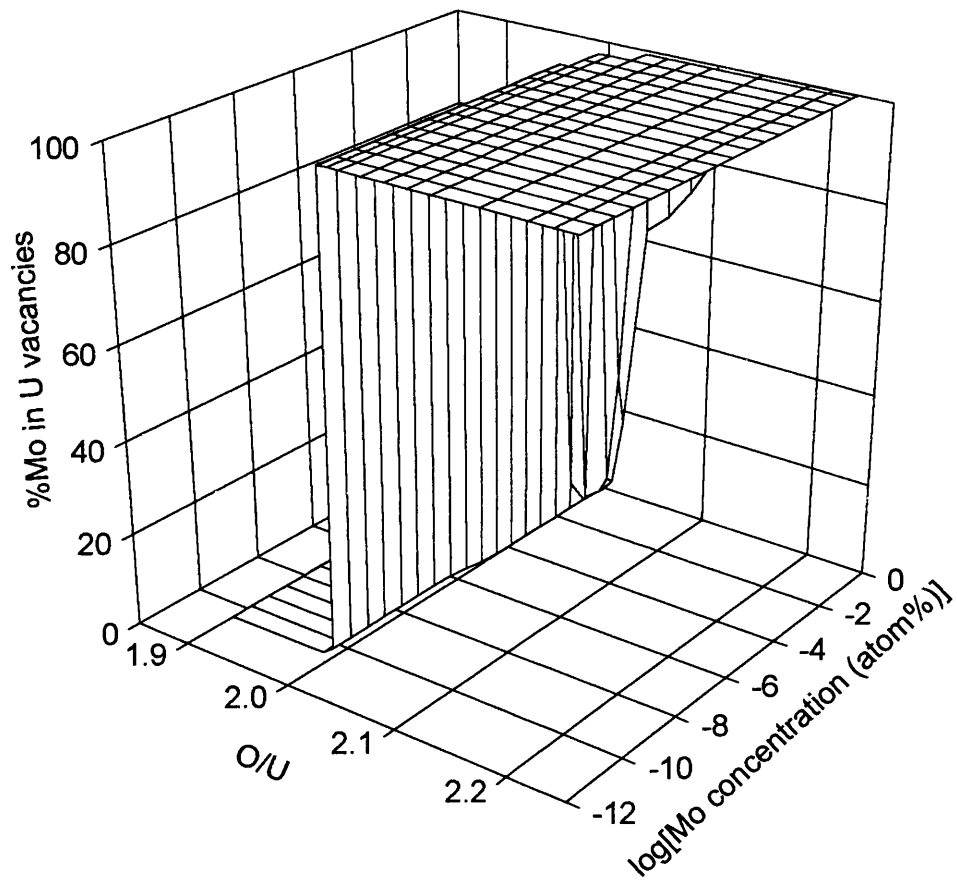
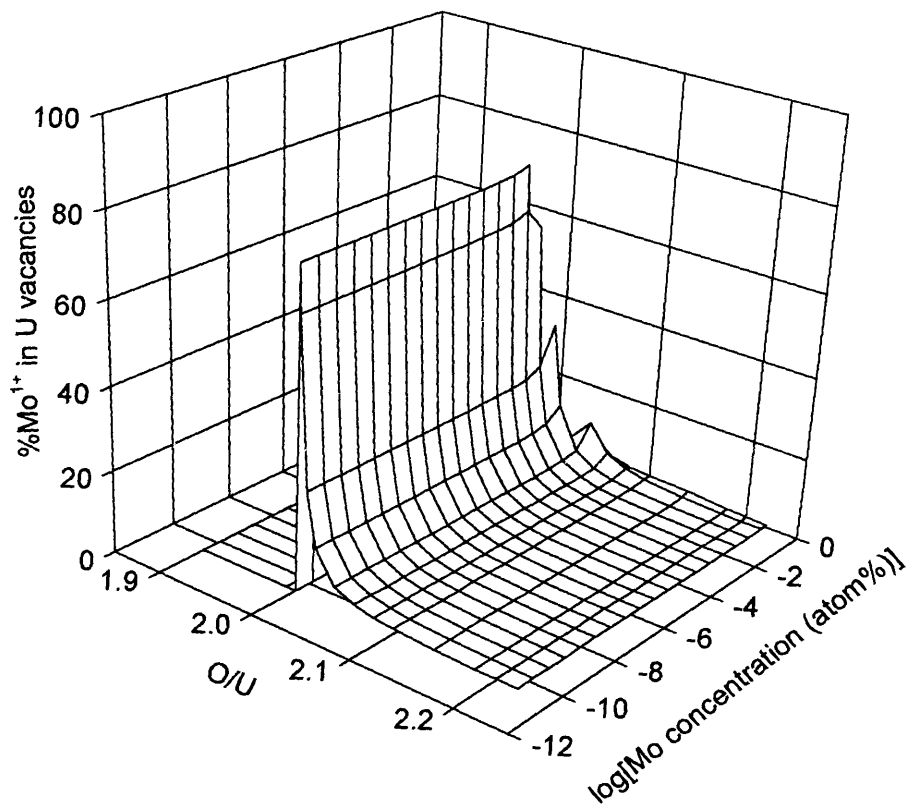


Figure 15. Proportion of Mo (in all charge states) present in single uranium vacancies as a function of stoichiometry and Mo concentration. Note that at high Mo concentrations this proportion is reduced.

resemble that of exactly stoichiometric UO_2 (that is, the region where neutral Mo at di- and trivacancies is prevalent). As already mentioned, the validity of our model of isolated defects becomes, in any case, suspect at such high concentrations. Clearly then, it will be difficult to be sure which of our regions of composition it would be appropriate to compare with the experimental data on nominally stoichiometric urania. Small differences in composition (that is O/U ratio) are seen to lead to quite different predictions for Mo behaviour.

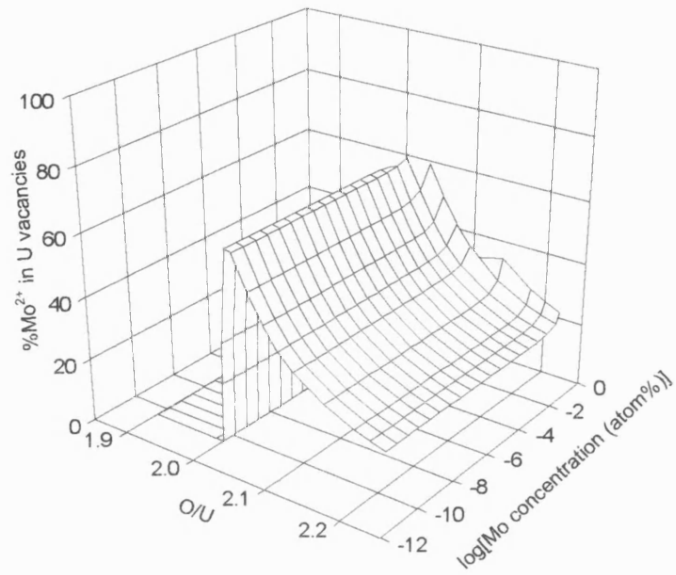
One interesting and perhaps surprising result from our calculations concerns the possible charge states of Mo in urania. In Figure 16 we decompose Figure 15 into the proportions of Mo present in uranium vacancies in the charge states $1+$, $2+$ and $3+$. It is these three states which prevail in UO_{2+x} . As a general rule, increases in hyperstoichiometry lead to increased Mo ionization, which, however, does not extend beyond Mo^{3+} . In $\text{UO}_{2.001}$ for low Mo concentrations, Mo^{1+} is a dominant state. As the degree of hyperstoichiometry is increased it is Mo^{2+} and finally Mo^{3+} which prevail. Up to quite high Mo concentrations in $\text{UO}_{2.2}$ for example, over 80% of the isolated Mo is present as Mo^{3+} in uranium vacancies. What is not calculated to occur in urania however, is any further ionization to Mo^{4+} or higher charge states. In view of the fact that it is often assumed that isolated Mo may be present as Mo^{4+} substituting at uranium vacancies (see for example [58]) the calculated absence of Mo^{4+} is quiet unexpected¹³. We shall defer for a moment a discussion of the reasons behind this result.

¹³ Although we discuss here results from only one set of simulations, we note that a preliminary set of calculations of ours, based on the electron gas UO_2 potentials of Grimes and Catlow [10], also showed no tendency for the Mo^{4+} ion to form. The results from that study were in general agreement with those reported here (based on the potentials of Jackson and co-workers) but are not given here in detail, as the present calculations are thought to be more reliable due to the reasons outlined in Chapter 5.

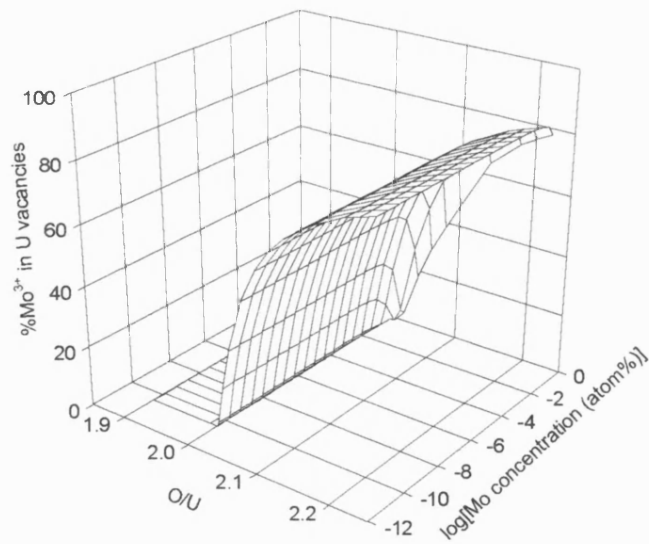


a)

Figure 16. Charge states of Mo in uranium vacancies. a) Proportion of Mo¹⁺ in single uranium vacancies. Figure continued overleaf.



b)



c)

Figure 16 continued. b) Proportion of Mo^{2+} in single uranium vacancies. c) Proportion of Mo^{3+} .

6.5 Further Analysis and Discussion

Having stated the basic results of our calculations of the behaviour of isolated atoms of Mo in urania, let us now look in detail at some of the mechanistic implications. Firstly we can note a basic similarity in the behaviour of Mo and Xe as far as their lattice locations are concerned. In UO_{2-x} it is the trivacancy site that is most important, in UO_2 it is a mixture of divacancy and trivacancy, and finally in UO_{2+x} the uranium vacancy dominates.

In UO_{2-x} neither the oxygen vacancy nor the interstitial site are calculated to be favourable locations for Mo. Although both sites are readily available, the calculated defect energies do not favour these sites above the neutral trivacancy (which must however be formed through the Schottky process):



The last of these two processes, where the accommodation of Mo at pre-existing oxygen vacancies competes with accommodation at trivacancy sites, is almost viable but is prevented through Mo-U interactions¹⁴. Within the bounds of the approximations used in the calculations however, it cannot be ruled out that the oxygen vacancy has some role to play as a site for Mo in UO_{2-x} .

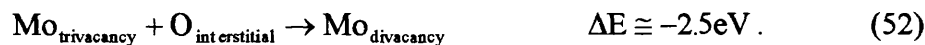
The oxygen Frenkel equilibrium governs the relative concentrations (with respect to one UO_2 formula unit) of oxygen vacancies and interstitials through the equation,

¹⁴ More correctly, this effect is the sum of influences from many origins but the point is being made that if Mo-U interactions are not included in the simulation then the oxygen vacancy becomes the preferred site for Mo in UO_{2-x} . For ionised Mo, Mo-U interactions account for very little of the total defect energy but this is not true in the case of neutral Mo.

$$[O_{\text{vacancies}}][O_{\text{interstitials}}] = 2 \exp\left(\frac{-\Delta G_f}{k_B T}\right), \quad (51)$$

where ΔG_f is the formation energy of one Frenkel pair. In general each of the concentrations may be further constrained by other processes¹⁵. At 1673 K, the calculated value for ΔG_f gives a value for the right hand side of equation 51 of $5.6 \cdot 10^{-15}$. We can thus expect that the effect of hypostoichiometry (oxygen vacancy production) will, through equation 51, reduce the oxygen interstitial concentration to negligible proportions and that oxygen interstitials will play little role in hypostoichiometric urania.

In stoichiometric UO_2 , the situation is suddenly altered¹⁶. Here, through equation 51, a population of intrinsically created oxygen interstitials becomes available to take part in reactions with other lattice defects. Where, in hypostoichiometric UO_{2-x} , trivacancies were the dominant Mo site, in UO_2 the following reaction path now becomes available.



Thus in exactly stoichiometric UO_2 , the divacancy is the dominant site for Mo. The process shown in equation 52 is however limited through equation 51; there is no endless supply of oxygen interstitials. In particular, if the concentration of Mo becomes large the process described by equation 52 will no longer be able to play its full role¹⁷ and we may expect that an increasingly larger fraction of the Mo will remain in trivacancies - the behaviour shown in Figure 14.

¹⁵ These further constraints may be written as extra multiplicative terms on the right hand side of equation 51 as was shown in Chapter 2. These terms have been left out of equation 51 for the sake of the simplistic explanation of the role of oxygen interstitials that follows.

¹⁶ "Suddenly" in the sense that it is only very close to stoichiometric composition that the extrinsic, composition controlled processes cease to dominate Mo behavior.

¹⁷ That is, we can no longer ignore the extra constraints not included in equation 51.

As we increase the degree of hyperstoichiometry, we introduce excess extrinsic oxygen into the lattice. The evidence, from both experiment and computation, that this oxygen is accommodated as oxygen interstitials is overwhelming. With the availability of an extrinsic supply of oxygen interstitials in UO_{2+x} , a second reaction path becomes readily available, allowing single uranium vacancies to form majority sites for the Mo.



As the concentration of Mo increases the oxygen interstitial supply will become unable to sustain this process and at high concentrations divacancies and trivacancies again dominate. The rationale behind the location of Mo in the urania is thus identical to that given for Xe.

In practice, calculations show that a neutral Mo atom at a uranium vacancy is not a particularly populous defect at any stoichiometry. To understand why, we need to consider the effect of stoichiometry on charge transfer reactions.

In our model we employ an atomistic picture of localised charge carriers. Thus, if we consider the transfer of an electron from a neutral Mo atom to the UO_2 lattice we may, as was outlined in Chapter 2, write an equation such as,



where the charge on a lattice uranium is reduced from the formal charge of $4+$. Had there been a population of U^{5+} ions we could have written:



Using our calculated defect energies for U^{3+} and U^{5+} at normal lattice sites and tabulated ionization potentials (these data will be found in Tables 1 and 7) we find that of the two processes, the second is more favourable by about 3.9eV . This is important, for if we consider the ionization of Mo located in a uranium vacancy for example, we find that the first of these two processes is not viable but the second is.

As the degree of hyperstoichiometry is increased the lattice needs not only to accommodate the excess oxygen (as O^{2-} interstitials) it must also retain electroneutrality. The model we use for this, is the process,



where we have employed Kröger-Vink notation. The symbol h^{\bullet} denotes a hole which, in our model of localised charges, must be located on a localised species in the system. In pure urania (no fission products) one possibility is the creation of U^{5+} ions. Another is the creation of U^{6+} ions. Using our calculated defect energies and the tabulated ionization energies we find that, in agreement with the previous work of Catlow [29], U^{5+} are the most likely means of retaining electroneutrality. It should be remembered that the errors in the data are significant and U^{6+} may well be an important charge state in urania. What is important here, however, is the point that increasing oxygen excess leads to an increased hole concentration and the release of more favourable paths for the ionization of Mo. We thus find for example, that in $UO_{2.001}$ most of the isolated Mo is present as Mo^{1+} whereas in $UO_{2.2}$ Mo^{3+} is the most populous state. The location of Mo at U vacancies in UO_{2+x} is thus associated with ionization of the Mo.

As it is such an important point, we should look in detail at the process of ionization of Mo at the uranium vacancy site:



When calculating the change in energy ΔE of this process, it is useful to divide this energy into two components; the change in energy due to a change in defect types ΔD ¹⁸ and the change due to charge transfer from $Mo^{(n-1)+}$ to U^{5+} , ΔIP . This last component is estimated as the 5th ionization potential of uranium subtracted from the nth ionization

¹⁸ For example, the energy change in the lattice on substituting a U^{5+} ion with a U^{4+} ion without worrying where the U^{4+} came from or where the U^{5+} goes.

potential of Mo. These two components together with the total energy change are plotted in Figure 17 for values of n from 1 to 6¹⁹. We see a steady decrease in ΔD with increasing n due to the higher charge and smaller ionic radius of Mo. The increase in ΔIP is, however, well known to be non-linear and the jump in ΔIP at $n=4$ pushes ΔE well into the positive range when attempting to form Mo^{4+} (and indeed Mo^{5+} and Mo^{6+}). This is the reason why, in our model, Mo^{4+} ions at uranium vacancies do not form.

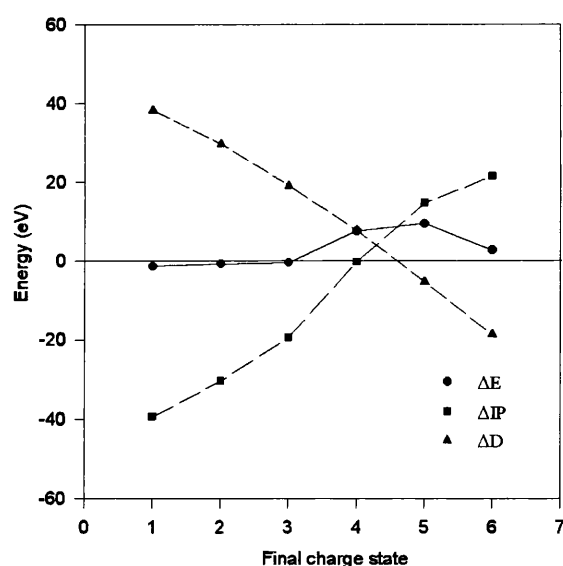
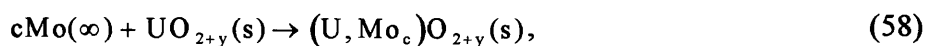


Figure 17. Breakdown of the energy contributions to Mo charge transfer reactions of the form shown in equation 57. Where the final charge on the Mo is less than 4+, the total energy for these reactions are negative. ΔE is the total energy; ΔIP , ΔD are defined in the text, where a full discussion will be found.

¹⁹ Values of 7 and above are not investigated as the 7th ionization potential of Mo is prohibitively high for further ionization to be an important process.

Finally, a parameter that may be of some interest is the free energy change that occurs when we add Mo to a crystal of previously pure urania. We know that the location of the Mo in the lattice (assuming that precipitation does not occur) is dependent on both the composition of the urania (stoichiometry) and the amount of Mo we add. We therefore get a distribution of Mo in various states where the population of each state depends upon these two parameters. Once we have added the Mo, the difference in the free energy of the crystal with and without Mo is thus given by a weighted sum of the energies and configurational entropies of these states together with any contributions arising from a change in the intrinsic defect populations (for example a change in the number of oxygen interstitials). It should be emphasised that the term “free energy” is used in a rather loose way here to indicate that a defect configurational entropy term has been included. Changes in vibrational entropy on defect formation are not, however, calculated and thus the true change in free energy will vary from that given here. The energy difference, ΔE , calculated is equivalent to that associated with the reaction,



where $\text{Mo}(\infty)$ signifies a Mo atom at infinity. In what follows, we assume that $\text{Mo}(\infty)$ can be replaced by a Mo atom in the gaseous state, $\text{Mo}(\text{g})$, without appreciably affecting the energy change associated with equation 58.

In Figure 18 we have plotted this change in free energy (per Mo atom) as a function of the O/U ratio and Mo concentration. For convenience ΔE has been plotted only for the region $\Delta E \geq 0$. When $\Delta E > 0$ the reverse of equation 58 will be spontaneous and Mo in the gas phase will be favoured above Mo in solution in UO_{2+y} (where y takes positive and negative values). When $\Delta E < 0$ the forward direction of equation 58 is preferred and solution of Mo in UO_{2+y} is favoured above the gaseous state. This is a significant point which shall be returned to later.

The value of ΔE is easily related to the Mo behaviour already discussed and shown principally in Figures 13 and 15²⁰. In UO_{2-x} , where Mo is located exclusively in trivacancies, the energy change is large and positive, indicative of an insoluble nature for Mo. In UO_{2+x} however, we find that the location of Mo in uranium vacancies may (dependent upon Mo concentration) result in Mo in solution being favoured above Mo in the gaseous state. This does not, however, necessarily translate into an observable solubility of Mo, for we can further consider the reaction,



where the metal phase of Mo is produced. This process can be used as an approximation for the precipitation of Mo into the five metal particles. The energy change associated with this reaction may be approximately written as $-(\Delta E + \Delta E_{\text{sub}})$ where ΔE is the free energy change of equation 58 and ΔE_{sub} is the free energy change upon sublimation of metallic Mo. The enthalpy of sublimation of Mo over a wide temperature range is about 6.5 to 6.8 eV per atom [62] and the free energy change associated with sublimation, though less than this, is probably still quite substantial (and positive) at the temperature considered here (that is, at 1673K). Hence, precipitation will be favoured for those regions of the ΔE plot in Figure 18 with values $(\Delta E + \Delta E_{\text{sub}}) > 0$.

At large degrees of hyperstoichiometry and small Mo concentrations (the most favourable solubility conditions calculated for single Mo atoms) the calculated energy change on adding Mo is never much less than -1 to -2 eV. Hence even in the regions of concentration and O/U ratio most favourable to solution of Mo in urania, precipitation is

²⁰ Perhaps the only feature not obviously explained by these other figures is the slope seen in Figure 18 for lines of constant O/U ratio where there is no apparent change in Mo location (see for example the line for O/U=1.9 where trivacancies are the only Mo site at any concentration). This slope has its origin in the influence of the changing configurational entropy with Mo concentration.

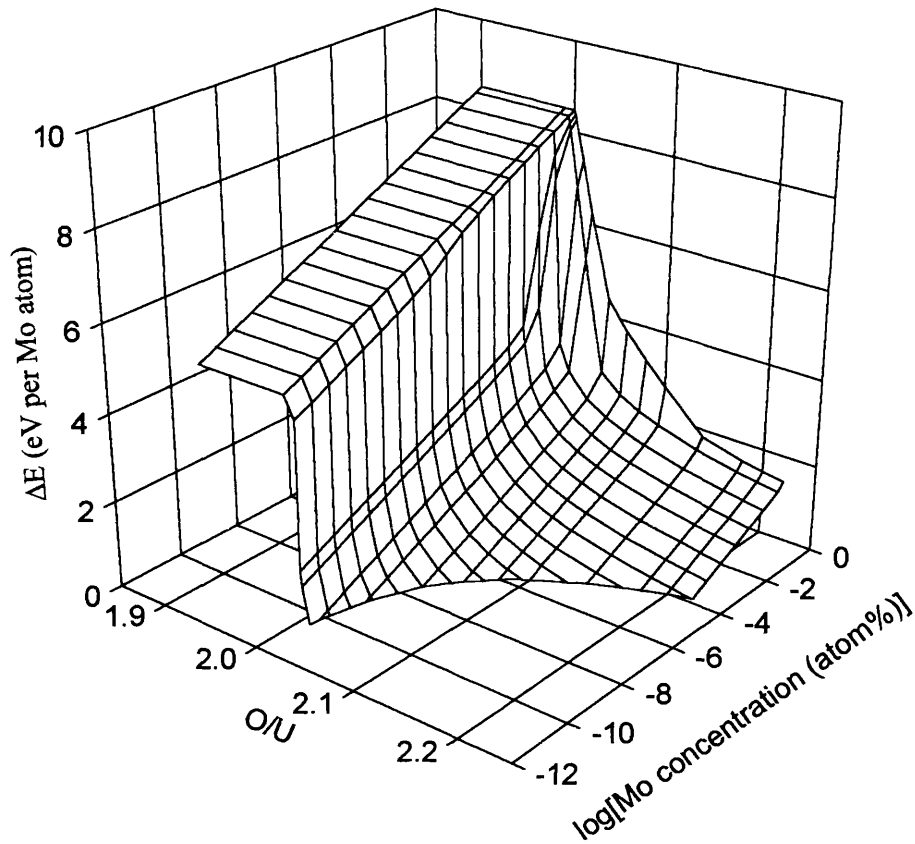


Figure 18. Plot of the free energy change ΔE occurring when single Mo atoms in the gas phase are added to pure urania at a fixed O/U ratio (only the region $\Delta E > 0$ is shown). The region where $\Delta E > 0$ favours precipitation and/or high release of Mo (see discussion). When the plot cuts the $\Delta E = 0$ plane and becomes negative, solution of Mo in urania is preferred over the Mo gas phase. Precipitation of Mo is still possible, however (see discussion in text).

likely to be preferred. This precipitation may be into a metallic form as discussed here, however, it is also in the high hyperstoichiometry region that the oxygen potential favours the formation of various oxide precipitates and this question has not been considered here. Precipitates would thus be likely to form over the whole stoichiometry range, providing the kinetics of this were not a barrier.

When the kinetics are a barrier, as in the case of trace irradiated urania, then the “solubility” of single Mo atoms should be enhanced with increasing O/U ratio and reducing Mo concentration. That is, Mo solution is preferred to Mo in the gaseous state. This would presumably have the effect of reducing Mo release. It can be seen from Figure 18 that as the Mo concentration is decreased, the value of the O/U ratio where $\Delta E=0$ approaches closer to the stoichiometric composition. It is tempting to relate this result to the experimental data of Prussin and co-workers [60] which showed only a small Mo release (a release intermediate between those found for soluble and insoluble fission products) from trace irradiated samples of urania thought to be very close to stoichiometric composition even though the results of Giacchetti and Sari [59] showed no appreciable solubility for Mo in urania.

If this simple analysis of equation 58 is correct then it does present some problems to be resolved concerning the oxygen potential buffering effect of Mo in reactor fuels. Unless five metal particles can themselves be oxidised in the fuel, and there is no published data at present which supports this²¹, then oxidation of Mo can proceed only for the Mo dispersed through the urania lattice (we ignore for the moment the possibility of the further oxidation of Mo already present in oxide precipitates or gases). The dispersed Mo will originate through three main processes; creation through fission, fission induced resolution from metallic precipitates and thermal resolution from metallic precipitates.

²¹ An example of such support would be if an oxidised shell were observed on five metal particles in high burn up fuel. It is understood, however, that the characterisation of precipitates of such small dimensions as those of the five metal particles, is often quite difficult.

The amount of Mo produced by the last of these processes will be related to the factor $\exp[-(\Delta E + \Delta E_{\text{sub}})/k_B T]$ and the total amount present in solution will depend on the kinetics of the precipitation process unless equilibrium is obtained. From the calculations given here, we know that the thermal resolution of Mo from metallic precipitates is enhanced through the increase of the O/U ratio (and hence oxygen potential) and that oxidation up to Mo^{3+} is likely in hyperstoichiometric urania. Although we have not attempted to do so here, it should be feasible to calculate the amount of Mo in solution and the average oxidation state as a function of fuel burn up. It should also be possible to calculate the free energy change associated with the closed system reaction,



and hence attempt to plot metallic/oxide precipitation of Mo as a function of O/U ratio and Mo concentration for a closed model system. This would, of course, only be an approximation to the true open system where the oxygen potential is the important parameter, but it would be instructive nevertheless.

6.6 Summary

It is useful now to summarise the main results of our calculations. Firstly, concerning the location and charge state of *those Mo atoms dispersed through the urania lattice*, we can say:

- In UO_{2-x} , Mo will be present as neutral atoms in trivacancy sites.
- In UO_2 , Mo will be present as neutral atoms in di- and trivacancy site with perhaps a minor amount in single uranium vacancies.
- In UO_{2+x} , Mo will be found principally in single uranium vacancies with charge states from 0 to 3+. Increased oxidation of the Mo is related to increases in O/U ratio.

A plot of the energy change associated with adding Mo atoms in the gaseous state to urania suggests that this process is favourable at low Mo concentrations in UO_{2+x} . A

similar process where the Mo begins in the metallic state is probably not favoured at any stoichiometry and hence precipitation of Mo in urania is likely, as is experimentally observed. The oxygen potential buffering effect of Mo in urania, in part at least, originates from the oxidation of that dispersed Mo focused upon in this chapter. On the basis of the results given here and some further work, it should be possible to calculate the amount and average charge state of Mo in the lattice as a function of burn up and hence test whether our results are in agreement with the recent experimental measurements of Matzke [56].

7 Ru, Rh and Pd

7.1 Introduction

The close physical association often observed in reactor fuels between Mo and the metals Tc, Ru, Rh and Pd has already been noted in Chapter 6. Although all five of these elements are seen to alloy together into solid precipitates in the fuel, there are some subtle differences which make the calculated solubility of Mo rather higher than that of the others. To understand this behaviour better and to complement the results already given for Mo, in this chapter we discuss the findings of a computer simulation study into the behaviour of Ru, Rh and Pd in urania. Although all three of these elements are calculated to be insoluble in urania, on the atomic scale the behaviour of Pd is found to be different from that of Ru and Rh, while these latter exhibit close similarities to the behaviour of Mo.

7.2 Experimental knowledge

In studies of reactor fuels, it has been observed that the most common location for Ru, Rh and Pd is with Mo and Tc in the “five metal particles” (white phase precipitates). These particles have already been discussed in Chapter 6. Although there may be some conditions under which these elements form other compounds in reactor fuels (see below) this is generally of minor importance. With the exception of Mo, it is usually assumed that Tc, Ru, Rh and Pd can be regarded as generally insoluble in UO_2 (the more complicated case of Mo has already been discussed).

The actual amounts of these elements present in a reactor fuel are, of course, dependent upon the reactor nature and history. In general however, Ru concentrations are less than

those of Mo with significantly less Tc, Rh and Pd being present [36]. This is often reflected in the composition of the five metal particles. Yields for Ru, Rh and Pd are approximately doubled for Pu fission as compared to U fission [58] and in mixed fuels this may bring Ru concentrations much closer to those of Mo.

In Figure 19, the partial molar Gibbs free energies for the oxides of Ru, Rh and Pd are given. As was the case for Figure 12 in Chapter 6, we write for each fission product the equation for the formation of the solid oxide from the metal as,



and plot the Gibbs free energy of formation (ΔG_F) for this equation. We note, however, that here ΔG_F is plotted against the temperature, rather than being superimposed on a plot of the fuel oxygen potential vs. O/U ratio. This diagram demonstrates the increasingly noble character of the metals as the atomic number is increased from Ru through to Pd. In particular, when reference is made to the variation of oxygen potential with O/U ratio in Figure 12, it is seen that solid oxides of Ru, Rh and Pd are unlikely to occur in UO_{2+x} and this is borne out by experimental observations.

Although solid oxides of Ru, Rh and Pd have apparently never been reported in reactor fuels, Kleykamp [36] suggested that Mo and Ru may undergo radial transport as gaseous MoO_3 and RuO_3 in order to explain observed enrichments in these elements at a relative radius of about 0.6 in some fuels. Certainly, large radial fissures may form in high burn up fuels, creating a possible path for gaseous transport but the exact mechanisms of gaseous oxide formation and its relationship to subsequent alloy formation is unclear.

Pd is the noblest of the three metals discussed in this chapter and although it does not form oxides in the fuel, it has been observed as a component of other metal alloys in addition to the five metal particles. Alloys of Pd, Ag and Cd and Pd, Sn, Sb and Te amongst others have been observed [36] although these are much less common than the

five metal particle themselves. Additionally, at high temperatures and *very* low oxygen potentials Rh and Pd may form precipitates with the actinides of the form (U,Pu)(Rh,Pd)₃. URu₃ is not normally observed although its formation is thought to be theoretically possible at high temperatures [36].

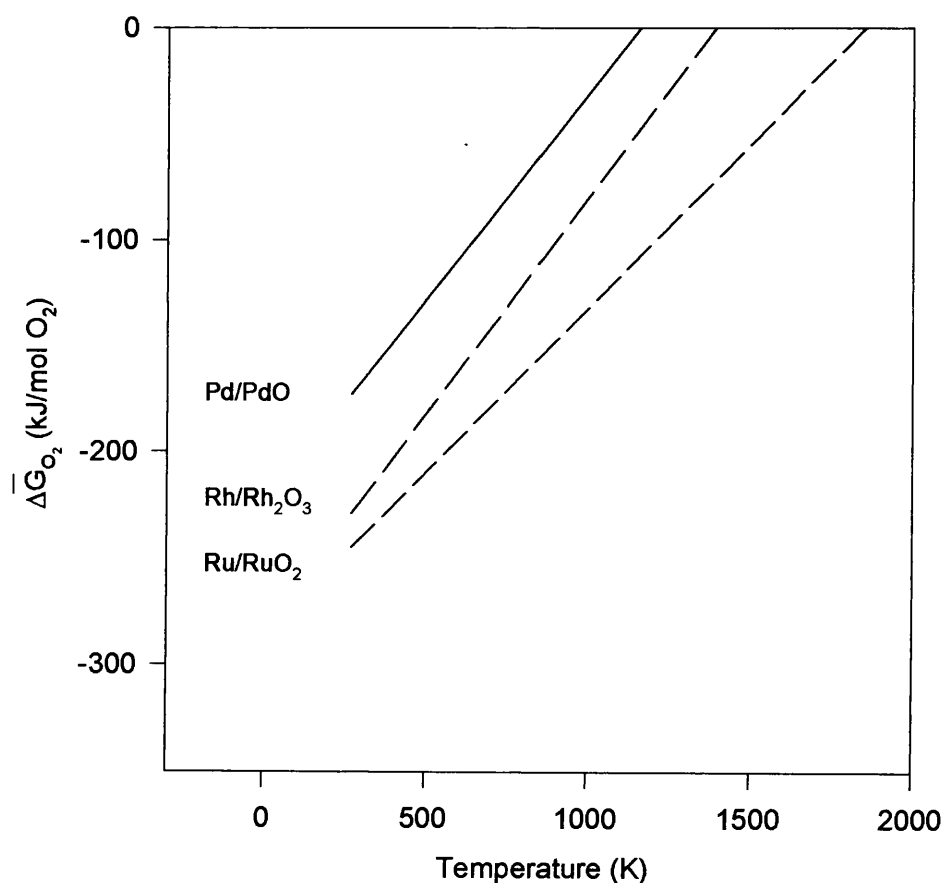


Figure 19. The relative partial molar Gibbs free energies of oxygen of the oxides of Ru, Rh, and Pd. A redrawn portion of a figure from [36].

In the fission product release studies of Prussin and co-workers [60] Ru was placed in the same class as Xe on the basis of its ease of release from near stoichiometric UO_2 . This was in contrast to Mo whose release could neither be categorised with the insoluble neutral fission products such as Xe nor soluble fission products which were not released at all (see Chapter 6 for a discussion on Mo release characteristics).

7.3 The computer simulation of Ru, Rh and Pd

Generally, the approach adopted here for simulating the behaviour of Ru, Rh and Pd in UO_2 follows the spirit of that used for Mo and outlined in Chapter 6. Once defect energies were derived, occupancies of the various possible sites for atoms of these elements were calculated using equations 7 with the system temperature fixed at 1673 K. This allows direct comparison between these results and those reported earlier for Mo. Again, temperature dependency only enters via the configurational terms in equations 7 and no attempt was made to calculate the effect of temperature upon individual defect energies, which were thus internal energy changes and not changes in free energy. No interaction terms between separate defects were included.

Once more, the potentials of Jackson and co-workers [42] are used for modelling the UO_2 lattice and also in deriving “empiricised” potentials for the interactions between fission product and host lattice atoms (see Chapter 3 for a description of this approach). Fission product charge states from 0 to 3+ were included in the final analysis, with higher charge states being unimportant for the fission product sites considered. Potentials were fitted to the Buckingham form and are given in Tables 9, 10, and 11.

Examination of these tables reveals some apparent inconsistencies in the values derived for A and ρ values for the neutral atoms when these are compared with the trends apparent with the interactions of the charged ions (e.g. increasing A and decreasing ρ with increasing ionic charge). As was the case with Mo, these discrepancies derive from

the origin of the electron densities used in calculating potentials and were unfortunately unavoidable. Whereas the HERSKILL program (see Chapter 3) was used to derive electron densities for the charged ions, densities for the neutral atoms could only be calculated from expansion of tabulated wave functions for the ground state of the free atom (these were obtained from [64]). This is not, however, thought to be a major source of error.

Interaction	A (eV)	ρ (Å)	C_6 (eVÅ ⁶)
Ru-O ²⁻	465.85	0.425759	123.17
Ru ¹⁺ -O ²⁻	405.079	0.449469	45.02
Ru ²⁺ -O ²⁻	592.829	0.427258	29.09
Ru ³⁺ -O ²⁻	794.782	0.403734	19.23
Ru-U ⁴⁺	4399.17	0.352474	93.57
Ru ¹⁺ -U ⁴⁺	4645.64	0.347558	36.60
Ru ²⁺ -U ⁴⁺	6016.84	0.317341	24.29
Ru ³⁺ -U ⁴⁺	7956.11	0.287115	11.21

Table 9. Short range potentials for Ru interactions.

Interaction	A (eV)	ρ (Å)	C_6 (eVÅ ⁶)
Rh-O ²⁻	522.909	0.416615	97.56
Rh ¹⁺ -O ²⁻	449.635	0.444492	34.73
Rh ²⁺ -O ²⁻	644.827	0.421021	22.24
Rh ³⁺ -O ²⁻	844.285	0.399257	14.50
Rh-U ⁴⁺	4515.69	0.348891	75.31
Rh ¹⁺ -U ⁴⁺	5001.91	0.33997	28.70
Rh ²⁺ -U ⁴⁺	6320.46	0.313262	18.86
Rh ³⁺ -U ⁴⁺	7341.64	0.297081	12.57

Table 10. Short range potentials for Rh interactions.

Interaction	A (eV)	ρ (Å)	C_6 (eVÅ ⁶)
Pd-O ²⁻	616.256	0.421894	80.16
Pd ¹⁺ -O ²⁻	500.365	0.437717	27.98
Pd ²⁺ -O ²⁻	701.653	0.414365	17.68
Pd ³⁺ -O ²⁻	898.529	0.394422	11.50
Pd-U ⁴⁺	6679.39	0.312382	62.72
Pd ¹⁺ -U ⁴⁺	5454.24	0.331905	23.42
Pd ²⁺ -U ⁴⁺	6762.35	0.308154	15.18
Pd ³⁺ -U ⁴⁺	7760.91	0.293592	10.08

Table 11. Short range potentials for Pd interactions.

Comparison of the interactions of the neutral atoms of Mo (Table 5) Ru, Rh and Pd, with O^{2-} indicates that all but the Pd- O^{2-} interaction follow the pattern of decreasing ρ with increasing atomic number. This anomaly is related to the closed 4d electronic structure of the Pd ground state and, as will be seen, is responsible for some differences in behaviour on the atomic scale between Pd, Mo, Ru and Rh²².

C_6 parameters for the long range dispersive interactions were derived using the Slater-Kirkwood formula as outlined in Chapter 3. In this regard, the polarizabilities employed were again estimated. Interpolation between an experimental value for the polarizability of a neutral Mo atom [62] and a theoretical value for neutral Pd [61] was used to derive estimates for the neutral atom polarizabilities of Ru and Rh. The polarizabilities of the charged ions were estimated by assuming that they scaled with ionic charge in the same way as the polarizabilities estimated for Mo;

$$\alpha(M^{n+}) = \frac{\alpha(M^0)}{\alpha(Mo^0)} \cdot \alpha(Mo^{n+}). \quad (62)$$

This approach to the estimation of polarizabilities is necessitated by the lack of appropriate values in the literature. No allowance for the crystalline environment is made when estimating α values. Although this may be seen as a further deficiency in the model, attempting to include such effects would be problematic and lead to uncertainties regarding the transferability of potentials between the several different fission product sites considered. The environment at an oxygen vacancy for example, differs, of course, from that at an uranium vacancy.

²² The electronic structures for the neutral atoms used in deriving electron densities were:



	α (\AA^3)	Y	K ($\text{eV}\text{\AA}^{-2}$)
Ru	5.61	7.0	125.77
Ru ¹⁺	1.50	7.0	470.39
Ru ²⁺	0.88	7.0	801.81
Ru ³⁺	0.54	7.0	1306.65
Rh	4.08	7.0	172.94
Rh ¹⁺	1.09	7.0	647.33
Rh ²⁺	0.64	7.0	1102.48
Rh ³⁺	0.39	7.0	1809.21
Pd	3.14	7.0	224.71
Pd ¹⁺	0.84	7.0	839.99
Pd ²⁺	0.49	7.0	1439.98
Pd ³⁺	0.30	7.0	2351.97

Table 12. Polarizability data for Ru, Rh and Pd used in shell model and Slater-Kirkwood formula.

As was the case with Mo, the effective number of polarizable electrons, P , used in the Slater-Kirkwood expression, were fixed at 7.0 for all fission product ions. The same electron numbers together with the estimated polarizabilities, were also used in the shell model and are tabulated in Table 12. The ionization potentials used in deriving the final defect concentrations are given in Table 7; they are taken from [62] and [63].

7.4 Results

Tables 13, 14 and 15 report the basic defect energies calculated using the CASCADE program for Ru, Rh and Pd respectively at various site in urania. These energies were used in the approach outlined in Chapter 2 to calculate fission products site occupancies at various values of fission product concentration and O/U ratio.

Unfortunately, as may be seen from the tables of defect energies, not all the CASCADE calculations converged. In particular, none of the calculations involving charged fission product ions at single oxygen vacancies were successful. However, only in the case of Pd is the oxygen vacancy seen to be an important fission product location and the omission of these particular type of defect from the final analysis of defect concentrations is not thought to be serious. Calculations for the neutral atoms at oxygen vacancies were successful for all three of the fission products considered.

Additionally, for all except neutral Pd at the divacancy site, calculation of defect energies for neutral atoms at di- and trivacancy sites were initially unsuccessful. As was the case for Mo in Chapter 6, calculation of defect energies in these cases were completed by removing the shells from the fission product atoms. As with Mo, this is thought to introduce only a small additional error into the final results.

Defect	Energy (eV)	Defect	Energy (eV)
Ru at V_U	83.29	Ru at divacancy	97.58
Ru ¹⁺ at V_U	76.17	Ru ¹⁺ at divacancy	91.16
Ru ²⁺ at V_U	59.00	Ru ²⁺ at divacancy	74.86
Ru ³⁺ at V_U	31.96	Ru ³⁺ at divacancy	48.42
Ru at V_O	26.91	Ru at trivacancy	112.59
Ru ¹⁺ at V_O	-	Ru ¹⁺ at trivacancy	107.08
Ru ²⁺ at V_O	-	Ru ²⁺ at trivacancy	91.91
Ru ³⁺ at V_O	-	Ru ³⁺ at trivacancy	66.18
Ru interstitial	12.65		
Ru ¹⁺ interstitial	10.18		
Ru ²⁺ interstitial	-5.01		
Ru ³⁺ interstitial	-30.99		

Table 13. Defect energies for Ru in UO₂ calculated with CASCADE.

Defect	Energy (eV)	Defect	Energy (eV)
Rh at V_U	83.54	Rh at divacancy	97.79
Rh ¹⁺ at V_U	76.48	Rh ¹⁺ at divacancy	91.48
Rh ²⁺ at V_U	59.07	Rh ²⁺ at divacancy	74.95
Rh ³⁺ at V_U	32.02	Rh ³⁺ at divacancy	48.52
Rh at V_O	27.03	Rh at trivacancy	112.76
Rh ¹⁺ at V_O	-	Rh ¹⁺ at trivacancy	107.41
Rh ²⁺ at V_O	-	Rh ²⁺ at trivacancy	92.04
Rh ³⁺ at V_O	-	Rh ³⁺ at trivacancy	66.33
Rh interstitial	12.99		
Rh ¹⁺ interstitial	10.46		
Rh ²⁺ interstitial	-4.92		
Rh ³⁺ interstitial	-30.84		

Table 14. Defect energies for Rh in UO₂ calculated with CASCADE.

Defect	Energy (eV)	Defect	Energy (eV)
Pd at V_U	84.41	Pd at divacancy	97.18
Pd ¹⁺ at V_U	76.55	Pd ¹⁺ at divacancy	91.55
Pd ²⁺ at V_U	58.98	Pd ²⁺ at divacancy	74.88
Pd ³⁺ at V_U	31.93	Pd ³⁺ at divacancy	48.45
Pd at V_O	26.21	Pd at trivacancy	113.14
Pd ¹⁺ at V_O	-	Pd ¹⁺ at trivacancy	107.50
Pd ²⁺ at V_O	-	Pd ²⁺ at trivacancy	92.00
Pd ³⁺ at V_O	-	Pd ³⁺ at trivacancy	-
Pd interstitial	13.11		
Pd ¹⁺ interstitial	10.38		
Pd ²⁺ interstitial	-5.07		
Pd ³⁺ interstitial	-30.93		

Table 15. Defect energies for Pd in UO_2 calculated with CASCADE.

7.4.1 Ru

The calculated locations for Ru in urania are found to be similar to those calculated for Mo. In UO_{2-x} virtually all single atoms of Ru will be located at trivacancy sites as neutral atoms. In Figure 20, this is shown by plotting the percentage of single Ru atoms at trivacancies as a function of Ru concentration²³ and O/U ratio. The sudden drop in the population in trivacancies when the O/U ratio becomes greater than or equal to 2 is similar to that found for Mo (see Chapter 6). As was the case with Mo, this drop is compensated for near stoichiometric composition by an increase in the proportion of Ru (again as neutral atoms) at divacancy sites, as shown in Figure 21. In UO_{2+x} , only at very high concentrations does the trivacancy have some importance as a site for Ru.

Although the proportion of Ru in divacancy sites may reach values of over 80% of the total Ru concentration, this is restricted to a region very close to stoichiometric composition at low and medium concentrations. In both hyper- and hypostoichiometric regions the proportion of Ru in divacancies is seen, in the main, to be negligible. There is, however, a narrow band at high concentrations where the divacancy again gains importance as a site for Ru in UO_{2+x} . The position of this band is dependent upon Ru concentration and O/U ratio. Due to its narrowness it is not properly resolved with the mesh size used in Figure 21 and hence appears as two anomalous peaks.

For O/U ratios in the hyperstoichiometry region, single Ru atoms are most likely to be found in uranium vacancies as indicated in Figure 22. It is in these locations that Ru may ionize to higher charge states. However, this occurs far less readily than was the case for Mo. In particular, charge states higher than Ru^{2+} are not calculated to occur for Ru atoms dispersed in urania. In Figure 23, we break down the population of Ru at uranium vacancies into its component charge states.

²³ That is, the concentration of single, isolated Ru atoms in the system.

The rationale for the observations given above will be discussed shortly. First, however, the results for Rh and Pd are outlined.

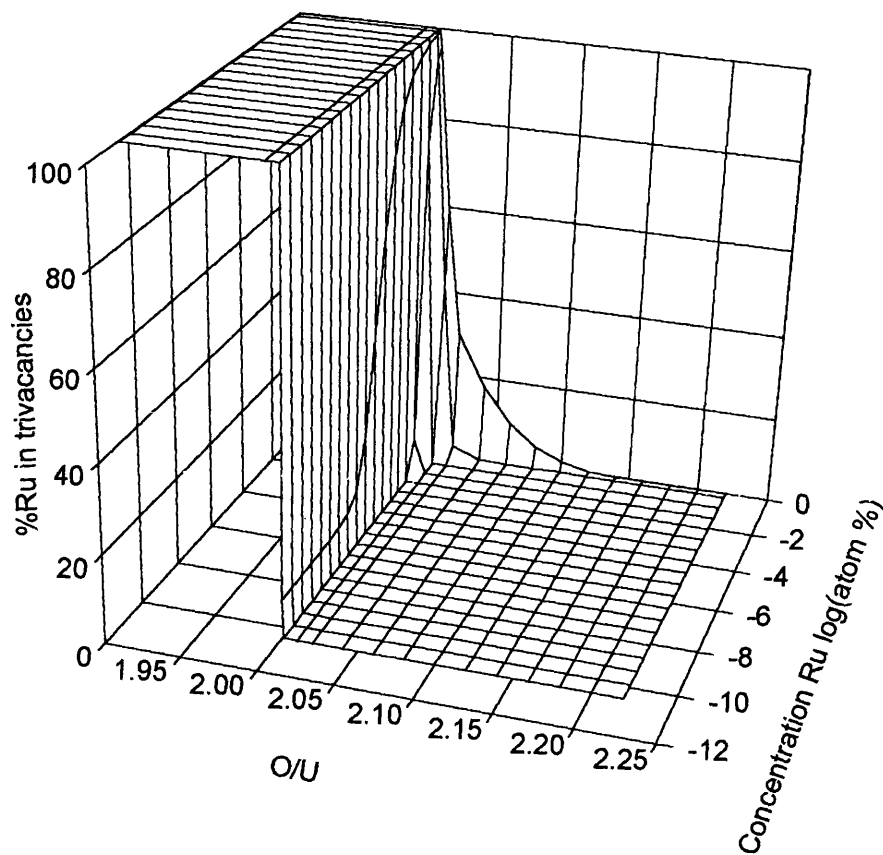


Figure 20. Proportion of single atoms of Ru occupying trivacancies in urania as a function of stoichiometry and Ru concentration. As already mentioned, all data and figures to be discussed refer to calculations at $T=1673\text{K}$.

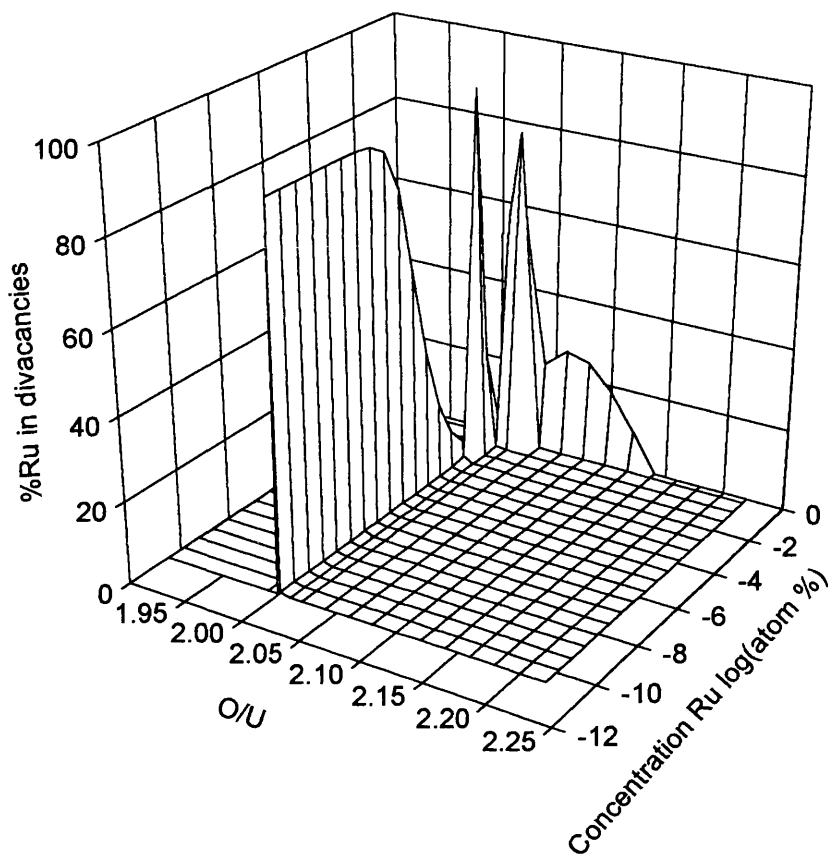


Figure 21. Proportion of single atoms of Ru occupying divacancy sites in urania as a function of stoichiometry and Ru concentration. The apparently anomalous peaks at high concentrations indicate a fine feature that cannot be resolved properly with the mesh size used in this plot. See main text for further details.

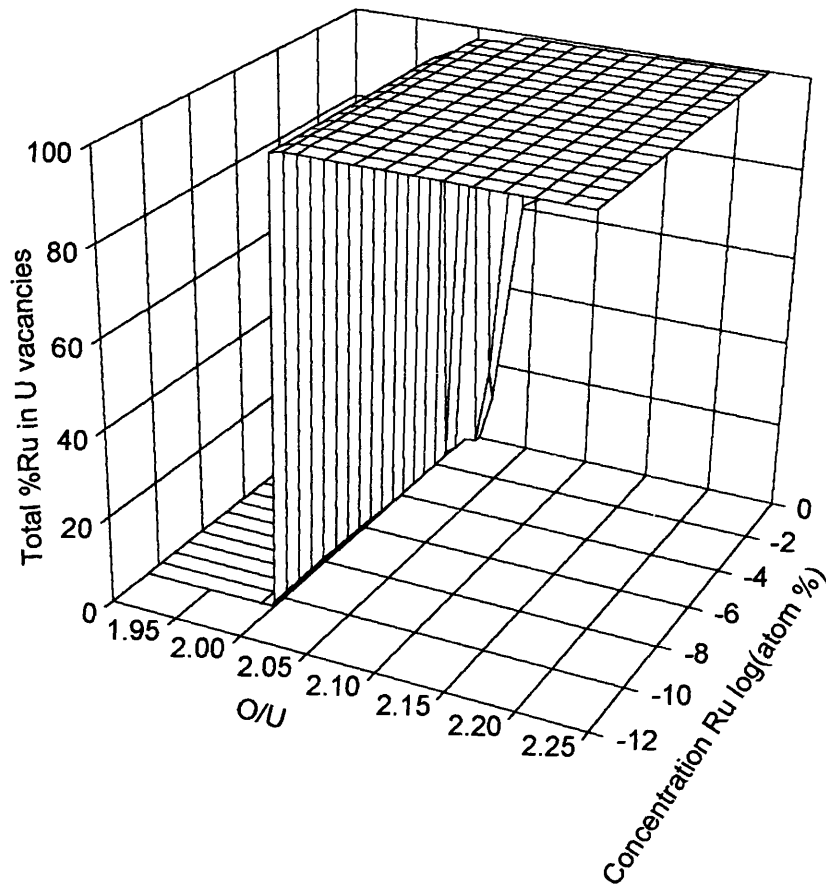
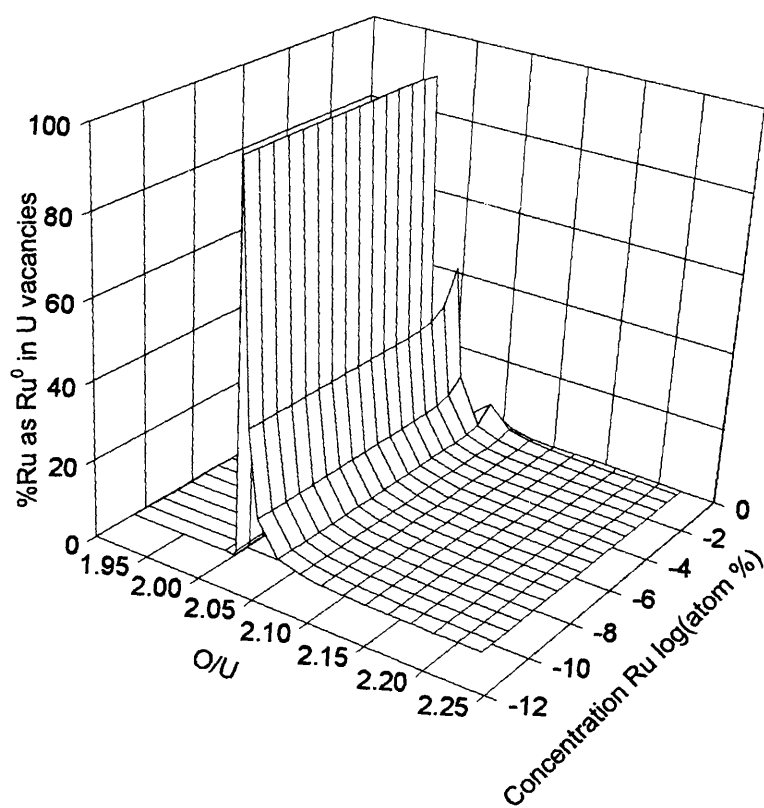
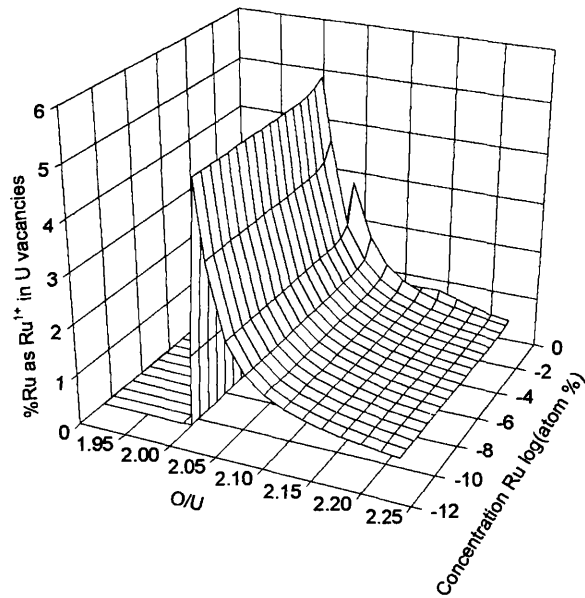


Figure 22. Proportion of single Ru atoms occupying uranium vacancy sites in urania as a function of stoichiometry and Ru concentration.

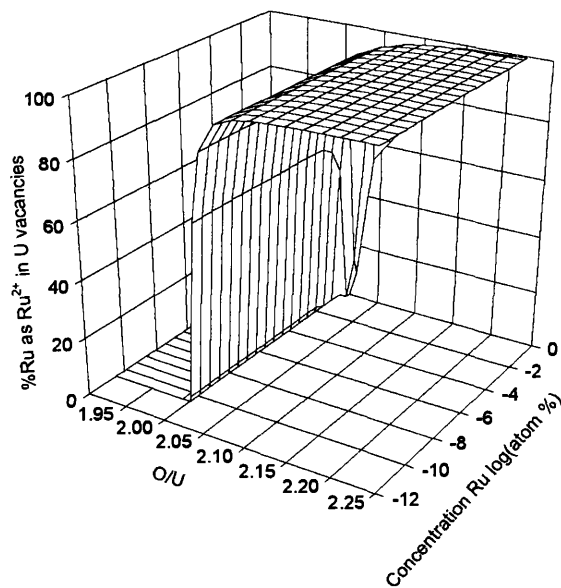


a)

Figure 23. Proportion of single Ru atoms occupying uranium vacancy sites as charged ions. a) Proportion as neutral Ru. This figure is continued overleaf.



b)



c)

Figure 23 continued. b) Proportion of Ru atoms as Ru^{1+} in U vacancies. c) Proportion of Ru atoms as Ru^{2+} in U vacancies.

7.4.2 Rh

The behaviour of Rh is quite similar to that of Ru and Mo. For $O/U < 2$, almost all single Rh atoms will be located in trivacancies. For $O/U > 2$, Rh is only found in trivacancies at high Rh concentrations. This behaviour is shown in Figure 24.

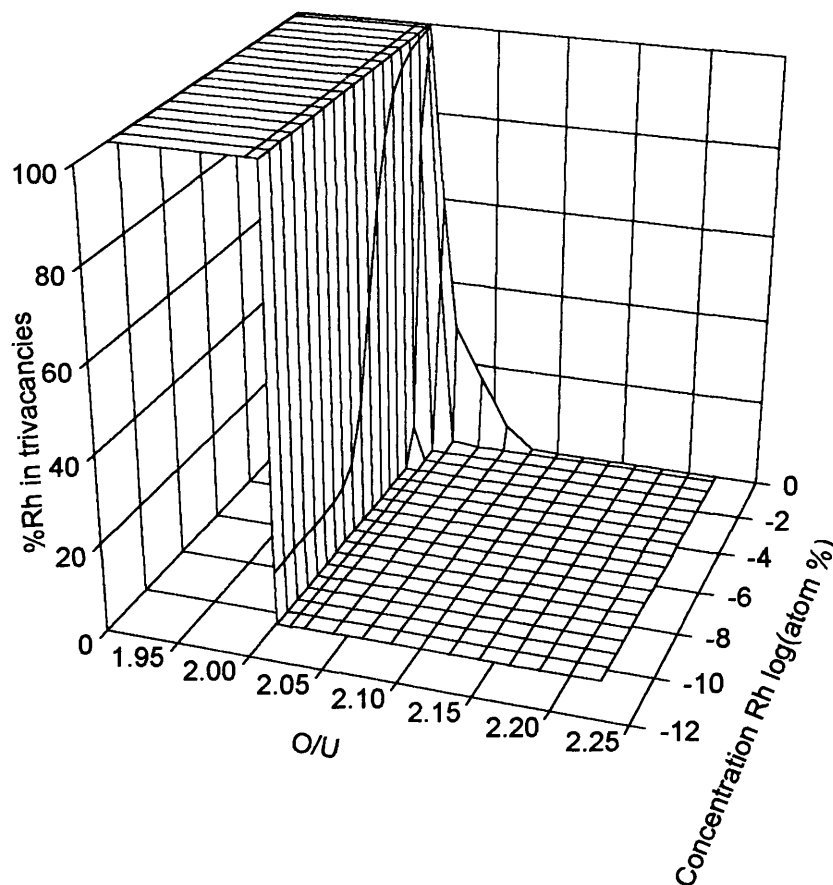


Figure 24. Proportion of single Rh atoms occupying trivacancy sites in urania as a function of stoichiometry and Rh concentration.

Near the stoichiometric composition a large proportion of Rh is located at divacancy sites. Approximately 87% of the total population of single atoms are calculated to be in divacancies for $O/U=2$ providing the Rh concentration is not too great. See Figure 25.

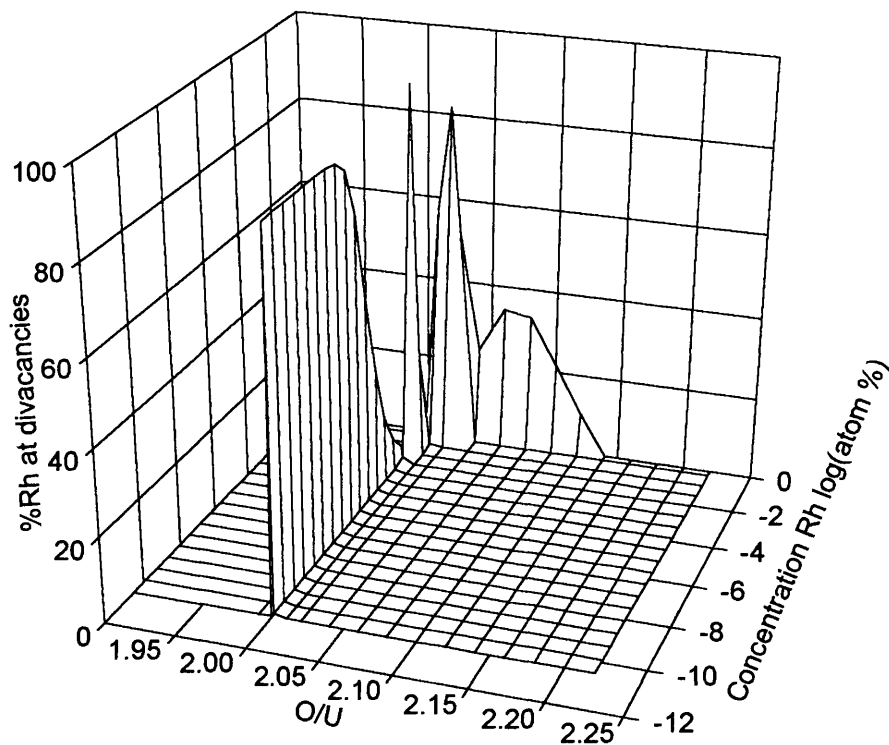


Figure 25. Proportion of single Rh atoms occupying divacancy sites in urania. The peaks at high concentrations are again a result of the mesh size being too coarse to resolve a fine feature. See main text for further details.

Again, occupation of single uranium sites is important when $O/U > 2$ and, as shown in Figure 26, Rh atoms at uranium vacancies may again lose electrons to form higher charged ions but the process is even less marked than was the case with Ru. Although charge states up to Rh^{2+} are calculated to be stable, only a small proportion of the Rh will be doubly ionized even at quite high degrees of hyperstoichiometry²⁴. A breakdown of Figure 26 into the component charge states is given in Figure 27.

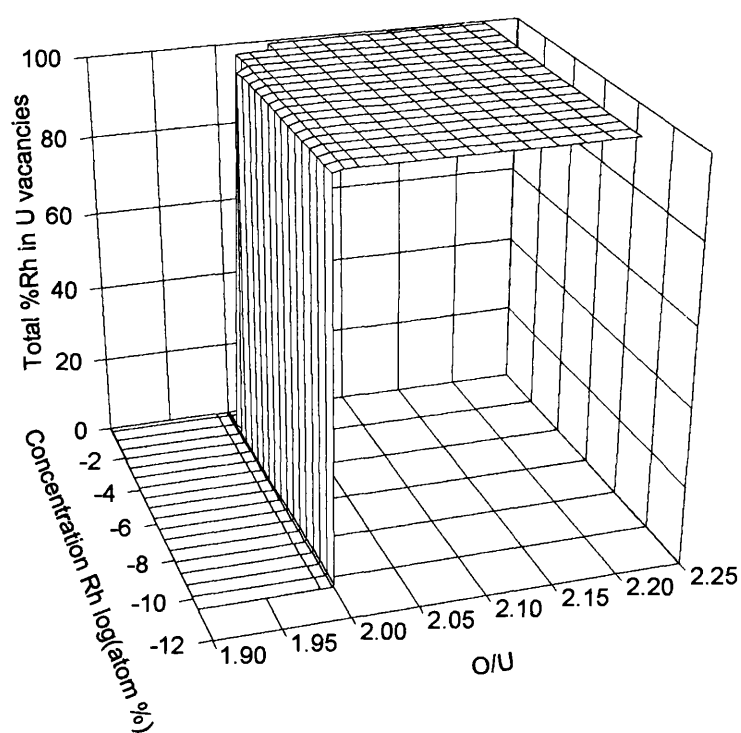
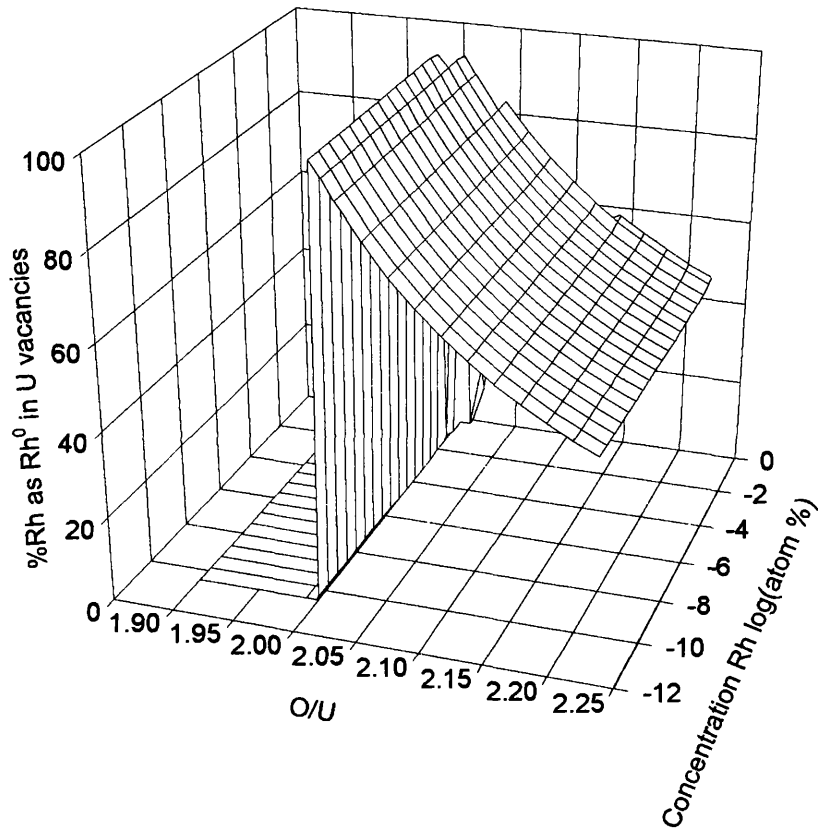


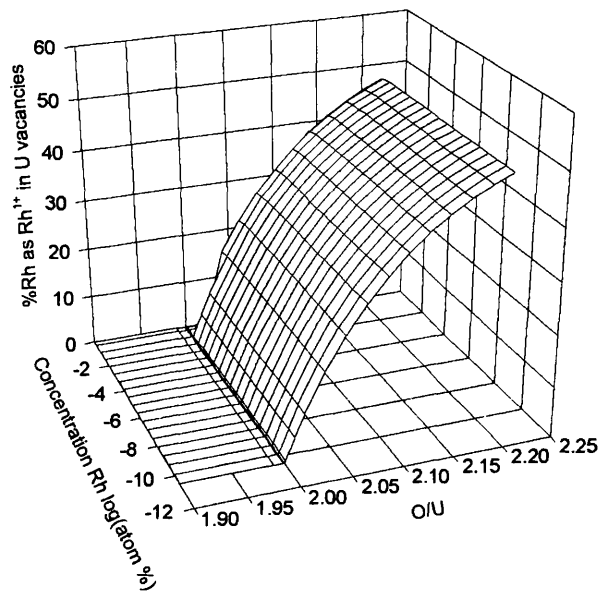
Figure 26. Proportion of single Rh atoms occupying uranium vacancy sites in urania as a function of stoichiometry and Rh concentration.

²⁴ For $O/U=2.2$ only 7% of the single atom Rh population will be in the $2+$ state. For smaller O/U ratios the percentage is reduced.

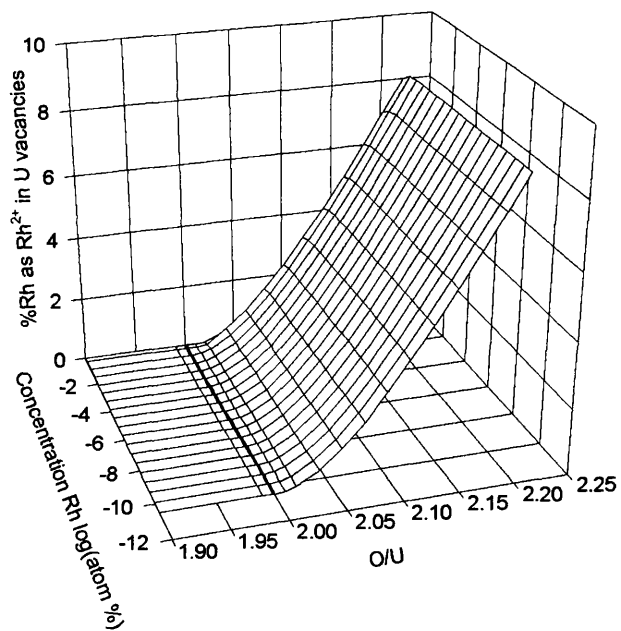


a)

Figure 27. Proportion of single Rh atoms occupying uranium vacancy sites as charged ions. a) Proportion as neutral Rh. This figure is continued overleaf



b)



c)

Figure 27 continued. b) Proportion of Rh atoms as Rh^{1+} in U vacancies. c) Proportion of Rh atoms as Rh^{2+} in U vacancies.

7.4.3 Pd

The departure from the type of behaviour shown by Mo in urania is much more radical for Pd than it is for Ru and Rh. With the latter, although there is a decreasing tendency for the fission product to ionize when in a uranium vacancy site in hyperstoichiometric urania, the pattern of changing fission product location with fuel stoichiometry is essentially the same for Ru and Rh as it is for Mo. With Pd the picture is quite different. In UO_{2-x} , rather than the trivacancy site being the location of virtually all single fission product atoms, the single oxygen vacancy becomes a major site for Pd, of importance comparable to the trivacancy. Whereas for Mo, Ru and Rh the proportion of single fission product atoms occupying trivacancies was for the most part independent of x in UO_{2-x} , the proportion of Pd atoms occupying oxygen vacancies is seen to depend very much upon the degree of non-stoichiometry, as shown in Figure 28.

As the oxygen content of UO_{2-x} is increased towards the stoichiometric composition, the drop in the proportion of Pd occupying oxygen vacancies is mirrored not only by an increase in the proportion located in trivacancy sites but also that located in divacancies, as shown in Figures 30 and 29.

The importance of the divacancy as a Pd site continues through the near stoichiometry region into the hyperstoichiometry region. In $\text{UO}_{2.2}$ for example, 42% of the single atom Pd is calculated to be located in divacancies, in contrast to the cases for Mo, Ru and Rh, where in UO_{2+x} , fission products sited at uranium vacancies were predominant.

Although the location of Pd atoms at uranium vacancies is still an important factor in UO_{2+x} (see Figure 31) in comparison with Mo, Ru and Rh, the degree of ionization of fission product atoms at these sites is much reduced. In $\text{UO}_{2.04}$ only 1.6% of the Pd is calculated to be present as Pd^{1+} and although this proportion is increased to 20.7% in $\text{UO}_{2.2}$, most of the Pd remains neutral at all stoichiometries (see Figure 32). Charge states higher than Pd^{1+} do not form.

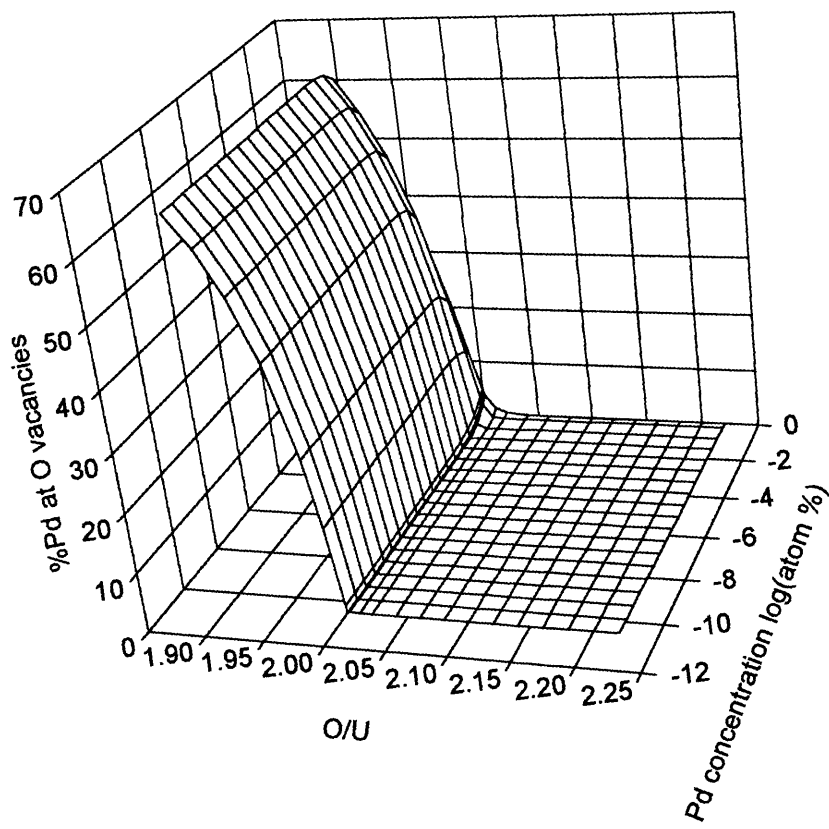


Figure 28. Proportion of single Pd atoms occupying oxygen vacancy sites in urania.

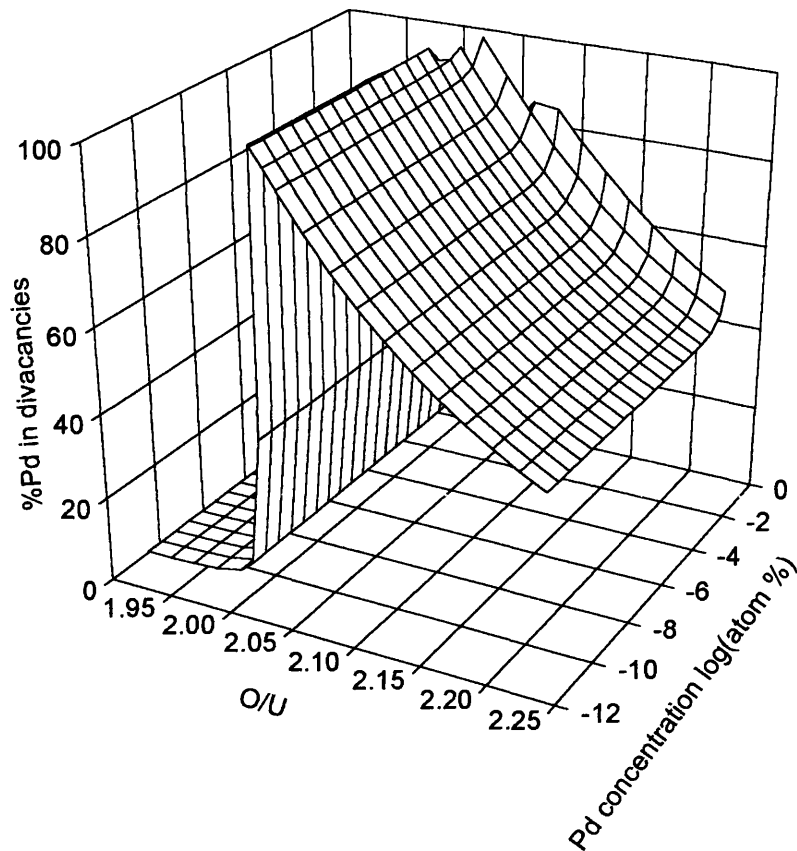


Figure 29. Proportion of single Pd atoms occupying divacancy sites in urania. Note that this population extends into the hyperstoichiometry region and, to a lesser extent, the hypostoichiometry region. This contrasts with the cases for the divacancy occupation of Ru and Rh which was restricted to the near stoichiometry region.

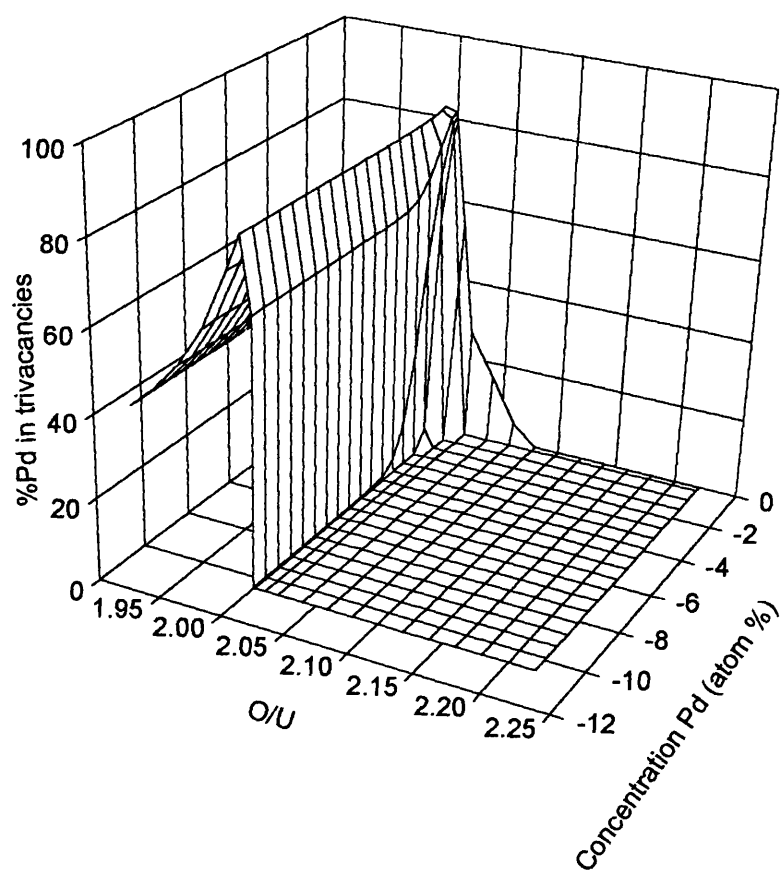


Figure 30. Proportion of single Pd atoms occupying trivacancy sites in urania.

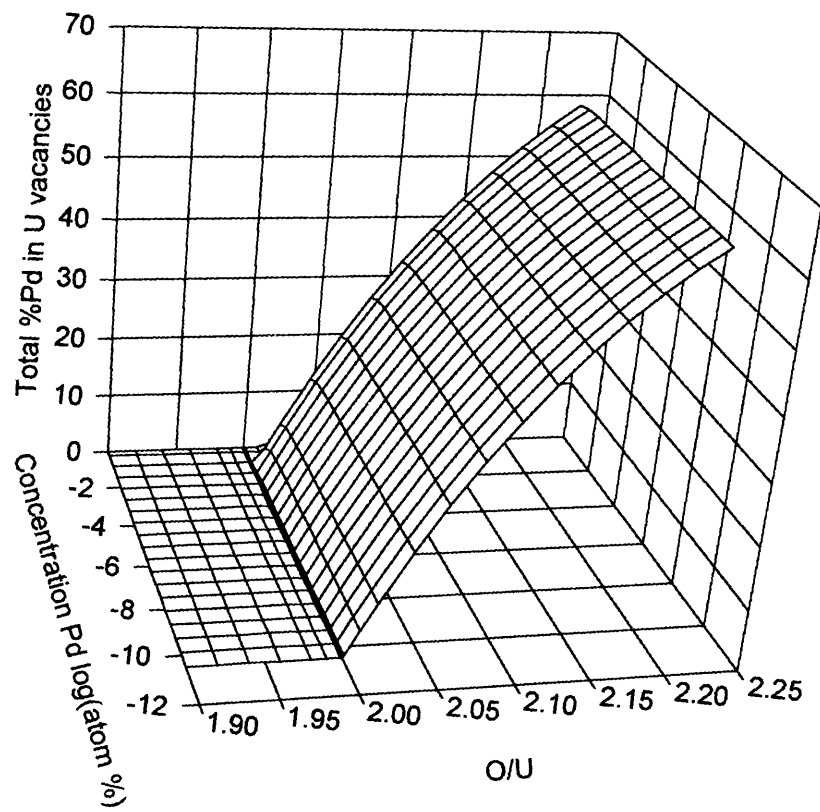
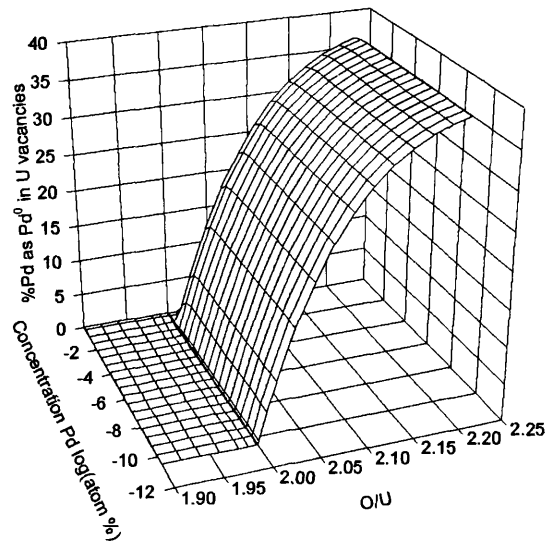
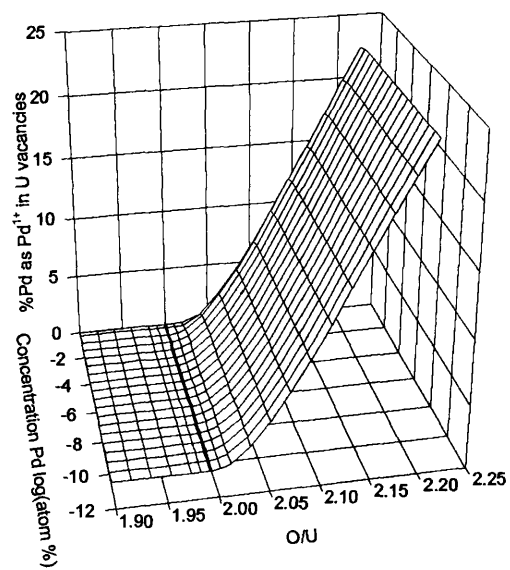


Figure 31. Proportion of single Pd atoms occupying uranium vacancy sites in urania.



a)



b)

Figure 32. Proportion of single Pd atoms occupying uranium vacancy sites as a) neutral atoms and b) Pd¹⁺.

7.5 Analysis and Discussion

In this section we discuss and analyse the results for Ru, Rh and Pd briefly outlined above.

In Chapter 6 the behaviour of Mo in urania was considered and in broad terms (ignoring the effects of high fission product concentrations) the effect of stoichiometry on the location of single Mo atoms is as follows: In UO_{2-x} Mo will be found in trivacancy sites, in UO_2 at divacancy sites and in UO_{2+x} in single uranium vacancies. Although the predicted behaviour for Pd is quite different from this, Ru and Rh exhibit close parallels with Mo.

For fission product atoms at uranium vacancy sites, the degree of ionization decreases in the order Mo-Ru-Rh-Pd, which is in line with the ionization potentials used (see Table 7). The behaviour of Pd shows us, however, that ionization potentials are not the only factor that is important in distinguishing between each of the fission products.

In UO_{2-x} occupation of oxygen vacancies by Mo was seen not to be energetically favourable. As the oxygen vacancy is of such importance in the case of Pd, it is of interest to write similar reactions for Ru, Rh and Pd and compare the energy changes involved. We consider only UO_{2-x} and hence can assume a ready supply of oxygen vacancies.



In equation 63, the movement of a fission product atom (FP) from a trivacancy site to a pre-existing oxygen vacancy is expressed in terms of a defect reaction. The energy changes involved in these processes are given for the cases of Ru, Rh and Pd²⁵. Only in

²⁵ For Mo this energy change is 0.52eV.

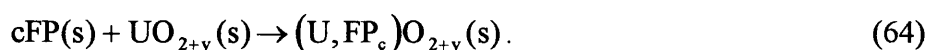
the case of Pd is this energy change negative and hence only in this case does the oxygen vacancy compete as a fission product location with the trivacancy in UO_{2-x} . This result is primarily due to a particularly low energy calculated for Pd at an oxygen vacancy (see Table 15).

In UO_{2+x} there is a general tendency for Ru and Rh to be located in uranium vacancy sites. Although this tendency is also present with Pd it is much reduced and the divacancy is found to be a site of comparable importance. This is also due to a particularly low calculated defect energy, this time for Pd at a divacancy site. The low values of the two energies, which lead to the special behaviour predicted for Pd in urania, can be traced to the electron densities used in the derivation of interionic potentials and in particular to the closed 4d shell structure of the Pd ground state, which results in a smaller atom.

As with Mo, for all three of the elements considered in this chapter the general behaviour applicable at low and medium concentrations is seen to change at certain O/U ratios at high concentrations. For example, at a fixed value of x in UO_{2+x} , at low and medium Ru concentrations the uranium vacancy may be the dominant Ru site. As the Ru concentration is increased, the divacancy and then the trivacancy site become, in turn, the most important. This type of behaviour occurs where the most populous fission product location is heavily dependent upon the presence of extrinsic defects (such as oxygen interstitials or vacancies). This is the case for the uranium vacancy site important in UO_{2+x} and also the oxygen vacancy site of Pd in UO_{2-x} ; the role of the oxygen interstitial was discussed in detail in Chapter 6. These effects at high fission product concentrations are undoubtedly of some importance although for the most part they occur beyond the limits of the region where the simple statistical treatment of defects used in this thesis is wholly reliable.

As with Mo, it is of interest to plot the free energy change per fission product atom (ΔE) when a certain concentration of isolated atoms of fission product are added to urania.

This will give an indication of how “soluble” the atoms are, providing the individual fission product atoms do not interact with each other. Whenever the plotted energy change is negative then solubility of the atom is favoured and this would presumably be reflected in the experimental fission product release data, as was suggested for Mo. In practice however, a negative energy change is not a sufficient criterion for fission product solubility as the ΔE used here is with respect to isolated fission product atoms introduced into the lattice from infinity and not from the fission product metal. For solution rather than precipitation in the fuel to be favoured, it is necessary that the energy change associated with the following reaction be negative.

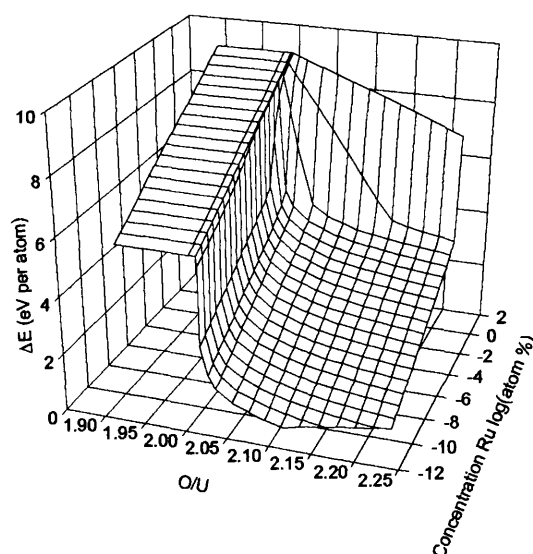


Here the fission product atom begins in the metallic state rather than at infinity. As in the previous chapter, the energy change associated with this reaction can be approximated as $\Delta E + \Delta E_{\text{sub}}$, where ΔE_{sub} is the free energy associated with the sublimation of the fission product metal. The free energy change, ΔE plots for Ru, Rh and Pd where the fission products begin at infinity are given in Figure 33 where the term “free energy” is used in the restricted sense already adopted in the case of Mo. That is, it is composed of internal energy and configurational entropy terms alone and is therefore only an approximation to the true change in free energy. Figure 33 provides an approximate value for the energy change associated with the addition to urania of fission product atoms originally in the gaseous state.

We see from Figure 33, that addition of Rh or Pd to urania always results in an increase in system energy. At no concentration or O/U ratio, do the plots for these fission products cut the $\Delta E=0$ plane. In the case of Ru, there is a small region, at very small Ru concentrations and large degrees of hyperstoichiometry, where the energy change is

negative²⁶. However, even at the most extreme of the conditions in the range considered, ΔE is much greater than -0.5eV .

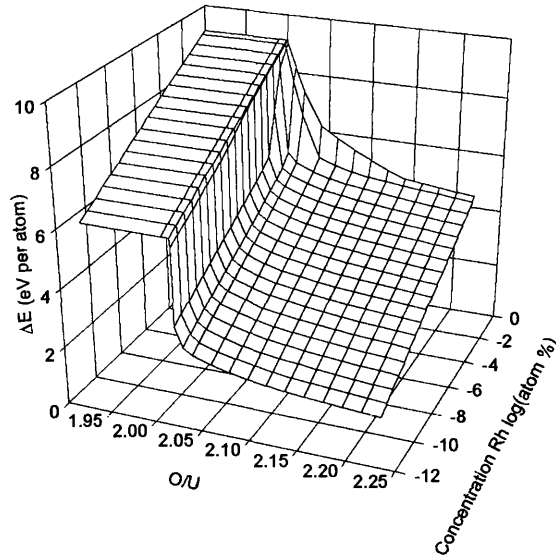
The curve traced out on the $\Delta E=0$ plane by the Ru energy surface in Figure 33 gives an indication of an upper limit to the solubility of Ru (with respect to the gas phase) in urania as a function of O/U ratio. At O/U=2.2 for example, the concentration of Ru when $\Delta E=0$ (that is the predicted solubility of Ru atoms at O/U=2.2) is less than 10^{-9} atom%. This is less than the detection limit by X-ray microanalysis [36]. Hence, the calculations presented here agree with an insoluble nature for Ru. The insolubility of Rh and Pd following from the fact that their energy plots never cross the $\Delta E=0$ plane.



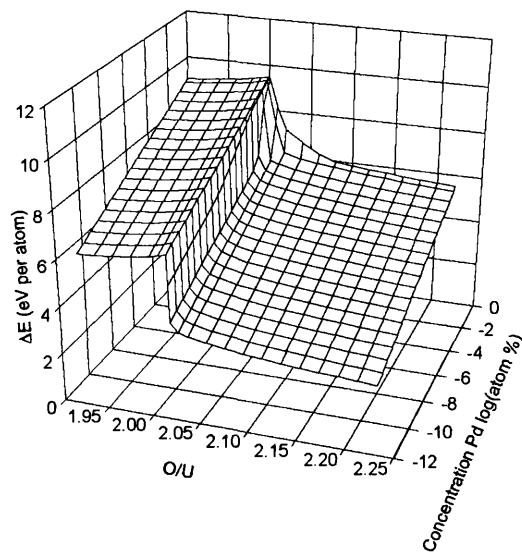
a)

Figure 33. “Free energy” change (ΔE) per atom when Ru, Rh and Pd atoms are added to urania from the gas phase, plotted as a function of fission product concentration and O/U ratio for a) Ru. Only the region $\Delta E \geq 0$ is drawn for each plot. This figure is continued overleaf.

²⁶ The plots in Figure 33 only show the range of $\Delta E > 0$ and the region where the ΔE surface cuts the $\Delta E=0$ plane can be clearly seen.



b)



c)

Figure 33 continued. Free energy change when fission product atoms are added to urania from the gas phase. b) Rh. c) Pd.

7.6 Summary

In summary, calculations show that Ru and Rh, when present as individual atoms in urania, occupy lattice sites in a similar way to Mo. They are both, however, rather more determinedly insoluble in urania than Mo and are less inclined to ionize. The behaviour of Pd is somewhat different in that occupancy of divacancy sites is not restricted to stoichiometric UO_2 alone and that the oxygen vacancy is a viable location in UO_{2-x} . Pd is also calculated to be insoluble in urania.

The calculation of insolubility for Ru, Rh and Pd in urania is of some reassurance and provides support for the predictions made regarding the location of these elements in the urania lattice. The differences in behaviour between Pd and Mo, Ru and Rh, should presumably have some effect on the values of the diffusion coefficients of these elements in urania. Exactly what form such differences should take is beyond the scope of this work but we end this chapter on a note of speculation. In Chapter 6, it was mentioned that some detailed X-ray analysis work may reveal the occurrence of zones of relatively depleted Mo and enriched Pd at the surface of some five metal particles [57]. Whilst no published record of this has been made and it must therefore be treated with some caution, if such zones do exist, it is conceivable that they may have an origin in the kind of atomic behaviour outlined above. The effect of such zones upon the possible oxygen potential buffering effect of Mo would be of interest.

8 Sr and Ba

8.1 Introduction

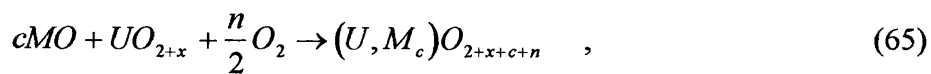
In this short chapter, our primary aim is to attempt an investigation into the reliability of the simple model for fission product solubility that was outlined in Chapter 2 and employed, for the case of Mo, in Chapter 6. We use as a vehicle for this study the alkali earths Sr and Ba and their calculated behaviour in UO_2 . According to Kleykamp's recent review of fission product solubilities [38], in near stoichiometric urania the maximum solubilities for Sr and Ba are fairly modest and low respectively. It is the presence of this difference in solubility and their similar chemical natures that make Sr and Ba of particular interest for our purposes.

In addition to any factors affecting the accuracy of the calculated defect energies (such as the quality of interaction potentials, the absence of vibrational entropy terms or the suitability of applying the ionic model for example) there are three main points which will limit the value of solubility calculations as a tool for quantitative prediction;

- a) The simple statistical model used, as outlined in Chapter 2, contains no modification to the configurational entropy to account for site blocking effects and no defect interaction terms are introduced (either explicitly or as an activity coefficient). This means the model would be expected to be inaccurate at high defect concentrations.
- b) Calculated and experimental fission product behaviour and UO_2 properties near stoichiometric composition are extremely sensitive to the oxygen potential and O/M ratio. When comparing calculated and experimental results it is not always clear whether the physical systems are comparable or not.
- c) Our simple model calculates defect concentrations and system energies for a *closed* model system. Again this makes it difficult to compare results with experiment.

In the current context, the first point means that, in attempting to calculate maximum solubilities, we shall be pushing our model to the limits of its legitimate applicability and, at least in the case of Sr, possibly beyond it. It will, however, be of interest to examine the results of the attempt.

In Chapter 6 we considered the relation between Mo in solution in urania and Mo in metal precipitates. For each calculation of defect concentrations, the oxygen content of the system was assumed fixed (a closed system was assumed) and providing the concentration of Mo in solution was low, the approximate O/Metal ratio of the model system remained fixed too. From the start in this chapter however, we wish to compare calculation with experiments in which oxides of Sr and Ba are mixed with urania. If some Sr or Ba is soluble in the urania matrix then we must account for the accompanying oxygen. The ideal way to do this is to work in terms of the oxygen potential but this is currently problematic from a computer simulation perspective. Alternatively, the reaction,



where M = Sr or Ba, can be investigated for a *closed* system with certain fixed values for c, n and x (here, n and x may take both positive and negative values). It should be noted however, that the assumption that MO is the important oxide phase is often incorrect (the presence of perovskite structured oxides in real fuels was mentioned in Chapter 4) and further quantitative errors are introduced by the uncertainties in the values for the lattice enthalpies of the oxides and the electron affinities of oxygen. However, to keep the problem manageable, this approach shall be adopted here. We want to know if our solubility calculations on Mo in Chapter 6 may be broadly reasonable and hence in this chapter a certain amount of approximation is allowable.

8.2 The Behaviour of Sr and Ba in UO_{2+x}

Although there is some overlap in the observed behaviour of Sr and Ba in irradiated reactor fuels, in the sense that both can occur in oxide precipitates (grey phases) in UO_2 and mixed fuels, the observed tendency is for Ba to form oxide precipitates whilst Sr is soluble in the matrix [36]. In irradiated fuels, the yields of Sr and Ba are roughly comparable to those of Rh and Pd. In Kleykamp's recent review of fission product solubilities [38], the maximum solubility of Sr in near stoichiometric UO_2 is quoted as 12 mol% at 1773 K and an oxygen potential of -460 kJmol^{-1} and that of Ba as 0.58 mol% at 2273 K and an oxygen potential of -370 kJmol^{-1} .

Defect energies for Sr and Ba in urania have also been calculated by Grimes and Catlow in their general study of some important fission products using electron gas potentials [10]. They found the uranium vacancy to be a favoured site for Sr and Ba in both UO_2 and UO_{2+x} whilst in UO_{2-x} the divacancy, and perhaps the trivacancy, were favoured.

In principle, it should be possible to produce a good set of interaction potentials for this study using empirical methods. However, as one of the purposes of this chapter is to investigate the reliability of our solubility calculations on Mo, the same method for deriving potentials shall be used that has been employed throughout the foregoing part of the thesis, that is, the "empiricising" of electron gas potentials using the empirical potentials of Jackson and co-workers [42] as outlined in Chapter 3. The short range potentials thus derived are given in Table 16.

Interaction	A (eV)	ρ (Å)	C_6 (eVÅ ⁶)
Sr ²⁺ -O ²⁻	586.4	0.4269	29.98
Sr ²⁺ -U ⁴⁺	5867.0	0.3095	25.06
Ba ²⁺ -O ²⁻	589.1	0.4440	44.66
Ba ²⁺ -U ⁴⁺	7374.0	0.3187	36.60

Table 16. Short range potentials for Sr and Ba interactions. Shell model parameters are $Y=7.3$ and $k=849.1 \text{ eVÅ}^{-2}$ and $Y=7.9$ and $k=622.8 \text{ eVÅ}^{-2}$ for Sr and Ba respectively.

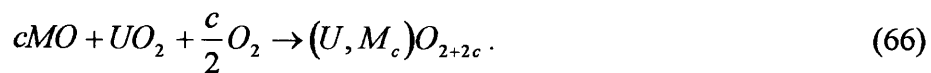
Using these potentials in CASCADE calculations of defect energies enables the investigation of Sr and Ba site preferences in urania as a function of stoichiometry. The calculated defect energies are given in Table 17. To illustrate these site preferences, in Figure 34 we plot the proportion of Sr and Ba at the various important sites in $\text{UO}_{2\pm x}$ with change in value of x . For both Sr and Ba the concentration has been fixed at one particular value (1×10^{-7} atoms per UO_2 molecule).

It can be seen that the results presented in Figure 34 are consistent with the previous calculations of Grimes and Catlow [10]. In UO_2 and UO_{2+x} the uranium vacancy site is preferred whilst in UO_{2-x} the divacancy is the predominant site with some Sr/Ba also present in trivacancies.

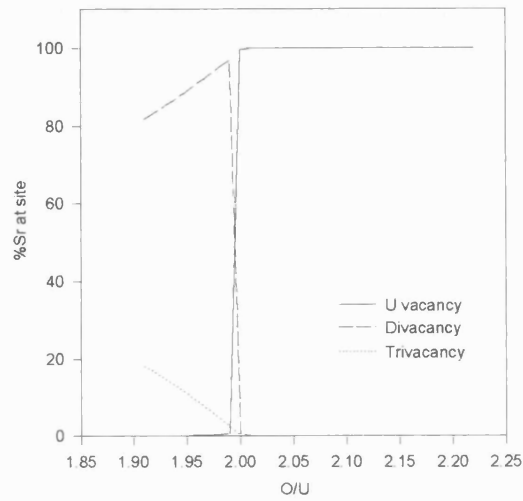
Fission product site	Sr	Ba
U vacancy	58.70	61.19
divacancy	74.54	76.87
trivacancy	91.44	93.56
tetravacancy	169.51	170.82
interstitial	-5.82	-1.74

Table 17. Calculated defect energies for single atoms of Sr and Ba at various sites in UO₂. Values are in eV.

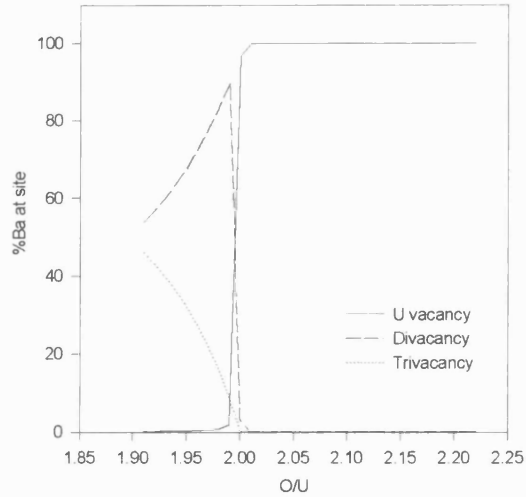
The calculated system energy (that is the energy of the (Sr/Ba)/UO₂ closed model system containing single Sr/Ba atoms) can now be used to estimate the *maximum* solubility of the fission products in UO₂. Matters are simplified by assuming the fission product oxide is mixed with, initially pure, stoichiometric UO₂ in such a way that the O/M ratio is maintained²⁷ at 2.0 (here M=U+(Sr/Ba)). This constraint is reasonably consistent with the experiments used to derive the experimental solubilities quoted above and implies that, in equation 65, x=0 and n=c. Hence,



²⁷ It should be remembered that a constant O/M ratio does not necessarily imply a constant oxygen potential.



a)



b)

Figure 34. Plot of calculated site preference of a) Sr at 1773 K and b) Ba at 2273 K, as a function of O/U ratio. In each case the respective fission product concentration is 1×10^{-7} atoms per UO_2 molecule.

This is, admittedly, a simple approximation but it is in the same spirit as that used in Chapter 6 when estimating Mo solubility, and it is the reliability of that calculation that we wish to investigate.

Using equation 66 and tabulated values for lattice enthalpies and electron affinities of oxygen etc. (see Table 18) the energy change, ΔE , associated with this reaction can be estimated. A plot can then be made of the change in energy per fission product atom, $\Delta E/c$, required to complete the solution reaction in equation 66 against fission product concentration. This plot is shown in Figure 35.

Process	Energy (eV)
$\text{SrO(s)} \rightarrow \text{Sr}^{2+}(\text{g}) + \text{O}^{2-}(\text{g})$	34.0
$\text{BaO(s)} \rightarrow \text{Ba}^{2+}(\text{g}) + \text{O}^{2-}(\text{g})$	32.3
$\frac{1}{2}\text{O}_2(\text{g}) \rightarrow \text{O}^{2-}(\text{g}) + 2\text{e}^-$	9.69

Table 18. Some energy values of processes required in equation 65. The values are for T=298K and are used as an approximation only. Source: [65].

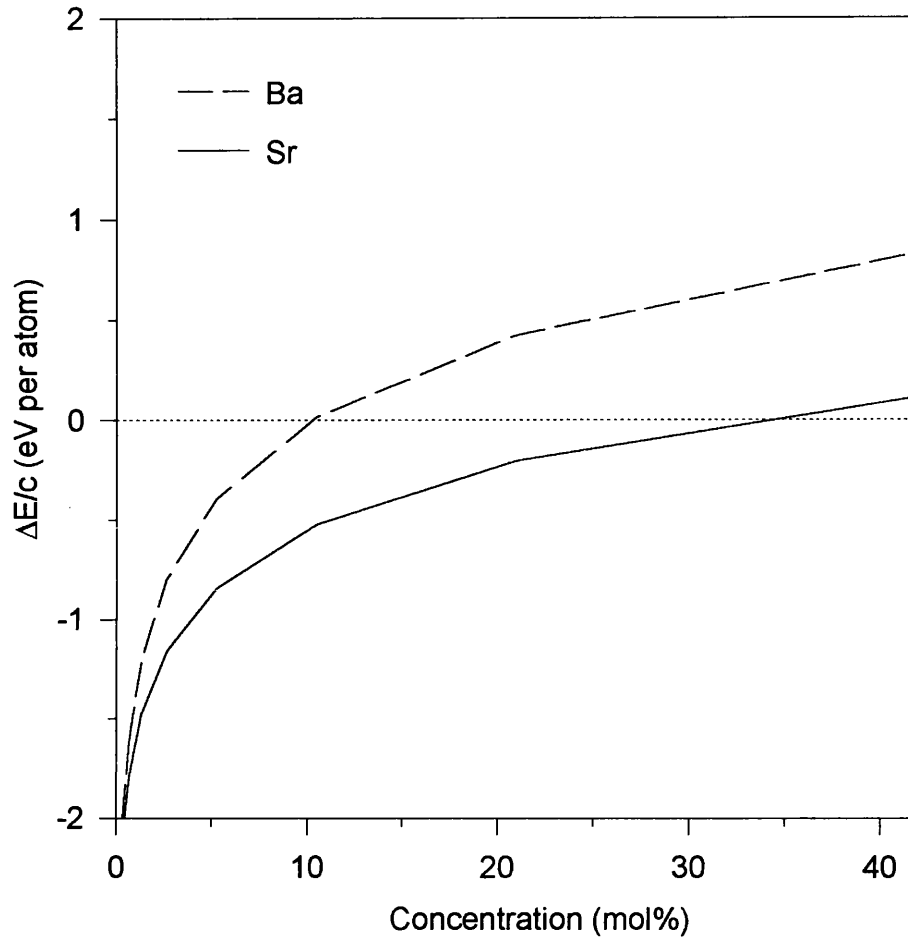


Figure 35. Plot of energy change in system when a concentration of Sr/Ba is dissolved in UO_2 according to equation 66. The maximum solubility corresponds to an energy change of zero and can be read of from the concentration axis. In this case, the maximum solubility is about 35 mol% for Sr and 10 mol% for Ba.

In Figure 35, the point in the plot where $\Delta E/c=0$ corresponds to the maximum solubility of the respective fission product. Clearly these solubilities (approximately 35 mol% and 10 mol% for Sr and Ba respectively) are much too high. More importantly, however, it can be seen that quite small changes in $\Delta E/c$ are seen to lead to large variations in concentration. The model appears therefore, extremely sensitive to the values used for lattice enthalpies etc. (we have used as an estimate enthalpy values at 298 K, the relevant free energies will differ somewhat from these but the result given here are not thought to be qualitatively altered). Perhaps the most reassuring thing that can be said from Figure 35, is that the model does at least show Sr to be more soluble than Ba, although the difference in solubility is perhaps not as large as one might have hoped. Clearly then, the model as it stands does not allow a simple quantitative prediction of maximum solubilities. Part of the problem is no doubt due to the high defect concentrations involved and the difficulty in setting up a model closed system of close enough resemblance to the real open system of experiment. Generally, the model is very sensitive to small changes in parameters whose values are often not known to great enough accuracy.

If it is not possible to specify system parameters precisely enough to make an accurate quantitative calculation of solubility, is it at least possible to check whether the model is consistent with experiment? One way to attempt this is to fix the Sr and Ba concentrations at the respective experimentally determined value for the maximum solubility (12 and 0.58 mol% respectively) and allow the value of n in equation 65 to vary (we shall still assume $x=0$). In this case the final O/M ratio is allowed to vary from the value 2.0 and again a search is made for the conditions (in this case the final O/M ratio) that give an energy change $\Delta E/c=0$ in equation 65. If, however, this variation in O/M is much smaller than that which could reasonably be expected to be measurable in experimental work, then it can be said that the closed model system is consistent with experiment and that if accurate experimental parameters were available the computation

might provide a means for calculating maximum solubilities in reasonable agreement with experiment. For the moderately and highly soluble elements, it would be unlikely that such calculations could be followed through with such a simple model as that presented here but the method may be of use for “order of magnitude” calculations on fission products exhibiting low solubilities. Mo is just such a case, where the solubility is lower than that which can be detected by normal experimental means but is high enough, and therefore important enough, to effect Mo diffusion data when present in low doses in UO_2 (see Chapter 6).

With the above remarks in mind, Figure 36 presents a plot of $\Delta E/c$ against final O/M ratio for equation 65 with $x=0$, c =maximum solubility and n as a free variable.

It can be seen from Figure 36, that a maximum solubility of 0.58 mol% for Ba is consistent with a final O/M ratio very close to 2 (the value is 1.998) so it may be that our attempt to directly calculate a Ba solubility failed due to a lack of an accurate knowledge of experimental parameters such as the final O/M ratio of the $(\text{U}_{1-c}, \text{Ba}_c)\text{O}_{2+x}$ system. The same argument however, can not be used in the case of Sr where the final O/M ratio is calculated as 1.990; a measurable degree of hypostoichiometry.

We have already given several reason why the simple model used in this thesis is really inapplicable at high defect concentrations. The discrepancies between our Sr solubility calculations and experiment may be a manifestation of these inadequacies of the model. The lower solubility of Ba however, enables a calculation which is consistent with experiment. Although the attempt to directly calculate a maximum solubility for Ba was not a success, this may, in part, have been due to the sensitivity of the model to factors such as the final O/M ratio. Perhaps a future model, based on a calculation of oxygen potentials rather than closed constrained systems would be more successful in this respect. In some ways however, when the simple nature of the model is taken into account the results of the solubility calculations are perhaps better than we might have expected. The calculated solubilities are about the right order of magnitude. This should

provide some support to the conclusion of Chapter 6, where it was suggested that, in agreement with experiment, Mo was essentially insoluble (in the sense of most practical measurements) but the solubility was still high enough to effect the results of Mo diffusion studies at low Mo doses.

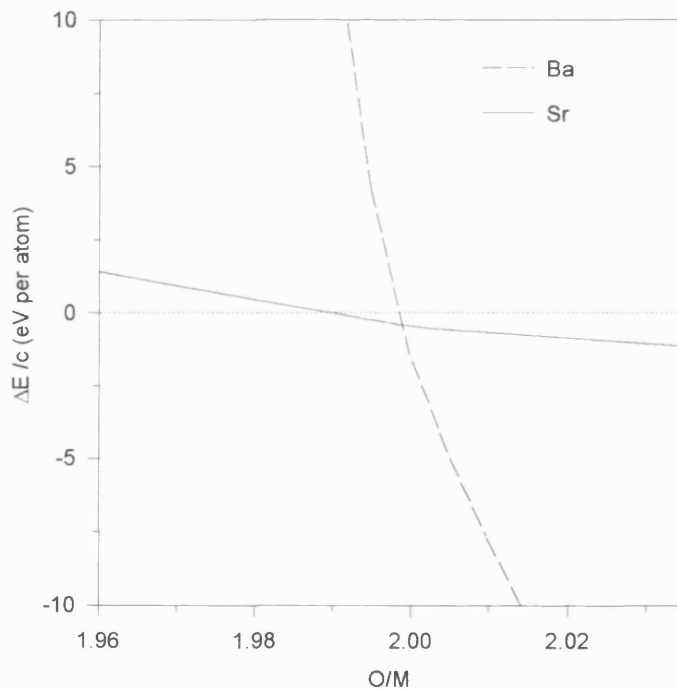


Figure 36. Plot of $\Delta E/c$ for equation 65 with $x=0$, c =relevant experimental maximum solubility and n as a free variable. The plot for Ba cuts the line $\Delta E/c=0$ very close to $O/M=2$ and the calculation is thus consistent with experiment. The plot for Sr however, cuts $\Delta E/c=0$ at $O/M=1.99$ and is thus in poorer agreement with experiment. Note however the shallower slope on the Sr plot. The slope is an inverse function of the imposed concentration.

PART 3
— DOPANTS IN
TRANSITION METAL OXIDES

9 Introduction

A considerable amount of experimental and theoretical work has been published concerning the nature of point defects in the non-stoichiometric transition metal oxides $Mn_{1-x}O$, $Fe_{1-x}O$, $Co_{1-x}O$ and $Ni_{1-x}O$ (for an overview of the experimental work see [66]). However, few studies have investigated the role of dopant impurities in the defect structure of these materials. Since the industrial grade oxides may contain as much as 1% of impurities, an examination of the effects of dopants is clearly important.

In Part 3 of this thesis, results of an atomistic simulation study of these oxides and the effect of dopants on their defect structures are presented. Although the statistical mechanical treatment described in Chapter 2 is not adopted when analysing these results, the defect energies themselves provide an indication of the effect of certain dopant ions on the point defect structure of these materials. The results presented here are intended to supplement the more extensive calculations on the undoped oxides by Catlow and co-workers [4,67,68], Tomlinson and co-workers [69,70] and Muxworthy [71].

9.1 The Transition Metal Oxides

The transition metal oxides considered here are all semiconductors adopting the rock-salt structure shown in Figure 37. Each of the oxides may exhibit some degree of non-stoichiometry and, in the case of $Mn_{1-x}O$ and $Fe_{1-x}O$, the departure from the stoichiometric composition may be large. This non-stoichiometry appears as a deficiency of cations with a minimal disruption of the oxygen sub-lattice [66]. Many properties, such as rates of diffusion and electrical conductivity, depend heavily on the defect structure of these materials and hence it is important to understand in what ways the non-stoichiometry is accommodated within the lattice. As the degree of

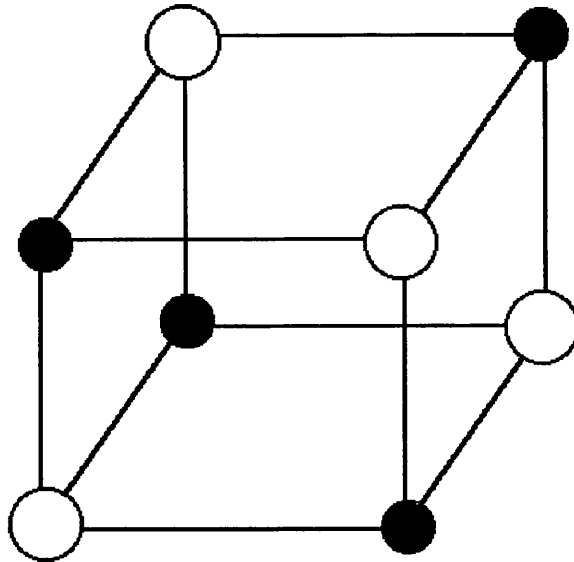


Figure 37. The rock salt structure. White circles indicate anions, black circles are cations.

non-stoichiometry may be large, we can expect there to be considerable interaction and, possibly, intimate association of point defects.

As, in the oxides considered here, the interstitial site shown in Figure 37 is much smaller than that for the fluorite structured UO_2 , oxygen interstitials play no great role in the defect structure of Mn_{1-x}O , Fe_{1-x}O , Co_{1-x}O and Ni_{1-x}O . The Schottky energy is also prohibitively high. The extrinsic, composition controlled, defect population needs therefore, to be accommodated through the production of vacancies on the cation

sub-lattice. At small departures from the stoichiometric composition a simple model of isolated cation vacancies, perhaps with an associated charge (relative to the lattice) probably provides a good description of the point defect structure of these materials. As the degree of non-stoichiometry is increased however, the aggregation of defects into defect clusters becomes a possibility (c.f. the clustering of point defects in UO_2 discussed in Chapter 4).

In Fe_{1-x}O x may attain values as high as 0.15. In fact FeO of stoichiometric composition is unstable. In highly non-stoichiometric Fe_{1-x}O samples, X-ray and neutron diffraction techniques have established not only that clustering of defects occurs but also that a population of cation interstitials is present [72,73]. It has further been suggested, on the basis of electron microscopy studies, that there is some long range ordering of defect clusters resulting in the presence of two sub-phases [74]. The most puzzling feature of the diffraction studies, the presence of cation interstitials in grossly cation deficient materials, found an explanation in the theoretical work of Catlow and Fender [4]. These authors demonstrated the stability of clusters of defects based on the {4:1} cluster where a cation interstitial is surrounded by 4 vacancies on the cation sub-lattice (Figure 38). They found that such clusters are essentially stabilised by the Coulomb interaction between the vacancies and interstitial cations.

The {4:1} cluster was suggested by these authors as the simplest of a family of related clusters. It was suggested that more complex aggregates could be formed by {4:1} clusters sharing vacancies at common edges and corners. The sharing of vacancies between the {4:1} building blocks in these larger clusters clearly results in a decrease in the vacancy/interstitial ratio associated with the cluster. This is entirely consistent with the evidence from neutron diffraction work [73] which found that the vacancy/interstitial ratio in Fe_{1-x}O decreases from about 4 with increasing value of x .

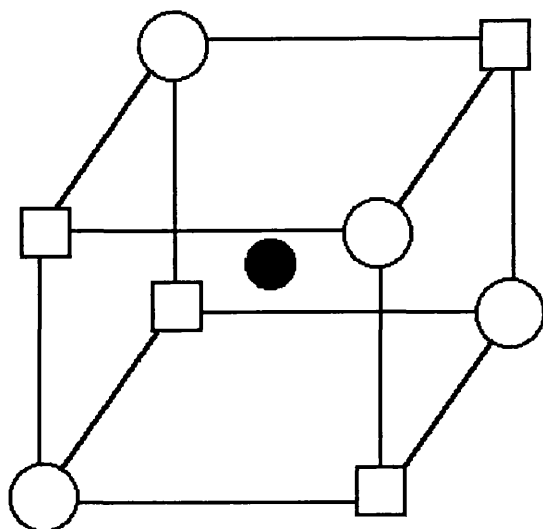


Figure 38. Schematic of the {4:1} cluster. A tetrahedrally co-ordinated cation (black circle) is surrounded by four vacancies on the cation sub-lattice (white squares). White circles indicate lattice oxygen atoms.

The evidence for the clustering of defects in Co_{1-x}O is much less certain than that for Fe_{1-x}O and the nature of the defect structure of this material is still a matter of debate. However, on the basis of simulation studies, Tomlinson has suggested that the degree of non-stoichiometry ($x < 0.01$) is such that we may expect to see the onset of clustering [69]; while Gesmundo and co-workers [75] and Petot-Ervas and co-workers [76] have used electrical conductivity data to lend support to {4:1} cluster formation at high partial

pressures of oxygen in pure Co_{1-x}O . Although Gesmundo and co-workers have further suggested that cluster formation is enhanced in the presence of Cr, their suggestion that Cr ions may occupy interstitial sites is not favoured by the strong octahedral site preference of the Cr^{3+} ion.

With $x < 0.001$, the maximum possible departure from the stoichiometric composition for Ni_{1-x}O is considerably smaller than that seen in the other transition metal oxides and hence from an entropic point of view, defect clustering is much less likely to occur. Indeed, the sum result of the diffusivity, electrical conductivity and composition vs. oxygen activity data from experiment is that isolated, singly and doubly charged Ni vacancies are the only important atomic defects in this material [77].

In Mn_{1-x}O the maximum degree of non-stoichiometry is of the same order of magnitude as that found in Fe_{1-x}O where, as we have already mentioned, large defect clusters are known to be present. Diffraction studies, similar to those carried out on Fe_{1-x}O , indicate some occupation of interstitial sites at high degrees of non-stoichiometry but experimental evidence concerning the nature of any clustering is inconclusive [78,79,80]. As pointed out by Catlow, however, it would be surprising if clustering of defect were not a factor in Mn_{1-x}O for large departures from stoichiometry (see discussion at the end of [78]). Dieckmann has suggested that neutral clusters cannot account for his data on composition vs. oxygen activity but he could not rule out the possibility of charged defect clusters [78].

10 Methods

In the following chapter we report the results of atomistic computer simulation studies of the transition metal oxides obtained using the techniques outlined in Chapter 3. The use of these oxides as model systems in computational work is facilitated by a large base of experimental data. However, these materials do present some specific difficulties in simulation studies. For example, it is not clear to what extent covalency is important and whether such effects can be adequately accommodated within the effective pair potential model. Nevertheless, through the use of empirical potentials, calculations have, in the past, been successful on these materials (see for example [67,68]). Another difficulty is presented by the presence and possible importance of crystal field effects on the electronic structure of the transition metal ions [81,82]. As discussed below, at times these terms may be important in determining whether a particular defect cluster configuration is energetically favourable.

As an alternative approach to the classical simulation studies reported here, Grimes and co-workers [83] have carried out molecular-orbital type calculations on the doped transition metal oxides to investigate the electronic contribution to the stability of defect clusters. Their calculations suggest that, in some cases, dopant cations located at the interstitial position, may appreciably effect the stability of {4:1} clusters. In particular {4:1} clusters based on Mn^{3+} and Fe^{3+} interstitials in Co_{1-x}O and Ni_{1-x}O were found to be more stable than the undoped clusters in these materials.

10.1 Interionic Potentials

In the present study of the defect structure of the transition metal oxides, we again use a pair potential model with interactions of the Buckingham form (equation 39). Initially an attempt was made to derive all these interaction using the electron gas method (see

Chapter 3). A simple application of this method to the problem, using electron densities derived from tabulated or calculated wave functions appropriate to free ions, results in a calculation of perfect crystal properties in extremely poor agreement with experiment. Improvements in the model are obtained if the wave functions (and hence densities) are re-calculated for the ion embedded in a potential well simulating the Madelung field experienced in the crystal by the ion. Even in this case, however, calculated crystal properties show the potentials to be much inferior to equivalent empirically derived potentials. An attempt could be made to change, in an *ad hoc* fashion, one or more of the parameters describing the potentials in order that the calculated crystal properties are improved. Such potentials, however, must then be considered highly questionable and it is unlikely they would provide any advance on carefully derived empirical potentials.

10.1.1 Potentials for M^{2+} - O^{2-} and O^{2-} - O^{2-} interactions

The problems found when attempting to apply directly electron gas methods to the current study may well, in part, be indicating an appreciable covalent character to the M-O bonding in these materials. Although the present calculations essentially assume the validity of applying the ionic model in this study, a good set of empirically derived potentials will implicitly contain some contribution accounting, in an approximate way, for the non-ionic interactions.

In their original work on the transition metal oxides, Catlow and co-workers [67] empirically derived short range potentials for the M^{2+} - O^{2-} interaction of the oxides considered here on the basis of a fitting to the experimental data on cohesive energies and dielectric constants. The short range component of the O^{2-} - O^{2-} interaction was fixed at that calculated for O^1 - O^1 by a Hartree-Fock calculation. The assumption here was that as the two O^{2-} ions approached each other, the highly polarizable second electron on

each ion would be repelled resulting in a short range interaction very similar to that between two O^{1-} ions.

Due to the problems experienced when attempting to apply the electron gas method and in view of the fact that their empirical potentials have been employed in several studies of the transition metal oxides in the past (see [69,70]) it was decided to employ the potentials of Catlow and co-workers in the current work. The only exception to this was in the case of the $Mn^{2+}-O^{2-}$ interaction, where the calculated crystal properties were in poorest agreement with experiment. Here the A and ρ parameters of the original interaction were further adjusted to improve the fitting. The resulting potentials are given in Table 19. All cation-cation short range interactions were assumed to be negligible.

Interaction	A (eV)	ρ (Å)	C_6 (eV Å ⁶)
$O^{2-}-O^{2-}$	22764.3	0.149	20.37
$Mn^{2+}-O^{2-}$	590.0	0.3591	-
$Fe^{2+}-O^{2-}$	745.3	0.3362	-
$Co^{2+}-O^{2-}$	793.2	0.3296	-
$Ni^{2+}-O^{2-}$	863.4	0.3186	-

Table 19. Short range interactions for the transition metal oxides. All potentials are those given in [67] with the exception of the $Mn^{2+}-O^{2-}$ interaction which has been derived empirically in the present work. A potential cut-off of 2.1 lattice units was used for all the calculations reported in this chapter.

Crystal	k (eVÅ ⁻²)	Y (e)
MnO	6.53	-2.0066
FeO	5.48	-2.0066
CoO	4.81	-2.0066
NiO	4.26	-2.0066

Table 20. Shell model parameters for the O²⁻ ion in the transition metal oxides. Shells where not included on cations. All values are taken from [67] with the exception of the parameters in MnO.

In keeping with the original potentials of Catlow and co-workers, the shell model has been invoked only in the case of the O²⁻ ion. However, the value of the polarizability is allowed to depend on the particular host crystal environment by varying the force constant k in equation 43 (the electron number Y remains fixed). Shell model parameters are given in Table 20.

It will be noticed from Table 19 that no attempt has been made to include a C_6 term to explicitly account for the Van der Waals component in the M²⁺-O²⁻ interactions. However, the process of empirically deriving the parameters in the table means that some allowance for the longer range dispersive interactions (as well as covalency) should be included in the potentials.

	MnO	FeO	CoO	NiO
E_{lattice} (eV)	-38.06 (-39.5)	-39.42 (-40.7)	-39.91 (-41.4)	-40.94 (-42.3)
r_{lattice} (Å)	2.222 (2.222)	2.160 (2.155)	2.137 (2.133)	2.087 (2.084)
ϵ_0	17.9 (12.8-18.0)	13.1 (12.7-14.2)	12.3 (10.0-12.9)	11.4 (9.7-11.9)
ϵ_∞	4.95 (4.95)	5.32 (-)	5.66 (5.3)	6.00 (-)
c_{11} (10^{11} dyne/cm ²)	19.53 (22.3)	25.09 (35.9)	27.04 (25.6)	30.86 (27.0)
c_{12} (10^{11} dyne/cm ²)	13.86 (12.0)	15.32 (15.6)	15.93 (14.4)	17.38 (12.5)
c_{44} (10^{11} dyne/cm ²)	13.86 (7.9)	15.32 (5.6)	15.93 (8.0)	17.38 (10.5)

Table 21. Perfect crystal properties for the transition metal oxides calculated using the short range potentials from Table 19. References to the experimental values shown in brackets are given in [67,25].

The perfect crystal properties calculated using the potentials of Table 19 are given in Table 21. We can see from this table that our new potential for MnO reproduces quite well the perfect crystal properties (there is however some question over the experimental value of the static dielectric constant ϵ_0 , we have fitted to $\epsilon_0=18.0$).

A remark should be made concerning the calculated values of the elastic constants reported in Table 21. In a rock salt structured crystal, with ions interacting through central force pair potentials, the elastic constants c_{12} and c_{14} are necessarily related by the Cauchy relation [84],

$$c_{12} = c_{44}. \quad (67)$$

This condition holds in our simulation work on the transition metal oxides and accounts for the calculated equality between c_{12} and c_{44} shown in Table 21. To account for the violation of the Cauchy relation found in the experimentally determined elastic constants given in the table, a more sophisticated treatment, which included some allowance for many-body interactions, would be required.

10.1.2 Potentials for M^{3+} - O^{2-} interactions

In their original work, for the short range interactions of the M^{3+} ions with O^{2-} , Catlow and co-workers used their potentials for the equivalent M^{2+} - O^{2-} interaction. In the current work however, we derive these potentials using a similar approach to that adopted in our work on UO_2 in Part 2 of the thesis. That is, we use the empiricising method described in Chapter 3, whereby electron gas derived potentials are used to modify the M^{2+} - O^{2-} interaction giving a more realistic potential for the M^{3+} - O^{2-} interaction. In this approach, before deriving the electron gas potentials, the electron density of the O^{2-} ion was re-calculated to allow for the influence of an idealised Madelung type potential appropriate to the particular crystal. The empiricised potentials thus derived are given in Table 22.

Interaction	A (eV)	ρ (Å)	C_6 (eV Å ⁶)
Mn ³⁺ -O ²⁻	640.3	0.3488	-
Fe ³⁺ -O ²⁻	815.7	0.3263	-
Co ³⁺ -O ²⁻	827.2	0.3232	-
Ni ³⁺ -O ²⁻	922.9	0.3108	-

Table 22. M³⁺-O²⁻ short range interactions derived using the empiricising method described in Chapter 3.

10.2 Crystal Field Effects

When considering the perfect lattice, the effect that the rest of the crystal has on a particular lattice ion is included through our use of empirical potentials. In the derivation of the M³⁺-O²⁻ interaction we also tried to include some of the influence the crystal has on the O²⁻ ion when deriving the empiricised potentials. However, there is one aspect of the crystal field that has been overlooked concerning the electron density of the transition metal ions at non-lattice sites and of charges other than 2+.

When a transition metal ion is placed in a crystal, the d orbitals will arrange themselves in the way that is most energetically advantageous. This effect results in a splitting of the degeneracy in the d orbitals. For a transition metal ion at an octahedrally co-ordinated site for instance (as in the case of a cation in a rock salt structured transition metal oxide) three of the d orbitals (the t_{2g} orbitals) are directed between adjacent nearest neighbour

ligands (O^{2-} ions) thus lowering their associated energy (with respect to the degenerate orbitals of an ion in a spherically symmetrical field equivalent to that produced by the six co-ordinating ligands). The energy associated with the remaining two orbitals (the e_g orbitals) is, however, increased, as these orbitals are directed towards the ligands themselves. The magnitude of the splitting between the t_{2g} and e_g orbitals, $10Dq$, depends on a number of factors but McClure has shown that spectroscopic data on the transition metal ions in aqueous solution appear to give a reasonable estimate of the value appropriate in a crystal environment [82]. This splitting of the d orbitals leads to an extra stability for the metal ion at the octahedral lattice sites, and we would thus expect the effect of this to be included, to some extent, in the empirical potentials for the lattice ions.

For a transition metal ion in a tetrahedral site, the four co-ordinating ligands have a somewhat different effect. In this case the four ligands approach closest to the t_{2g} orbitals and these are raised in energy whilst the e_g orbitals are lowered. However, as the ligand field for the tetrahedrally co-ordinated metal ion is less than that for the ion at an octahedral site, the $10Dq$ splitting in the tetrahedral case is much smaller.

The splitting of the d orbitals described above will have two main influences on the energies of the type of point defects considered in the following chapter. First, for a process in which a doubly charged dopant cation transfers an electron to a triply charged host cation,



it can be expected that an adjustment to the reaction energy will be needed. Secondly, we shall be considering defect clusters (the {4:1} clusters) which have a transition metal tetrahedrally co-ordinated by 4 lattice oxygens. To form such a cluster we need to move the cation from an octahedrally co-ordinated lattice site to the tetrahedral interstitial site. Again we can expect the d orbital splitting to play some role, and in fact the splitting will

generally favour the octahedral site. Ideally such effects should be included in the potentials but this would require different potentials for the interactions involving the cations at the different sites. Additionally, as the value of $10Dq$ depends to some extent on the distance between cation and ligands, it could then also be argued that different $D^{n+}-O^{2-}$ potentials would be required for the interactions in each host oxide. Such a scheme would thus significantly multiply the work involved in the calculations whilst giving uncertain benefits. We can however give an indication of the influence of the d orbital splitting on the energies associated with defect reactions. Although we do not do this in the case of the calculated energies of charge transfer reactions, an indication of the extra octahedral site preference energy in reactions involving {4:1} clusters will be given using energies derived from spectroscopic data, as discussed below.

11 Results and Discussion

We shall now summarise the results of our calculations in terms of the binding energies of various defects with respect to their component parts. We can write many possible defect reaction equations and hence it will not be possible to be exhaustive in our treatment. The primitive defect types for all the transition metal oxides considered, at low degrees of non-stoichiometry, are taken to be doubly charged cation vacancies V_M'' and electronic holes h^\bullet . The latter are assumed to be localised on either host cations M_M^\bullet or dopant cations D_M^\bullet dependent upon which is most energetically favoured in the particular oxide considered.

Using the results of our computer simulation calculations, the relative binding energies, with respect to V_M'' and h^\bullet , of singly charged and neutral cation vacancies (V_M' and V_M respectively) are calculated. Also calculated are the binding energies of two types of charged {4:1} cluster. The influence of dopant ions on all these energies will be our major concern. The dopants that are considered here are the transition metals themselves; Mn, Fe, Co and Ni.

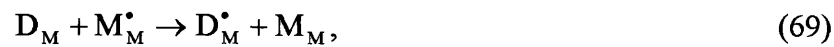
In Table 23 we state the third ionization potentials (IP) that we have used in these calculations together with estimates, where possible, of the octahedral site preference energy of the metal ion (OSP) arising from the crystal field effect discussed above. These latter values are taken from spectroscopic work on the aqueous ions [82]. As a large part of the stability of a {4:1} cluster originates from the Coulomb attraction between the interstitial metal ion and the surrounding cation vacancies, it shall be assumed that only M^{3+} ions need be considered at the interstitial site. The values in Table 23 will be used in arriving at a final value for the change in the internal energy associated with a defect reaction, ΔE .

	3 rd Ionization Potential (eV)	OSP for M ³⁺ (eV)
Mn	33.69	1.1
Fe	30.643	0
Co	33.49	0.82
Ni	35.16	—

Table 23. Ionization potentials and octahedral site preference energy of transition metal ions. Ionization potentials are from [63]. Values for the OSP are estimates from the spectroscopic data of [82]. No OSP value was available for Ni³⁺.

11.1 The Charge State of Dopant Cations

Our first task is to decide what charge state is appropriate for the isolated dopant cations at cation lattice sites within the host oxide. Assuming that holes are localised on cations we write,



and calculate the energy change, ΔE , in taking this reaction from left to right²⁸. Here $\Delta E = \Delta U + \Delta IP$. Where ΔU is the difference in the defect formation energies calculated

²⁸Of course, hole concentrations in the oxide may be such that many (perhaps all) dopant cations will be in the 2+ state even when ΔE is favourable to the 3+ state. However, this is not a problem in the context in which the results from equation 69 are used below. Strictly speaking we use equation 69 only to decide on the *location* of holes present in our later defect reaction equations.

	Mn	Fe	Co	Ni
MnO	0.00	-3.77	-1.06	-0.21
FeO	3.72	0.00	2.71	3.58
CoO	0.99	-2.72	0.00	0.87
NiO	0.07	-3.61	-0.88	0.00

Table 24. ΔE for the formation of dopant cations in the 3+ charge state via equation 69. Each row corresponds to the particular host oxide indicated in the first column. The dopants are indicated in the column headings. The main diagonal corresponds to the undoped material. All energies are given in eV.

using the CASCADE code and $\Delta IP = (3\text{rd ionization potential of dopant cation} - 3\text{rd ionization potential of host cation})$. In this, and in all defect reactions to follow, a negative value for ΔE implies that the right hand side of the equation is favoured. We tabulate values for ΔE in Table 24.

We will use Table 24 to decide which charge state should be assumed for the isolated cations in the defect reaction equations of the following two sections. Hence, for example in MnO we assume Fe, Co and Ni may all be present in the 3+ state when not associated with other defects (providing, of course, that holes are available). This is

indicated by the negative values calculated for ΔE in these cases²⁹. Similarly, in NiO, both Fe and Co are triply charged and in CoO Fe is the only one of the dopants considered in the 3+ charge state. In FeO none of the dopants considered are in the 3+ charge state and hence we assume that any holes present will exist as Fe^{3+} .

11.2 Neutral and Singly Charged Cation Vacancies

We model a singly charged cation vacancy, V_M' , as a defect cluster consisting of a doubly charged vacancy, V_M'' , and a hole localised on a nearest neighbour dopant or host cation. Hence, for the formation of V_M' from V_M'' and D_M^\bullet , we write,



where the final change in energy, ΔE , is obtained solely from the difference in defect energies, ΔU , calculated for the right and left sides of equation 70. In equation 70 we assume that the hole is localised on a dopant cation before the V_M' is produced. As shown in Table 24, this will not always be the case. We must therefore also write an equation appropriate to V_M' formation where the isolated dopant cation begins in the 2+ state,



Here, the energy involved in the implied charge transfer between host and dopant cation, ΔIP , has also been included. This value is derived from the ionization potentials given in Table 23. We give values for ΔE associated with V_M' formation in Table 25. In each

²⁹ We assume that only one dopant is present in the oxide and hence only need to consider whether ΔE is positive or negative.

	Mn	Fe	Co	Ni
MnO	-0.48 †	-0.33 †	-0.39 †	-0.48 †
FeO	3.20 ‡	-0.39 †	2.31 ‡	3.17 ‡
CoO	0.44 ‡	-0.43 †	-0.44 †	0.46 ‡
NiO	-0.56 ‡	-0.53 †	-0.52 †	-0.48 †

Table 25. ΔE for the formation of singly charged cation vacancies via equations 70 and 71. The equation used in deriving each number is indicated in each case by † and ‡ respectively. All energies are in eV.

case, the results of the previous section are used to determine which of the two above equations should be used when calculating ΔE .

Reading the values down the main diagonal, it can be seen from Table 25 that, in all cases, V_M' in the pure undoped oxide are, on the basis of internal energy changes, more favoured than isolated uncombined V_M'' and holes. Whether or not singly charged cation vacancies form in the undoped oxides will thus depend upon the degree of non-stoichiometry and the entropy terms associated with their formation.

It can also be seen from Table 25 that in certain cases the stability of the singly charged vacancy may be enhanced by the presence of a dopant cation. For example, in NiO, Mn, Fe and Co dopants all lead to extra stability of the singly charged vacancy in this oxide. Admittedly, the extra stability obtained through the dopant is quite small and we might

expect, therefore, that crystal field terms may be important. We have not attempted to include these here.

In FeO, none of the dopants considered here are found to increase the stability of the singly charged vacancy. However, we have only considered the case where the hole is localised on the dopant ion. It may of course be possible that a D^{2+} ion could add stability to a singly charged vacancy. Again we have not considered this possibility here.

We can write equations similar to equations 70 and 71 for the case of the formation of neutral cation vacancies V_M . In this case we model V_M as a defect cluster consisting of a doubly charged cation vacancy and two holes localised at nearest neighbour cation sites, one of which may be occupied by a dopant cation. Hence we write,



and,



for the cases where the dopant cations begins in the 3+ and 2+ charge states respectively. The internal energy changes, ΔE , associated with the formation of neutral cation vacancies via these equations are summarised in Table 26. Again, which equation we use is decided upon the basis of the results given in Table 24 for the stability of D_M^\bullet in the relevant oxide.

By examining the values in the main diagonals of the tables, we see from Tables 25 and 26 that, in terms of the internal energy, neutral cation vacancies in the undoped oxides show a stability over both doubly charged and singly charged vacancies. Again, their formation in the oxide will depend on the degree of non-stoichiometry and the associated entropy terms.

	Mn	Fe	Co	Ni
MnO	-0.78 †	-0.63 †	-0.69 †	-0.78 †
FeO	3.05 ‡	-0.54 †	2.17 ‡	3.02 ‡
CoO	0.25 ‡	-0.63 †	-0.62 †	0.29 ‡
NiO	-0.78 ‡	-0.75 †	-0.73 †	-0.68 †

Table 26. ΔE for the formation of neutral cation vacancies via equations 72 and 73. The equation used in deriving each number is indicated in each case by † and ‡ respectively. All energies are in eV.

Again it can be seen that the stability of the neutral vacancy may be enhanced by the presence of dopant cations. The effect of the dopants is essentially the same as that found in the case of singly charged vacancies. In FeO, Table 26 implies that none of the dopants considered will enhance the stability of neutral vacancies. However, once more it is found that Mn, Co and Fe will all lead to a lower energy for neutral vacancy formation in NiO.

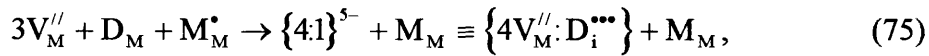
11.3 {4:1} Clusters

To investigate the stability of {4:1} defect clusters we will write equations similar to those used in the previous sections for investigating the formation of cation vacancies associated with dopant ions. The stability of the {4:1} cluster with respect to doubly charged cation vacancies and electronic holes shall be investigated. We shall assume that the interstitial site of the {4:1} clusters is taken up by a dopant cation in the 3+ oxidation state. This cation is surrounded by four doubly charged cation vacancies (see Figure 38)

giving the cluster a total charge, relative to the lattice, of 5-. This cluster is denoted by $\{4:1\}^{5-}$. In addition to investigating the stability of $\{4:1\}^{5-}$ clusters, we shall also look at the case where some of the charge on the cluster is compensated by the presence of holes localised on nearest neighbour cations. We shall investigate a high symmetry case where four charge compensating M^{3+} ions are situated adjacent to the cluster. In this case the charge is reduced to 1- and the cluster is denoted by $\{4:1\}^{1-}$. Firstly, for the formation of $\{4:1\}^{5-}$ we write,



and,



where we again decide which equation is most appropriate on the basis of the results of Table 24. To aid the comparison with the stabilities of single vacancies, we calculate the stability of the $\{4:1\}^{5-}$ clusters per isolated vacancy. That is, we calculate the energy associated with the above reactions and divide by 3. Hence, for equation 74 we write,

$$\Delta E = \Delta U/3. \quad (76a)$$

For equation 75 the charge transfer term must be included and we hence write,

$$\Delta E = 1/3(\Delta U + \Delta IP). \quad (77a)$$

To give a crude estimate of the influence of crystal field effects on $\{4:1\}$ cluster formation, the octahedral site preference energy (OSP) of the interstitial dopant ion, $D_i^{\bullet\bullet\bullet}$, can be included in the calculation. Equations 76a and 77a are then written respectively as,

$$\Delta E = 1/3(\Delta U + OSP), \quad (76b)$$

and,

$$\Delta E = 1/3(\Delta U + \Delta IP + OSP) \quad . \quad (77b)$$

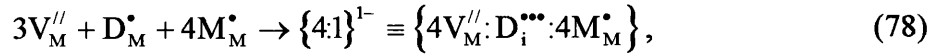
Using the above equations, the calculated stabilities of doped and undoped $\{4:1\}^{5-}$ clusters over isolated doubly charged vacancies and electronic holes are given in Table 27. To investigate the possible importance of crystal field effects, values of ΔE are given for both the case where the OSP is not included and also the case where it is (the latter values are shown in brackets in the table).

By comparison of Tables 26 and 27 we see that only in the case of pure undoped FeO and Fe doped MnO does the $\{4:1\}^{5-}$ cluster appear to be more stable than isolated neutral cation vacancies. This is true whether or not OSP terms are included. It is of interest therefore, to investigate the stability of a $\{4:1\}$ cluster of lower relative charge

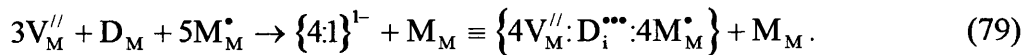
	Mn	Fe	Co	Ni
MnO	-0.76 (-0.40) †	-0.67 (-0.67) †	-0.67 (-0.40) †	-0.66 (—) †
FeO	0.51 (0.88) ‡	-0.62 (-0.62) †	0.28 (0.55) ‡	0.59 (—) ‡
CoO	-0.40 (-0.03) ‡	-0.61 (-0.61) †	-0.61 (-0.34) †	-0.29 (—) ‡
NiO	-0.72 (-0.35) ‡	-0.61 (-0.61) †	-0.61 (-0.33) †	-0.56 (—) †

Table 27. ΔE for the formation of $\{4:1\}^{5-}$ clusters from doubly charged vacancies via equations 74 and 75. The equation used in deriving each number is indicated in each case by † and ‡ respectively. Values in brackets include an estimate of the effect of the octahedral site preference energy of the relevant dopant cation. All energies are in eV.

and for this we choose the $\{4:1\}^{1-}$ cluster. The formation of this cluster from doubly charged vacancies can be written as,



and,



Again we calculate ΔE via equations 76 and 77, including both the case with and without OSP energies. The values thus calculated for ΔE are given in Table 28.

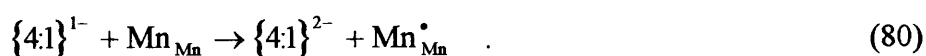
It is seen from Table 28 that $\{4:1\}^{1-}$ clusters appear to be preferred over isolated vacancies in all the pure and doped oxides considered. In NiO, Mn^{3+} , Fe^{3+} and Co^{3+} all increase the stability of $\{4:1\}^{1-}$ clusters when present in the interstitial site. When OSP energies are included, the stability of several of the clusters is significantly reduced

	Mn	Fe	Co	Ni
MnO	-1.62 (-1.25) †	-1.53 (-1.53) †	-1.52 (-1.25) †	-1.51 (—) †
FeO	-0.50 (-0.13) ‡	-1.63 (-1.63) †	-0.71 (-0.44) ‡	-0.38 (—) ‡
CoO	-1.49 (-1.13) ‡	-1.70 (-1.70) †	-1.69 (-1.42) †	-1.35 (—) ‡
NiO	-1.92 (-1.55) ‡	-1.81 (-1.81) †	-1.79 (-1.52) †	-1.72 (—) †

Table 28. ΔE for the formation of $\{4:1\}^{1-}$ clusters from doubly charged vacancies via equations 78 and 79. The equation used in deriving each number is indicated in each case by † and ‡ respectively. Values in brackets include an estimate of the effect of the octahedral site preference energy of the relevant dopant cation. All energies are in eV.

(although not to the point where isolated neutral vacancies are more favoured). In these cases, notably for $\{4:1\}^{1-}$ formation in undoped MnO, addition of Fe^{3+} dopant ions improves the stability.

In the case of $\{4:1\}^{1-}$ formation in undoped MnO, it is of interest to investigate the result of replacing the Mn^{3+} interstitial with Mn^{2+} and thus forming a $\{4:1\}^{2-}$ cluster. We can investigate the relative stabilities of these two clusters by writing,



Using the value of 1.1 eV for the OSP of Mn^{3+} ,³⁰ we find that the *right hand side* of equation 80 is favoured by 0.37 eV. So there is a suggestion here that if $\{4:1\}$ clusters do form in MnO, then the interstitial position may be occupied by something other than Mn^{3+} ; either a dopant cation or Mn^{2+} . A similar conclusion was drawn in the earlier work of Muxworthy [71]. It is clear, however, that we need to examine carefully methods for the inclusion of energy terms from crystal field effects.

11.4 Conclusions

In this chapter we used values for the change in internal energy of defect formation, to investigate the effects of dopants on the point defect structure of Mn_{1-x}O , Fe_{1-x}O , Co_{1-x}O and Ni_{1-x}O . We were rather restrictive in our treatment and considered only interactions where the dopant took up the interstitial site in a $\{4:1\}$ cluster and where the dopant was in the 3+ charge state when associated with vacancies on the cation sub-lattice. Our results for the undoped oxides are in agreement with those found previously by other workers [4,70] and demonstrate the marked stability of the charge compensated $\{4:1\}^{1-}$ over isolated neutral and singly charged cation vacancies.

³⁰ Mn^{2+} has a high spin d^5 configuration at both lattice and interstitial sites and hence its OSP energy is zero.

Although Mn, Fe and Co are shown to increase the stability of {4:1} clusters in Ni_{1-x}O , the low value of x attained in practice for this oxide means that {4:1} clusters are still unlikely to form. In the case of Mn_{1-x}O , if we include some estimate for the influence of crystal field effect on cluster stability, then doping with Fe may increase the chances of {4:1} clusters forming. In general, doping with Fe is seen to increase cluster stability in all the oxides considered.

REFERENCES

- [1] N.F.Mott and M.J.Littleton, *Trans. Faraday Soc.* 34 (1938) 485.
- [2] C.R.A. Catlow, R. James, W.C. Mackrodt and R.F. Stewart, *Phys. Rev. B* 25 (1982) 1006.
- [3] H. Donnerberg and C.R.A. Catlow, *J. Phys. Condens. Matter* 5 (1993) 2947.
- [4] C.R.A. Catlow and B.E.F. Fender, *J. Phys. C* 8 (1975) 3267.
- [5] A.B.Lidiard, in "Crystals with the fluorite structure", Ed. W.Hayes (Clarendon Press, Oxford 1974).
- [6] J. Oberschmidt, *Phys. Rev. B* 23 (1981) 5038.
- [7] J.H. Harding, *J. Chem. Soc. Faraday Trans 2* 83 (1987) 1177.
- [8] R. Tetot, M. Benzakour and G. Boureau, *J. Phys. Chem. Solids* 51 (1990) 545.
- [9] J.H. Harding, *Physica B* 131 (1985) 13.
- [10] R.W. Grimes and C.R.A. Catlow, *Phil. Trans. R. Soc. Lond. A.* 335 (1991) 609.
- [11] C.R.A.Catlow and W.C.Mackrodt, in "Computer Simulation of Solids", Eds. C.R.A.Catlow and W.C.Mackrodt (Springer Verlag, Berlin 1982).

- [12] M.Leslie, S.E.R.C. Daresbury Laboratory Report DL/SCI/TM31T (1982).
- [13] W.H.Press, S.A.Teukolsky, W.T.Vetterling and B.P.Flannery, "Numerical Recipes in C" 2nd Edition (Cambridge University Press 1992).
- [14] M.Leslie, *Physica*, 131B (1985) 145.
- [15] J.H.Harding, *Mol. Simul.* 4 (1990) 255.
- [16] R.G.Gordon and Y.S.Kim, *J. Chem. Phys.* 56 (1972) 3122.
- [17] M.J.Clugston, *Advances in Physics* 27 (1978) 893.
- [18] J.H.Harding and A.H.Harker, AERE Harwell Report AERE-R-10425 (1982).
- [19] R.D.Cowan and D.C.Griffin, *J. Opt. Soc. Am.* 66 (1976) 1010.
- [20] P.W.Fowler, P.J.Knowles and N.C.Pyper, *Mol. Phys.* 56 (1985) 83.
- [21] J.C.Slater and J.G.Kirkwood, *Phys. Rev.* 37 (1931) 682.
- [22] V.Butler, C.R.A.Catlow and B.E.F.Fender, *Radiat. Eff.* 73 (1983) 273.
- [23] R.Pandey, J.Zuo and A.B.Kunz, *J. Mater. Res.* 5 (1990) 623.
- [24] J.D. Gale, C.R.A. Catlow and W.C. Mackrodt, *Modelling Simul. Mater. Sci. Eng.* 1 (1992) 73.

- [25] C.R.A. Catlow, M. Dixon, W.C. Mackrodt, in "Computer Simulation of Solids", Eds. C.R.A. Catlow and W.C. Mackrodt (Springer Verlag, Berlin 1982).
- [26] B.G. Dick, Jr and A.W. Overhauser, Phys. Rev. 112 (1958) 90.
- [27] B.T.M. Willis, J. Chem. Soc., Faraday Trans. 2 83 (1987) 1073.
- [28] D.J.M. Bevan, I.E. Grey and B.T.M Willis, J. Solid State Chem. 61 (1986) 1.
- [29] C.R.A. Catlow, Proc. R. Soc. Lond. A. 353 (1977) 533.
- [30] H.J. Matzke, J. Chem. Soc. Faraday Trans. 86 (1990) 1243.
- [31] M.A. Bredig, Colloq. Int. C.N.R.S. 205 (1971) 183.
- [32] J.P. Hiernaut, G.J. Hyland and C. Ronchi, Int. J. Thermophys. 14 (1993) 259.
- [33] G.J. Hyland and J. Ralph, High Temp. High Press. 15 (1983) 179.
- [34] G.J. Hyland, "Theory of the Bredig Transition in UO_{2+x} .", Report of the Univ. Warwick.
- [35] R.A. Young, J. Nucl. Mater. 81 (1979) 283.
- [36] H. Kleykamp, J. Nucl. Mater. 131 (1985) 221.

- [37] Hj. Matzke, P.G. Lucuta and R.A. Verrall, *J. Nucl. Mater.* 185 (1991) 292.
- [38] H. Kleykamp, to be published.
- [39] Hj. Matzke, *Rad. Eff.* 53 (1980) 219.
- [40] Hj. Matzke and J.A. Davies, *J. App. Phys.* 38 (1967) 805.
- [41] C.R.A. Catlow and A.B. Lidiard, *Proc. of Conference of Thermodynamics of Reactor Materials, IAEA 2* (1974) 27.
- [42] R.A. Jackson, A.D. Murray, J.H. Harding and C.R.A. Catlow, *Phil. Mag. A.* 53 (1986) 27.
- [43] P. Sindzingre and M.J. Gillan, *J. Phys. C.* 21 (1988) 4017.
- [44] C.R.A. Catlow, *Proc. R. Soc. Lond. A.* 364 (1978) 473.
- [45] P.J. Kelly and M.S.S. Brooks, *J. Chem. Soc. Faraday Trans. 2* 83 (1987) 1189.
- [46] J.R. MacEwan and W.H. Stevens, *J. Nucl. Mater.* 11 (1964) 77.
- [47] W. Miekeley and F.W. Felix, *J. Nucl. Mater.* 42 (1972) 297.
- [48] R. Lindner and Hj. Matzke, *Z. Naturforschg.* 14a (1959) 582.
- [49] Hj. Matzke, *Nucl. Applic.* 2 (1966) 131.

- [50] R.G.J.Ball and R.W.Grimes, *J. Chem. Soc. Faraday Trans.* 86 (1990) 1257.
- [51] R.A.Jackson and C.R.A.Catlow, *J. Nucl. Mat.* 127 (1985) 161.
- [52] R.A.Jackson, C.R.A.Catlow and A.D.Murray, *J. Chem. Soc. Faraday Trans.* 2 83 (1987) 1171.
- [53] J.R.MacEwan and P.A.Morel, *Nucl. Applic.* 2 (1966) 158.
- [54] E.H.P. Cordfunke and R.J.M. Konings, *J. Nucl. Mater.* 152 (1988) 301.
- [55] H. Kleykamp, J.O. Paschoal, R. Pejsa and F. Thümmel, *J. Nucl. Mater.* 130 (1985) 426.
- [56] Hj. Matzke, *J. Nucl. Mater.* 223 (1995) 1.
- [57] I.L.F. Ray, personal communication.
- [58] D.R. Olander, "Fundamental Aspects of Nuclear Reactor Fuel Elements" (Energy Research and Development Administration 1976).
- [59] G. Giacchetti and C. Sari, *Nucl. Technol.* 31 (1976) 62.
- [60] S.G. Prussin, D.R. Olander, W.K. Lau and L. Hansson, *J. Nucl. Mater.* 154 (1988) 25.
- [61] W.R. Johnson, D. Kolb and K.N.Huang, *Atomic Nucl. Data Tables* 28 (1983).

- [62] Gmelin Handbook of Inorganic Chemistry, 8th Edition (Springer Verlag 1983 and 1985).
- [63] C.R.C. Handbook of Chemistry and Physics, 65th Edition (C.R.C. Press 1984).
- [64] E. Clementi and C Roetti, Atomic Nucl. Data Tables 14 (1974) 227.
- [65] P.W. Atkins, "Physical Chemistry" 4th Edition (Oxford University Press 1990).
- [66] P. Kofstadt, "Nonstoichiometry, Diffusion and Electrical Conductivity in Binary Metal Oxides" (Wiley, New York 1972).
- [67] C.R.A. Catlow, W.C. Mackrodt, M.J. Norgett and A.M. Stoneham, Phil. Mag. 35 (1977) 177.
- [68] C.R.A. Catlow, W.C. Mackrodt, M.J. Norgett and A.M. Stoneham, Phil. Mag. A 40 (1979) 161.
- [69] S.M. Tomlinson, PhD Thesis, Univ. London (1987).
- [70] S.M. Tomlinson, C.R.A. Catlow and J.H. Harding, J. Phys. Chem. Solids 51 (1990) 477.
- [71] D.G. Muxworthy, AERE Harwell report TP667 (1978).
- [72] F. Koch and J.B. Cohen, Acta Cryst. B25 (1969) 275.

- [73] A.K. Cheetham, B.E.G. Fender and R.I. Taylor, *J. Phys. C* 4 (1971) 2160.
- [74] C. Lebreton and L.W. Hobbs, *Radiat. Eff.* 74 (1983) 227.
- [75] F. Gesmundo, F. Viani, G. Petot-Ervas, C. Petot and V. Buscaglia, *Adv. Ceram.* 23 (1987) 83.
- [76] G. Petot-Ervas, C. Petot, F. Gesmundo and C. Clauss, *J. Phys. Chem. Solids* 51 (1990) 27.
- [77] Hj. Matzke, *Advances in Ceramics* 17 (1986) 1.
- [78] R. Dieckmann, *Solid State Ionics* 12 (1984) 1.
- [79] P. Kofstadt, *Solid State Ionics* 12 (1984) 101.
- [80] M.J. Radler, J.B. Cohen, G.P. Sykora, T. Mason, D.E. Ellis and J. Faber, *J. Phys. Chem. Solids* 53 (1992) 141.
- [81] J.D. Dunitz, and L.E. Orgel, *J. Phys. Chem. Solids* 3 (1957) 318.
- [82] D.S. McClure, *J. Phys. Chem. Solids* 3 (1957) 311.
- [83] R.W. Grimes, A.B. Anderson and A.H. Heuer, *J. Solid. St. Chem.* 69 (1986) 619.
- [84] M. Born and K. Huang, "Dynamical Theory of Crystal Lattices" (Oxford University Press 1954).